An early, novel arginine methylation of KCa3.1 attenuates subsequent T cell exhaustion.

Authors:

Piyush Sharma[1], Ao Guo[1], Suresh Poudel[1], Emilio Boada-Romero[1], Katherine C. Verbist[1], Gustavo Palacios[1], Kalyan Immadisetty[2], Mark J. Chen[1,3], Dalia Haydar[4], Ashutosh Mishra[5], Junmin Peng[5,6], M. Madan Babu[2], Giedre Krenciute[4], Evan S. Glazer[7], Douglas R. Green[1].

[1]Department of Immunology, St. Jude Children's Research Hospital, Memphis, TN 38105, USA

[2]Center of Excellence in Data Driven Discovery, Department of Structural Biology, St. Jude Children's Research Hospital, Memphis, TN 38105, USA

[3]Department of Laboratory Medicine, Cleveland Clinic, Cleveland, OH 44106, USA

[4]Department of Bone Marrow Transplantation and Cellular Therapy, St. Jude Children's Research Hospital, Memphis, TN 38105, USA

[5]Center for Proteomics and Metabolomics, St. Jude Children's Research Hospital, Memphis, TN 38105, USA

[6]Department of Structural Biology, Department of Developmental Neurobiology, St. Jude Children's Research Hospital, Memphis, TN 38105, USA

[7]Department of Surgery, University of Tennessee Health Science Center, 910 Madison Ave., Suite 300, Memphis, TN 38163, USA

Correspondence to piyush.sharma@stjude.org, douglas.green@stjude.org

ABSTRACT

T cell receptor (TCR) engagement initiates the activation process, and this signaling event is regulated in multifaceted ways. Nutrient availability in the immediate niche is one such mode of regulation[1-3]. Here, we investigated how the availability of an essential amino acid methionine (Met) and TCR signaling might interplay in the earliest events of T cell activation to affect subsequent T cell fate and function. We found that limiting Met during only the initial 30 minutes of $CD8^+$ T cell activation increased Ca^{2+} influx, Ca^{2+}-mediated NFAT1 (*Nfatc2*) activation, NFAT1 promoter occupancy, and T cell exhaustion. We identified changes in the protein arginine methylome during the initial 30 min of TCR engagement and discovered a novel arginine

32 methylation of a Ca^{2+}-activated potassium transporter, KCa3.1, which regulates Ca^{2+}-mediated
33 NFAT1 signaling to ensure optimal activation. Ablation of arginine methylation in KCa3.1 led to
34 increased NFAT1 activation, rendering T cells dysfunctional in murine tumour and infection
35 models. Furthermore, acute Met supplementation at early stages reduced nuclear NFAT1 in
36 tumour-infiltrating T cells and augmented their anti-tumour activity. Our findings identify a
37 metabolic event occurring early after T cell activation that influences the subsequent fate of the
38 cell.
39
40 **Methionine limitation promotes T cell exhaustion.**
41 During TCR engagement, nutrient metabolism ensures effective and optimal T cell activation and
42 function[4]. To determine which amino acids were rapidly consumed upon T cell activation, we
43 activated OT-I transgenic $CD8^+$ T cells in complete medium and performed targeted mass
44 spectrometry. We observed a significant decrease in intracellular Met and other amino acids as
45 early as 10 min (Fig. 1A). Among the amino acids important for T cells, Met is the sole amino acid
46 responsible for cellular methylome maintenance via the S-adenosyl Met (SAM) pathway, and
47 alterations in the SAM pathway adversely affect T cell functions[5,6]. In complete media, no
48 concomitant changes were observed in SAM or S-adenosyl homocysteine (SAH) (Fig. 1B, upper
49 panel). T cells consumed their intracellular Met pool only in Met-deprived medium, correlating
50 with decreases in SAM concentration and corresponding increases in SAH (Fig.1B, bottom panel).
51 These observations indicate that extracellular Met availability is required to maintain the SAM
52 cycle during T cell activation.
53
54 Mice infected with chronic Lymphocytic choriomeningitis virus (LCMV) have ~65% less Met
55 than in serum as early as day 2 post infection[7] (Extended Data Fig. 1A), suggesting that T cells
56 can experience low Met conditions during activation. To determine whether Met limitation during
57 TCR engagement affects T cell proliferation, we lowered the available amount of Met to 0.03 mM
58 in the culture medium. Cell-trace violet (CTV) labelled OT-I $CD8^+$ T cells were activated in media
59 with control (0.1 mM) or 0.03 mM Met for 30 min to 6 hr, after which Met was restored to 0.1
60 mM, and we observed no difference in the proliferation of T cells activated in reduced Met for
61 different times (Fig. 1C). When then assessed their activity *in vivo* upon transferring these
62 activated T cells into mice bearing B16/MC38 tumours expressing ovalbumin (B16-OVA/ MC38-

63 OVA) 24 h after activation (Fig. 1D), we observed defective tumour control in T cells activated in
64 0.03 mM Met compared to 0.1 mM Met, across all time points, with the earliest being 30 min
65 (*Rag1*$^{-/-}$ mice: Fig. 1E-G-B16-OVA; B6 WT mice: Extended Data Fig. 1B, C-MC38-OVA). To
66 further assess this effect, we generated LCMV GP33-specific memory T cells and activated them
67 for 24 hrs with GP33 peptide in either 0.1 mM Met or 0.03 mM Met for 30 min, after which Met
68 was restored to 0.1 mM and then transferred them into B16-GP33 (B16 expressing GP33 peptide)
69 tumour-bearing *Rag1*$^{-/-}$ mice (Extended Data Fig. 1D). We observed defective tumour control
70 leading to poor survival in mice receiving T cells activated in 0.03 mM Met compared to 0.1 mM
71 Met (Fig. 1H and I).
72
73 To examine the effects of activation in reduced Met on the T cell epigenome, we performed
74 ATAC-Seq at 24 hrs post activation (Extended Data Fig. 1E) and observed increased chromatin
75 accessibility in T cells activated in 0.03 mM Met during the initial 30 min (Extended Data Fig. 2A
76 and B). Overrepresentation analysis showed enrichment of gene sets associated with an
77 exhaustion-like phenotype (Extended Data Fig. 2C). Further HOMER motif analysis showed that
78 transcription factor (TF) motifs known to be associated with exhausted T cells[8,9] were highly
79 accessible in 0.03 mM-activated T cells (Extended Data Fig. 2D).
80
81 We activated OT-I CD8^{+} T cells T cells in either control or 0.03 mM Met for the initial 30 min
82 followed by 24 hours culture in 0.1 mM Met and injected them into B16-OVA bearing *Rag1*$^{-/-}$
83 mice. TILs were collected at day 9 post T cell injection. Again, animals receiving T cells activated
84 initially in 0.03 mM Met showed defective tumour control (Extended Data Fig. 2E and F). The
85 CD8^{+} TILs displayed reduced CD62L^{+}, CD62L^{high} CD44^{high} central memory cells (Tcm) with
86 increased TOX expression and reduced IFNγ production compared to TILs from T cells activated
87 in Met replete media (Extended Data Fig. 2G).
88
89 T cell dysfunction is known to contribute to poor prognoses in cancer[10]. This dysfunctional state
90 is at least in part driven by the transcription factor (TF) TOX[11] and is accompanied by markers
91 such as increased surface expression of PD1 and Tim-3 and reduced effector cytokine
92 production[12,13]. To further examine the effect of activation in limiting Met, we activated CD45.1^{+}
93 or CD45.2^{+} OT-I CD8^{+} T cells in 0.1 (control) or 0.03 mM Met for 30 min, restored Met to 0.1

94 mM for 24 hrs, and mixed them at a ratio of 1:1 before transferring them into B16-OVA tumour-
95 bearing *Rag1*$^{-/-}$ mice (Fig. 2A). Even though CD8^{+} TIL initially activated in 0.03 mM outnumbered
96 the 0.1 mM-activated CD8^{+} TIL at day 12 (Fig. 2B and C), these cells exhibited significant
97 increases in exhaustion-associated expression of PD1 and Tim-3, reduced effector cytokines (Fig.
98 2D,E and Extended Data Fig. 2H), increased expression of exhaustion associated TF, TOX (Fig.
99 2F and G), and reduced expression of the stemness-associated TF, TCF-1 (Extended Data Fig. 2I).
100 Altogether, these results suggest that reduced Met during early TCR signaling promotes
101 acquisition of epigenomic changes associated with exhaustion and drives T cells towards a
102 dysfunctional, exhausted state.
103
104 Exhausted T cells have been further defined as precursors of exhaustion (TEXprog) and
105 TEXprogenitor-like cells, both of which produce a replicative burst and effector function upon
106 checkpoint blockade [14], and terminally exhausted cells (TEXterm), which fail to mount an effective
107 effector response [15,16]. Although TOX is associated with maintenance of exhausted T cells, it is
108 also expressed in TEXprog [17]. We therefore further dissected the TOX^{+} CD8^{+} T cells from the
109 experiment in Fig. 2F (Fig. 2H) and found decreased TEXprog (TCF1^{+}Tim-3^{-}) and increased
110 TEXterm (TCF1^{-}Tim-3^{+}) among T cells initially activated in 0.03 mM Met, suggesting a decreased
111 pool of stem-like TEXprog cells (Fig. 2I). Furthermore, evaluation of total CD8^{+} TILs from mice
112 receiving T cells initially activated in 0.03 mM Met for 30 minutes revealed a lower frequency of
113 TCF1^{+}Tim-3^{-} TEXprog cells and CX3CR1^{+}Ly108^{+} TEXprogenitor-like cells (Extended Data Fig.
114 2J) and a corresponding increase in the frequency of TEXterm cells defined as TCF1^{-}Tim-3^{+}
115 (Extended Data Fig. 2K). We also observed a decrease in memory-associated markers such as
116 CD62L^{+}, CD62L^{+}CD44^{+} (Extended Data Fig. 2L) and CD127^{+}CD27^{+} (Extended Data Fig. 2M
117 and N) and an increase in KLRG1^{+}CD127^{-} terminal effector-like T cells (Extended Data Fig. 2O
118 and P) when initially activated in 0.03 mM Met.
119
120 To examine the transcriptomic state, we performed global RNA-seq of day 9 TIL from T cells
121 originally activated for 30 min in 0.1 mM or 0.03 mM Met and then cultured in 0.1 mM Met for
122 24hrs prior to transfer into B16-OVA tumour-bearing *Rag1-/-* mice. We found several
123 transcriptomic changes, the majority of which represented increased expression of differentially
124 enriched (DE) genes in T cells initially activated in 0.03 mM Met (Extended Data Fig. 3A and B).

125 Over-representation analysis of the DE genes in T cells activated in 0.1 mM Met revealed
126 enrichment of GOBP pathways which are associated with T cell effector functions along with
127 increases in transcription factors associated with a stem-like T cell state and memory generation
128 [18-21] (Extended Data Fig. 3C). Cells initially activated in 0.03 mM Met showed enrichment of genes
129 which are associated with terminal differentiation or dysfunction of T cells and transcription
130 factors associated with hyperactivation and development and maintenance of T cell exhaustion [8,22-
131 24] (Extended Data Fig. 3D). GSEA analysis also showed an enriched exhaustion-associated gene
132 set [25,26] in $CD8^+$ TIL initially activated in 0.03 mM Met (Fig. 2J) and enrichment of hallmark gene
133 sets associated with T cell effector function in the control (0.1 mM Met) T cells (Extended Data
134 Fig. 3E). These results suggest that Met availability during early TCR engagement influences T
135 cell differentiation, with initial, reduced Met availability promoting hyperactivation and driving T
136 cells towards exhaustion.
137
138 **Extracellular Met metabolism regulates Ca^{2+} flux and NFAT1 activation.**
139 Among the earliest events in T cell activation is the influx of Ca^{2+} [27,28], which is accompanied by
140 the activation of calcineurin, which dephosphorylates Nuclear Factor of Activated T cells-1
141 (NFAT1), resulting in its nuclear translocation and activation[29,30]. Because low Met levels for only
142 the first 30 min of activation influenced the subsequent T cell phenotype, we investigated changes
143 in Ca^{2+} flux using Fluo-8. We observed increased Ca^{2+} influx upon stimulation of T cells with anti-
144 CD3/CD28 antibody in 0.03 mM compared to 0.1 mM Met (Fig. 3A), which was reduced by the
145 CRAC channel inhibitor YM-58483 (Extended Data Fig. 4A). NFAT1 cooperates with the AP1
146 complex to ensure optimal T cell activation and differentiation, but high levels of NFAT1 activity
147 have been associated with T cell dysfunction and exhaustion [29,31]. Confocal imaging revealed an
148 increase in activated NFAT1 (nuclear localization of NFAT1) in T cells activated for 30 min with
149 anti-CD3/28 beads in 0.03 mM Met compared to 0.1 mM Met (Fig. 3B, Extended Data Fig. 4B),
150 quantified as either a ratio of nuclear NFAT1 to total cell NFAT (Fig. 3C and Extended Data Fig.
151 4C(0.0 mM Met)) or as nuclear NFAT1 fluorescence intensity (Extended Data Fig. 4D), which
152 were abolished upon treatment with either the calcineurin inhibitor Cyclosporin A (CsA) (Fig. 3B
153 and C) or CRAC channel inhibitor YM-58483 (Extended Data Fig. 4E). Examination of NFAT2
154 at 30 min of activation revealed no difference in its activation in T cells activated in either 0.1 mM
155 or 0.03 mM Met (Extended Data Fig. 4F). Next, we activated $CD8^+$ T cells in complete medium

156 for 24hrs and rested them for 48hrs before secondary activation in 0.03 mM or 0.1 mM Met and
157 observed increased nuclear NFAT1 levels in 0.03 mM Met 30 min after activation (Extended Data
158 Fig. 4G), suggesting that the effect of limiting Met on NFAT1 activation is independent of previous
159 activation events.
160
161 NFAT1 is known to regulate several exhaustion-associated genes such as *Lag3, Pdcd1, Havcr2,*
162 *Ctla4, Tnfrsf9* [31]. We performed NFAT1 CUT&RUN on T cells activated in 0.1 mM or 0.03 mM
163 Met for 30 min, followed by 0.1 mM Met for 24hrs and observed increased NFAT1 binding in the
164 low Met group (Fig. 3D). We observed that Met limitation for the initial 30 min resulted in
165 increased NFAT1 binding to *Pdcd1, Havcr2, Lag3, and Tnfrsf9* (Fig. 3E) as well as *Ctla4 and Tox*
166 gene loci (Fig. 3F). This further correlated with increased transcription of most of these genes at
167 24 hrs (Extended Data Fig. 4H). Altogether, our results suggest that reduced Met availability
168 during the initial stages of TCR activation directs a trajectory of T cells towards hyperactivation
169 and eventual exhaustion, and the maintenance of extracellular Met levels in the face of rapid Met
170 consumption upon TCR engagement dampens Ca^{2+}-mediated NFAT1 activity and T cell fate.
171
172 **KCa3.1 methylation regulates NFAT1.**
173 Methionine metabolism is the sole pathway for epigenetic and proteomic methylome maintenance,
174 which is known to affect T cell function [32]. When converted to SAH, SAM acts as the methyl
175 donor; thus, the ratio of SAM to SAH is known as the cellular methylation potential [33], an index
176 of a cell's capacity to maintain its methylome. We calculated the SAM/SAH ratio over time after
177 TCR engagement in the absence of extracellular Met and found this ratio to be significantly
178 reduced as early as 10 min post-activation (Extended Data Fig. 5A), suggesting alterations in the
179 methylome. Met metabolism is essential for DNA methylation [34]; however, we found no
180 significant differences in global 5-methylcytosine levels at either 30 min or 24 hrs in T cells
181 activated as above (Extended Data Fig. 5B). We similarly assessed H3me3K27 and H3me2K4 by
182 CUT&RUN at 24 hrs post activation, but again, no global changes were observed (Extended Data
183 Fig. 5C and D). Thus, Met restriction for only the first 30 min of T cell activation does not appear
184 to directly affect global DNA or histone methylation.
185

186 Therefore, we postulated that Met restriction influences early methylation events independently of
187 direct effects on DNA and histone methylation. Post-translational protein arginine methylation
188 mediated by protein arginine methyltransferases regulates protein function [35,36]. We found that
189 arginine methylation in T cells activated in 0.0 mM or 0.03 mM Met was significantly reduced 30
190 min post-activation when compared to T cells activated in 0.1 mM Met (Fig. 4A and B, Extended
191 Data Fig. 5E). To identify specific proteins differentially methylated upon TCR engagement in
192 limited Met, $CD8^+$ T cells activated by anti-CD3 antibody with IgG cross-linking for 30 min were
193 processed for methyl-arginine immunoprecipitation and quantification using multiplexed tandem
194 mass tag-mass spectrometry (TMT-MS). We identified common proteins which were
195 differentially methylated in 0.0 mM and 0.03 mM Met activation conditions compared to 0.1 mM
196 Met (Fig. 4C) and found the top candidate, KCa3.1 to be di-methylated at Arginine-350 (R350) in
197 0.1 mM Met, which was reduced in 0.0 mM and 0.03 mM Met (Fig. 4D, Supplementary Table. 1).
198 Furthermore, protein-BLAST analysis showed that KCa3.1 R350 is conserved across species,
199 including humans, which suggested that R350 may be important for KCa3.1 regulation (Extended
200 Data Fig. 5F).
201
202 KCa3.1 is a calcium-activated potassium transporter encoded by *Kcnn4* and is activated by
203 calmodulin binding upon TCR-mediated Ca^{2+} flux[37]. During T cell activation, the plasma
204 membrane is hyperpolarized to ensure sufficient Ca^{2+} flux for signaling[38], and this is maintained
205 by K^+ efflux through potassium transporters such as KCa3.1[39,40]. Based on our earlier observation
206 of increased Ca^{2+} signaling under low Met conditions, we hypothesized that R350 methylation of
207 KCa3.1 regulates its activity, and loss of this methyl group may result in hyperactivation, leading
208 to increased Ca^{2+} influx and NFAT1 activation. To understand how arginine methylation may
209 mechanistically modulate KCa3.1 activity, we performed MD simulations with the solved crystal
210 structure of human KCa3.1(hKCa3.1) bound to calmodulin (CaM) at R352 (corresponding to R350
211 in murine KCa3.1) (Extended Data Fig. 5G). The calmodulin-binding pocket encompasses D78-
212 T79-D80-S81-E82-E83-E84, which is predominantly negatively charged/polar, where E84 forms
213 a salt bridge with R352 of hKCa3.1. Our results showed that both symmetrical di-methylation
214 (SDMA) and asymmetrical di-methylation (ADMA) of R352 introduced a hydrophobic methyl
215 group into this negatively charged/polar CaM binding pocket, thereby weakening the hKCa3.1 and
216 CaM interaction (Fig. 4E). Furthermore, MD simulations showed that the salt bridge interaction

217 of R352 with E84 of the CaM binding pocket diminished over time, especially in the case of
218 SDMA where both guanidino nitrogens are methylated, compared to ADMA in which only one
219 nitrogen is methylated (Fig. 4F, Extended Data Fig. 5H), suggesting that disruption of arginine
220 methylation promoted stabilization of calmodulin binding, leading to increased activation of the
221 channel and Ca^{2+} flux.
222
223 To validate our *in-silico* simulation results, we used the chemical inhibitor TRAM-34 to reduce
224 KCa3.1 activity [41,42] during T cell activation and observed reduced Ca^{2+} flux upon TRAM-34
225 treatment only in 0.03 mM Met and not in 0.1 mM Met (Fig. 4G) at the concentration of TRAM-
226 34 we employed. Measurement of nuclear NFAT1 levels revealed that the treatment normalized
227 nuclear NFAT1 levels in T cells activated in 0.03 mM Met in a dose-dependent manner and had
228 no effect on T cells activated in 0.1 mM Met (Extended Data Fig. 5I). We then activated OT-I T
229 cells in 0.1 mM or 0.03 mM Met with either DMSO or TRAM-34 for 30 min, washed and then
230 cultured the cells for an additional 24 hrs in 0.1 mM Met before transferring into B16-OVA
231 tumour-bearing *Rag1*$^{-/-}$ mice (Extended Data Fig. 5J). Chemical inhibition of KCa3.1 for 30 min
232 significantly improved anti-tumour activity in T cells activated for 30 min in 0.03 mM Met (Fig.
233 4H), suggesting that increased KCa3.1 activity was responsible for the eventual decreased T cell
234 function under this activation condition.
235
236 **Methylation-deficient KCa3.1 increases Ca^{2+}-mediated NFAT1 activation.**
237 To specifically interrogate the role of R350 methylation of KCa3.1 in T cell activation, we cloned
238 KCa3.1 (Kca3.1^{WT}) and a mutant with an alanine substitution (KCa.3.1^{R350A}) into retroviral vectors
239 and expressed them in primary murine $CD8^+$ T cells in which endogenous KCa3.1 was deleted
240 using CRISPR/Cas9 (Extended Data Fig. 6A, B and C), and expression of the two was similar
241 (Extended Data Fig. 6D). Fluo-8 Ca^{2+} flux analysis showed significantly increased flux upon
242 activation in KCa3.1^{R350A} T cells (Fig. 5A). Due to the expression of GFP by transduced T cells,
243 which might interfere with the Fluo-8 signal, we used another Ca^{2+}-sensitive dye, ICR-1AM, and
244 observed similar results (Extended Data Fig. 6E). Increased Ca^{2+} flux correlated with an increase
245 in nuclear NFAT1 30 min post activation (Fig. 5B, C and Extended Data Fig. 6F). This heightened
246 nuclear NFAT1 in cells expressing KCa3.1^{R350A} was visible under resting conditions and increased
247 upon activation in a time-dependent manner (Extended Data Fig. 6G).

248

249 To investigate the epigenomic state of WT or mutant KCa3.1 T cells, we analyzed global
250 chromatin accessibility via ATAC-Seq after 24 hrs of *in vitro* activation. We found that the
251 activated KCa3.1^{R350A} T cells showed distinct chromatin accessibility which was increased
252 compared to KCa3.1^{WT} T cells (Fig. 5D, Extended Data Fig. 7A). Furthermore, GSEA analysis
253 revealed enrichment of GOBP terms associated with negative regulators of T cell-mediated
254 immunity and gene sets associated with T cell exhaustion [25,26] in T cells expressing mutant
255 KCa3.1^{R350A} (Fig. 5E and F), suggesting that ablation of R350 methylation drives T cells towards
256 exhaustion early after activation. Upon comparing these ATAC-Seq results with ATAC-Seq of T
257 cells activated in 0.03 mM vs. 0.1 mM Met (Extended Data Fig. 2B), we found several common
258 differentially accessible regions (DAR) (Extended Data Fig. 7B) with enrichment of gene sets
259 associated with T cell exhaustion (Extended Data Fig. 7C). HOMER motif analysis of WT or
260 mutant T cells and common DARs was similarly enriched (Extended Data Fig. 2D, 7D and E).
261 Despite these results, KCa.3.1^{R350A} did not fully phenocopy the chromatin effects of activation in
262 0.03 mM Met, suggesting that other differentially methylated proteins in addition to KCa.3.1 may
263 also impact chromatin accessibility following activation in the latter condition.
264

265 To investigate whether the observed exhaustion-specific chromatin state led to defective
266 functionality of mutant KCa3.1 T cells, we transferred T cells expressing KCa.3.1^{WT} or
267 KCa.3.1^{R350A} into B16-OVA tumour-bearing Rag1$^{-/-}$ mice. We found that T cells expressing
268 KCa.3.1^{R350A} displayed impaired tumour control and survival (Fig. 5G, H and I), suggesting that
269 the absence of KCa3.1 methylation drives T cells towards an exhaustion trajectory, leading to
270 defective effector function and tumour control.
271

272 **Ablation of KCa3.1 methylation promotes T cell exhaustion.**

273 To determine whether ablation of R350 methylation drives T cell exhaustion in tumours, we
274 transferred T cells expressing KCa.3.1^{WT} or KCa.3.1^{R350A} into B16-OVA tumour-bearing Rag1$^{-/-}$
275 mice. Tumours were isolated and measured at day 12 post-T cell injection, and consistently, much
276 larger tumours were extracted from animals treated with T cells expressing KCa.3.1^{R350A}
277 (Extended Data Fig. 8A). KCa.3.1^{R350A}-expressing TIL showed high surface expression of the
278 exhaustion markers PD1, Lag3, and Tim-3 (Extended Data Fig. 8B) that correlated with increased

279 TOX expression (Extended Data Fig. 8C). Among these cells we also found fewer TEXprog
280 ($CD69^{lo}Ly108^{hi}$)[43] and IFNγ- and TNFα-producing T cells (Extended Data Fig. 8D and E). Next,
281 we performed a similar experiment in a competitive setting, wherein $CD45.1^{+}$ $KCa.3.1^{WT}$ and
282 $CD45.1^{+}CD45.2^{+}$ $Kca.3.1^{R350A}$-expressing OT-I $CD8^{+}$ T cells were mixed at a 1:1 ratio and
283 transferred into B16-OVA tumour-bearing *Rag1*$^{-/-}$ mice (Fig. 6A). TIL analysis at D12 showed
284 increased $PD1^{+}Tim\text{-}3^{+}$, $Eomes^{+}PD1^{+}$ (Fig. 6B, Extended Data Fig. 8F) and TOX expression in
285 $Kca.3.1^{R350A}$ -expressing T cells, which correlated with reduced expression of the effector
286 cytokines IFNγ and TNFα (Fig. 6C and D). Further analysis revealed a decreased frequency of
287 $TCF1^{+}Tim\text{-}3^{-}$ TEXprog and increased $TCF1^{-}Tim\text{-}3^{+}$ TEXterm populations (Extended Data Fig. 8G
288 and Fig. 6E). We also observed a decrease in $CD62L^{+}$ and $CD127^{+}CD27^{+}$ memory T cells (Fig.
289 6F) with an increase in the $KLRG1^{+}CD127^{-}$ terminal effector-like phenotype in $KCa.3.1^{R350A}$-
290 expressing T cells, as compared to T cells expressing WT KCa3.1 (Extended Data Fig. 8H and I).
291
292 T cell exhaustion is a prominent feature of chronic viral infection [44]. We utilized the LCMV
293 infection model in WT (CD45.2, Thy 1.2) mice into which $CD45.1^{+}CD45.2^{+}$ $KCa.3.1^{WT}$ and
294 $CD45.2^{+}$ $KCa.3.1^{R350A}$-expressing Thy1.1 ($CD90.1^{+}$) $P14^{+}$ T cells were injected at a 1:1 ratio into
295 mice infected with either an acute Armstrong or a chronic Clone-13 strain. Spleens were analyzed
296 on day 9 post-infection (Fig. 6G). The $KCa.3.1^{R350A}$ population frequency was significantly
297 reduced in Clone-13 infection, but no significant change was observed in acute infection (Extended
298 Data Fig. 8J). $KCa.3.1^{R350A}$-expressing T cells presented with increased TOX, PD1 and Tim-3
299 expression in both acute and chronic infections (Fig. 6H-K, Extended Data Fig. 8K). We also
300 found that $KCa.3.1^{R350A}$-expressing T cells harbored reduced frequencies of $CX3CR1^{+}PD1^{+}$
301 TEXprog cells (Fig. 6L) in both acute and chronic infection and increased $Tim\text{-}3^{+}Cx3CR1^{+}PD1^{+}$
302 TEXeff cells (T exhausted effector-like cells) and $TCF1^{-}Tim\text{-}3^{+}$ TEXterm cells in chronic infection
303 (Extended Data Fig. 8L and Fig. 6M). $KCa.3.1^{R350A}$-expressing $P14^{+}$ T cells displayed significantly
304 increased $KLRG1^{+}CD127^{-}$ terminal effector-like cells and a concurrent decrease in $KLRG1^{-}$
305 $CD127^{+}$ memory precursor cells in chronic infection but not in acute infection (Extended Data Fig.
306 8M-O). Thus, ablation of R350 methylation drives T cells towards an exhaustion trajectory even
307 at the early stages of infection. Together, these experiments support the idea that R350 methylation
308 maintains optimal KCa3.1 function, ensuring optimal T cell activation and effector function in
309 both tumours and viral infections.

310 **Acute Met supplementation promotes anti-tumour T cell function.**

311 $CD8^+$ T cells are activated in both secondary lymphoid tissues and within tumours [45,46]. While T
312 cells are known to be primarily activated in draining lymph nodes (dLNs), a recent study showed
313 that activation of tumour infiltrating T cells in tumour microenvironment is necessary to acquire
314 an effector-like phenotype[47]. Our results in Fig. 1H and Extended Data Fig. 4G support the idea
315 that Met is required for optimal TCR activation, and this requirement is independent of the prior
316 activation status of the T cell. Thus, we hypothesized that upon tumour infiltration, $CD8^+$ T cells
317 experience antigen presentation in a Met-deficient microenvironment, leading to altered effector
318 function. To evaluate Met levels in TILs, we performed mass spectrometric analysis of $CD8^+$ TIL
319 and dLN $CD8^+$ T cells from B16 subcutaneous tumour-bearing mice at day 9. We observed a ~50%
320 reduction in intracellular Met in $CD8^+$ TIL compared to that in dLN $CD8^+$ T cells (Extended Data
321 Fig. 9A, Supplementary table 2). We also observed a similar decrease in intracellular Met in $CD8^+$
322 TIL isolated from primary human colorectal carcinomas compared with corresponding $CD8^+$ T
323 cells from PBMC (Extended Data Fig. 9B). To determine whether $CD8^+$ TIL with reduced
324 intracellular Met showed increased nuclear NFAT1, we sorted activated $CD44^+$ $CD8^+$ T cells from
325 B16 tumours and respective dLN at day 9 post implantation and imaged for NFAT1. We observed
326 increased levels of nuclear NFAT1 in $CD44^+CD8^+$ TIL compared to counterparts from dLN (Fig.
327 7A), suggesting that reduced Met availability in the TME may have led to increased NFAT1
328 activation in those T cells.

329

330 Continuous Met supplementation in tumours has been shown to promote anti-tumour T cell
331 activity, associated with global epigenetic maintenance [32]. Our findings, however, highlight an
332 early role for Met in T cell fate, and we hypothesized that Met supplementation up to that of serum
333 levels at the early stages of tumour development would increase T cell anti-tumour activity. We
334 therefore injected 50 µl of 61µM Met peri-tumourally once per day for 5 days when tumour
335 volumes were 70-100 mm^3 (Extended Data Fig. 9C) and found that treatment decreased nuclear
336 NFAT1 levels in $CD44^+$ $CD8^+$ TIL as compared to TIL from HBSS-injected tumours (Fig. 7B).
337 Indeed, nuclear NFAT1 in TIL was similar to or lower than that in $CD8^+$ T cells from dLN
338 (Extended data Fig. 9D). Furthermore, acute Met supplementation delayed tumour growth in
339 multiple murine tumour models, thereby improving overall survival (Fig. 7C, D and Extended
340 Data Fig. 9E-G). Met supplementation resulted in decreased PD1 and Tim-3 surface expression in

341 $CD8^+$ TIL, along with increased $CD62L^{hi}CD44^{hi}$ Tcm and reduced $CD62L^{lo}CD44^{hi}$ Tem
342 (Extended Data Fig. 9H and I) compared to TIL in HBSS-treated tumours. In contrast to
343 immunocompetent WT mice, Met injected peri-tumourally in tumour-bearing NSG mice resulted
344 in no difference in tumour growth (Extended Data Fig. 9J), implying a lymphocyte-mediated
345 effect. Depletion with an anti-CD8 antibody (Extended Data Fig. 9K) in B16-OVA tumour-bearing
346 mice abrogated the effect of Met supplementation on tumour control (Fig. 7E and F), supporting
347 the conclusion that the observed Met supplementation-mediated tumour control is dependent on
348 $CD8^+$ T cells. We then employed a contralateral tumour model with B16-OVA implanted in one
349 shoulder and in the opposite abdominal flank and injected Met peri-tumourally to the latter tumour.
350 Met supplementation of the abdominal flank tumours impeded contralateral tumour growth
351 (Extended Data Fig. 10A and B), further suggesting a T cell response. These results are consistent
352 with the idea that acute Met supplementation promoted tumour control by $CD8^+$ T cells. We also
353 found that an 0.5% increase in dietary Met supplementation in B16 tumour-bearing mice showed
354 better tumour growth control (Extended Data Fig. 10C), which is concordant with a recent study
355 showing that Met supplementation in humans increased the effector function of $CD8^+$ T cells [32].
356 Met supplementation, therefore, enhances the anti-tumour function of $CD8^+$ T cells.
357
358 **Met supplementation enhances CAR and ICB treatment.**
359 CAR-T cell treatment has been clinically successful in the treatment of hematological
360 malignancies, but less so in solid tumours [48,49]. In a solid tumour model in *Rag1*$^{-/-}$ mice, we
361 supplemented Met in the presence of transferred murine B7-H3 CAR-T cells into animals bearing
362 a B7-$H3^+$ F420 tumour[50] (Extended Data Fig. 10D). Again, Met supplementation improved tumour
363 control and animal survival in this model (Fig. 7G and H).
364
365 Immune checkpoint blockade (ICB) has been widely used either alone or in combination with
366 cancer treatments[51]. To query whether Met supplementation might cooperate with ICB, we
367 administered either IgG isotype or anti-PD1 antibody along with HBSS or Met supplementation
368 in subcutaneous MC38 tumour-bearing mice (Extended Data Fig. 10E) and found that
369 peritumoural Met supplementation with anti-PD1 treatment resulted in significantly reduced
370 tumour growth and increased survival of these animals compared to controls (Extended Data Fig.
371 10F and G). As local Met supplementation may not be feasible in the clinical setting, we performed

372 an ICB experiment with dietary supplementation of Met (Extended Data Fig. 10H). We observed
373 that a diet containing 1.5% Met (0.5% increase in dietary Met) enhanced the efficacy of anti-PD-
374 1, leading to significant control of tumour growth and survival of the mice, compared to that of
375 anti-PD1 with control diet (Fig. 7I-K, Supplementary Table. 3). These results suggest the potential
376 application of Met as a combinatorial treatment in the existing immunotherapies.
377
378 **Discussion**
379 T cell exhaustion is generally understood to be a consequence of persistent antigen stimulation
380 [12,44]; however, situations exist in which antigen persistence does not result in exhaustion, such as
381 in autoimmune T cells in Type I diabetes [21]. It is therefore possible that in addition to chronic
382 antigen exposure, nutrient limitation contributes to exhaustion [52,53]. A recent study suggested that
383 T cells can follow an exhaustion trajectory within hours of antigen recognition [54]. Here, we propose
384 that the state of T cell exhaustion is the result of a multifactorial pathway that involves the
385 assimilation of different input signals, including nutrients, and is engaged as early as the initial
386 recognition of cognate antigen.
387
388 Studies have shown that strong TCR signals result in hyperactivation and activation-induced cell
389 death, whereas weak TCR signals result in dampened responses [55]. NFAT family members are key
390 regulators of T cell activation and interact with key partners to induce activation-associated genes
391 including effector- and exhaustion-associated genes [28]. Continuous or partner-less NFAT
392 activation is associated with hyperactivation, anergy and exhaustion [29,31,56]; therefore, NFAT
393 activation must be tightly controlled for optimal T cell function, but little is known about how
394 niche-specific nutrients regulate NFAT. We found that during rapid tumour proliferation in the
395 early growth phase, $CD8^+$ TIL display increased NFAT1 activation, which is regulated
396 metabolically. Our data provide a novel mechanism of Met metabolism in the regulation of NFAT1
397 activation via post-translational modification of KCa3.1, without which $CD8^+$ T cells progress
398 towards exhaustion (Extended Data Fig. 11). We found that arginine methylation in KCa3.1 limits
399 Ca^{2+}-dependent NFAT1 signaling, ensuring optimal activation in tumours and infections. Met
400 supplementation to the TME preserves anti-tumour immunity [32] and limits exhaustion (this study),
401 a treatment that can be harnessed to improve patient prognosis in combination with ICB therapies.
402 Our results emphasize the importance of non-histone protein methylation in the functional

403 maintenance of T cells in diseases and describe a link between TCR signaling, metabolic
404 regulation, and transcription factor activation. These results suggest a change in the current dogma
405 of T cell exhaustion from a state driven only by persistent antigen exposure—acquired over a long
406 period of time—to a dynamic state controlled by multiple pathways over the course of T cell
407 activation and differentiation. Our study supports the idea that metabolism-dependent, rapid
408 proteomic modifications that occur upon TCR engagement influence subsequent T cell fate and
409 provides mechanistic insight into how niche-specific nutrient deprivation renders T cells
410 dysfunctional
411

412 **Acknowledgements**

413 We thank P. Fitzgerald, S. Sirasanagandla, M. Yang and L. Harris, for technical and administrative
414 assistance; L. Long and H. Chi for providing retroviral vectors and Cas9-OTI mice; C. Guy for
415 microscope imaging assistance; M. Morrison for organizing patient samples; the staff at the St.
416 Jude Immunology Flow Cytometry Core Facility for cell sorting. Statistical calculations were
417 performed using GraphPad Prism. We thank Dr. S. Pounds for the additional assistance with the
418 statistical analysis of the data in Fig. 4A. Illustrations were created using BioRender software. This
419 work was supported by National Institutes of Health grants AI123322 and CA231620 to D.R.G.,
420 American Lebanese Syrian Associated Charities (ALSAC) to G.K., and National Cancer Institute
421 grant K99CA256262 to D.H.
422

423 **Author Contributions**

424 P.S. conceived the project, designed, performed most experiments, interpreted results, and wrote
425 the manuscript. A.G. contributed to CUT&RUN, ATAC-Seq, and RNA-Seq experiments. K.V.
426 and E.B.R. helped in the development of the flow cytometry panel, experiments, and review of the
427 manuscript. G.P. contributed to and processed the LC-MS/MS experiments. D.H. and G.K.
428 assisted with CAR-T cell experiments. K.I. and M.B. performed MD simulations and analyses.
429 S.P. and M.J.C. analyzed the CUT&RUN, ATAC-seq, and RNA-seq data. A. M. and J.P.
430 performed and analyzed methyl-arginine immunoprecipitation and TMT-MS experiments. E.S.G
431 provided patient tumour samples. D.R.G. supervised the experimental designs, interpreted the
432 results, and wrote the manuscript.

433 **References**

1 Lim, A. R., Rathmell, W. K. & Rathmell, J. C. The tumor microenvironment as a metabolic barrier to effector T cells and immunotherapy. *Elife* **9** (2020). https://doi.org:10.7554/eLife.55185

2 Kedia-Mehta, N. & Finlay, D. K. Competition for nutrients and its role in controlling immune responses. *Nat Commun* **10**, 2123 (2019). https://doi.org:10.1038/s41467-019-10015-4

3 Wei, J., Raynor, J., Nguyen, T. L. & Chi, H. Nutrient and Metabolic Sensing in T Cell Responses. *Front Immunol* **8**, 247 (2017). https://doi.org:10.3389/fimmu.2017.00247

4 Cohen, S., Danzaki, K. & MacIver, N. J. Nutritional effects on T-cell immunometabolism. *Eur J Immunol* **47**, 225-235 (2017). https://doi.org:10.1002/eji.201646423

5 Klein Geltink, R. I. & Pearce, E. L. The importance of methionine metabolism. *Elife* **8** (2019). https://doi.org:10.7554/eLife.47221

6 Yang, X. *et al.* MAT2A-Mediated S-Adenosylmethionine Level in CD4(+) T Cells Regulates HIV-1 Latent Infection. *Front Immunol* **12**, 745784 (2021). https://doi.org:10.3389/fimmu.2021.745784

7 Lercher, A. *et al.* Type I Interferon Signaling Disrupts the Hepatic Urea Cycle and Alters Systemic Metabolism to Suppress T Cell Function. *Immunity* **51**, 1074-1087 e1079 (2019). https://doi.org:10.1016/j.immuni.2019.10.014

8 Beltra, J. C. *et al.* Stat5 opposes the transcription factor Tox and rewires exhausted CD8(+) T cells toward durable effector-like states during chronic antigen exposure. *Immunity* **56**, 2699-2718 e2611 (2023). https://doi.org:10.1016/j.immuni.2023.11.005

9 Belk, J. A. *et al.* Genome-wide CRISPR screens of T cell exhaustion identify chromatin remodeling factors that limit T cell persistence. *Cancer Cell* **40**, 768-786 e767 (2022). https://doi.org:10.1016/j.ccell.2022.06.001

10 Thommen, D. S. & Schumacher, T. N. T Cell Dysfunction in Cancer. *Cancer Cell* **33**, 547-562 (2018). https://doi.org:10.1016/j.ccell.2018.03.012

11 Khan, O. *et al.* TOX transcriptionally and epigenetically programs CD8(+) T cell exhaustion. *Nature* **571**, 211-218 (2019). https://doi.org:10.1038/s41586-019-1325-x

12 Wherry, E. J. & Kurachi, M. Molecular and cellular insights into T cell exhaustion. *Nat Rev Immunol* **15**, 486-499 (2015). https://doi.org:10.1038/nri3862

13 Zhang, Z. *et al.* Pan-cancer landscape of T-cell exhaustion heterogeneity within the tumor microenvironment revealed a progressive roadmap of hierarchical dysfunction associated with prognosis and therapeutic efficacy. *EBioMedicine* **83**, 104207 (2022). https://doi.org:10.1016/j.ebiom.2022.104207

14 Kallies, A., Zehn, D. & Utzschneider, D. T. Precursor exhausted T cells: key to successful immunotherapy? *Nat Rev Immunol* **20**, 128-136 (2020). https://doi.org:10.1038/s41577-019-0223-7

15 Hudson, W. H. *et al.* Proliferating Transitory T Cells with an Effector-like Transcriptional Signature Emerge from PD-1(+) Stem-like CD8(+) T Cells during Chronic Infection. *Immunity* **51**, 1043-1058 e1044 (2019). https://doi.org:10.1016/j.immuni.2019.11.002

16 Utzschneider, D. T. *et al.* Early precursor T cells establish and propagate T cell exhaustion in chronic infection. *Nat Immunol* **21**, 1256-1266 (2020). https://doi.org:10.1038/s41590-020-0760-z

17 Alfei, F. *et al.* TOX reinforces the phenotype and longevity of exhausted T cells in chronic viral infection. *Nature* **571**, 265-269 (2019). https://doi.org:10.1038/s41586-019-1326-9

18 Manolios, N., Papaemmanouil, J. & Adams, D. J. The role of ion channels in T cell function and disease. *Front Immunol* **14**, 1238171 (2023). https://doi.org:10.3389/fimmu.2023.1238171

19 Feng, Q. *et al.* Lactate increases stemness of CD8 + T cells to augment anti-tumor immunity. *Nat Commun* **13**, 4981 (2022). https://doi.org:10.1038/s41467-022-32521-8

20 Hart, G. T., Hogquist, K. A. & Jameson, S. C. Kruppel-like factors in lymphocyte biology. *J Immunol* **188**, 521-526 (2012). https://doi.org:10.4049/jimmunol.1101530

21 Abdelsamed, H. A. *et al.* Beta cell-specific CD8(+) T cells maintain stem cell memory-associated epigenetic programs during type 1 diabetes. *Nat Immunol* **21**, 578-587 (2020). https://doi.org:10.1038/s41590-020-0633-5

22 Sun, Q. *et al.* STAT3 regulates CD8+ T cell differentiation and functions in cancer and acute infection. *J Exp Med* **220** (2023). https://doi.org:10.1084/jem.20220686

23 Zheng, C. *et al.* Transcriptomic profiles of neoantigen-reactive T cells in human gastrointestinal cancers. *Cancer Cell* **40**, 410-423 e417 (2022). https://doi.org:10.1016/j.ccell.2022.03.005

24 Belk, J. A., Daniel, B. & Satpathy, A. T. Epigenetic regulation of T cell exhaustion. *Nat Immunol* **23**, 848-860 (2022). https://doi.org:10.1038/s41590-022-01224-z

25 Wherry, E. J. *et al.* Molecular signature of CD8+ T cell exhaustion during chronic viral infection. *Immunity* **27**, 670-684 (2007). https://doi.org:10.1016/j.immuni.2007.09.006

26 Doering, T. A. *et al.* Network analysis reveals centrally connected genes and pathways involved in CD8+ T cell exhaustion versus memory. *Immunity* **37**, 1130-1144 (2012). https://doi.org:10.1016/j.immuni.2012.08.021

27 Trebak, M. & Kinet, J. P. Calcium signalling in T cells. *Nat Rev Immunol* **19**, 154-169 (2019). https://doi.org:10.1038/s41577-018-0110-7

28 Quintana, A., Griesemer, D., Schwarz, E. C. & Hoth, M. Calcium-dependent activation of T-lymphocytes. *Pflugers Arch* **450**, 1-12 (2005). https://doi.org:10.1007/s00424-004-1364-4

29 Hogan, P. G. Calcium-NFAT transcriptional signalling in T cell activation and T cell exhaustion. *Cell Calcium* **63**, 66-69 (2017). https://doi.org:10.1016/j.ceca.2017.01.014

30 Hogan, P. G., Chen, L., Nardone, J. & Rao, A. Transcriptional regulation by calcium, calcineurin, and NFAT. *Genes Dev* **17**, 2205-2232 (2003). https://doi.org:10.1101/gad.1102703

31 Martinez, G. J. *et al.* The transcription factor NFAT promotes exhaustion of activated CD8(+) T cells. *Immunity* **42**, 265-278 (2015). https://doi.org:10.1016/j.immuni.2015.01.006

32 Bian, Y. *et al.* Cancer SLC43A2 alters T cell methionine metabolism and histone methylation. *Nature* **585**, 277-282 (2020). https://doi.org:10.1038/s41586-020-2682-1

33 Caudill, M. A. *et al.* Intracellular S-adenosylhomocysteine concentrations predict global DNA hypomethylation in tissues of methyl-deficient cystathionine beta-synthase heterozygous mice. *J Nutr* **131**, 2811-2818 (2001). https://doi.org:10.1093/jn/131.11.2811

34 Zhang, N. Role of methionine on epigenetic modification of DNA methylation and gene expression in animals. *Anim Nutr* **4**, 11-16 (2018). https://doi.org:10.1016/j.aninu.2017.08.009

35 Hwang, J. W., Cho, Y., Bae, G. U., Kim, S. N. & Kim, Y. K. Protein arginine methyltransferases: promising targets for cancer therapy. *Exp Mol Med* **53**, 788-808 (2021). https://doi.org:10.1038/s12276-021-00613-y

36 Al-Hamashi, A. A., Diaz, K. & Huang, R. Non-Histone Arginine Methylation by Protein Arginine Methyltransferases. *Curr Protein Pept Sci* **21**, 699-712 (2020). https://doi.org:10.2174/1389203721666200507091952

37 Lam, J. & Wulff, H. The Lymphocyte Potassium Channels Kv1.3 and KCa3.1 as Targets for Immunosuppression. *Drug Dev Res* **72**, 573-584 (2011). https://doi.org:10.1002/ddr.20467

38 Rader, R. K. *et al.* T cell activation is regulated by voltage-dependent and calcium-activated potassium channels. *J Immunol* **156**, 1425-1430 (1996).

39 Cahalan, M. D. & Chandy, K. G. The functional network of ion channels in T lymphocytes. *Immunol Rev* **231**, 59-87 (2009). https://doi.org:10.1111/j.1600-065X.2009.00816.x

40 Vodnala, S. K. *et al.* T cell stemness and dysfunction in tumors are triggered by a common mechanism. *Science* **363** (2019). https://doi.org:10.1126/science.aau0135

41 Bachmann, M. *et al.* Pharmacological targeting of the mitochondrial calcium-dependent potassium channel KCa3.1 triggers cell death and reduces tumor growth and metastasis in vivo. *Cell Death Dis* **13**, 1055 (2022). https://doi.org:10.1038/s41419-022-05463-8

42 Wulff, H. *et al.* Design of a potent and selective inhibitor of the intermediate-conductance Ca2+-activated K+ channel, IKCa1: a potential immunosuppressant. *Proc Natl Acad Sci U S A* **97**, 8151-8156 (2000). https://doi.org:10.1073/pnas.97.14.8151

43 Beltra, J. C. *et al.* Developmental Relationships of Four Exhausted CD8(+) T Cell Subsets Reveals Underlying Transcriptional and Epigenetic Landscape Control Mechanisms. *Immunity* **52**, 825-841 e828 (2020). https://doi.org:10.1016/j.immuni.2020.04.014

44 McLane, L. M., Abdel-Hakeem, M. S. & Wherry, E. J. CD8 T Cell Exhaustion During Chronic Viral Infection and Cancer. *Annu Rev Immunol* **37**, 457-495 (2019). https://doi.org:10.1146/annurev-immunol-041015-055318

45 Thompson, E. D., Enriquez, H. L., Fu, Y. X. & Engelhard, V. H. Tumor masses support naive T cell infiltration, activation, and differentiation into effectors. *J Exp Med* **207**, 1791-1804 (2010). https://doi.org:10.1084/jem.20092454

46 Yu, P. *et al.* Priming of naive T cells inside tumors leads to eradication of established tumors. *Nat Immunol* **5**, 141-149 (2004). https://doi.org:10.1038/ni1029

47 Prokhnevska, N. *et al.* CD8(+) T cell activation in cancer comprises an initial activation phase in lymph nodes followed by effector differentiation within the tumor. *Immunity* **56**, 107-124 e105 (2023). https://doi.org:10.1016/j.immuni.2022.12.002

48 Sterner, R. C. & Sterner, R. M. CAR-T cell therapy: current limitations and potential strategies. *Blood Cancer J* **11**, 69 (2021). https://doi.org:10.1038/s41408-021-00459-7

49 Marofi, F. *et al.* CAR T cells in solid tumors: challenges and opportunities. *Stem Cell Res Ther* **12**, 81 (2021). https://doi.org:10.1186/s13287-020-02128-1

50 Du, H. *et al.* Antitumor Responses in the Absence of Toxicity in Solid Tumors by Targeting B7-H3 via Chimeric Antigen Receptor T Cells. *Cancer Cell* **35**, 221-237 e228 (2019). https://doi.org:10.1016/j.ccell.2019.01.002

51 Sun, Q. *et al.* Immune checkpoint therapy for solid tumours: clinical dilemmas and future trends. *Signal Transduct Target Ther* **8**, 320 (2023). https://doi.org:10.1038/s41392-023-01522-4

52 Scharping, N. E. *et al.* The Tumor Microenvironment Represses T Cell Mitochondrial Biogenesis to Drive Intratumoral T Cell Metabolic Insufficiency and Dysfunction. *Immunity* **45**, 374-388 (2016). https://doi.org:10.1016/j.immuni.2016.07.009

53 Franco, F., Jaccard, A., Romero, P., Yu, Y. R. & Ho, P. C. Metabolic and epigenetic regulation of T-cell exhaustion. *Nat Metab* **2**, 1001-1012 (2020). https://doi.org:10.1038/s42255-020-00280-9

54 Rudloff, M. W. *et al.* Hallmarks of CD8(+) T cell dysfunction are established within hours of tumor antigen encounter before cell division. *Nat Immunol* **24**, 1527-1539 (2023). https://doi.org:10.1038/s41590-023-01578-y

55 Shakiba, M. *et al.* TCR signal strength defines distinct mechanisms of T cell dysfunction and cancer evasion. *J Exp Med* **219** (2022). https://doi.org:10.1084/jem.20201966

56 Abe, B. T., Shin, D. S., Mocholi, E. & Macian, F. NFAT1 supports tumor-induced anergy of CD4(+) T cells. *Cancer Res* **72**, 4642-4651 (2012). https://doi.org:10.1158/0008-5472.CAN-11-3775

FIGURE 1

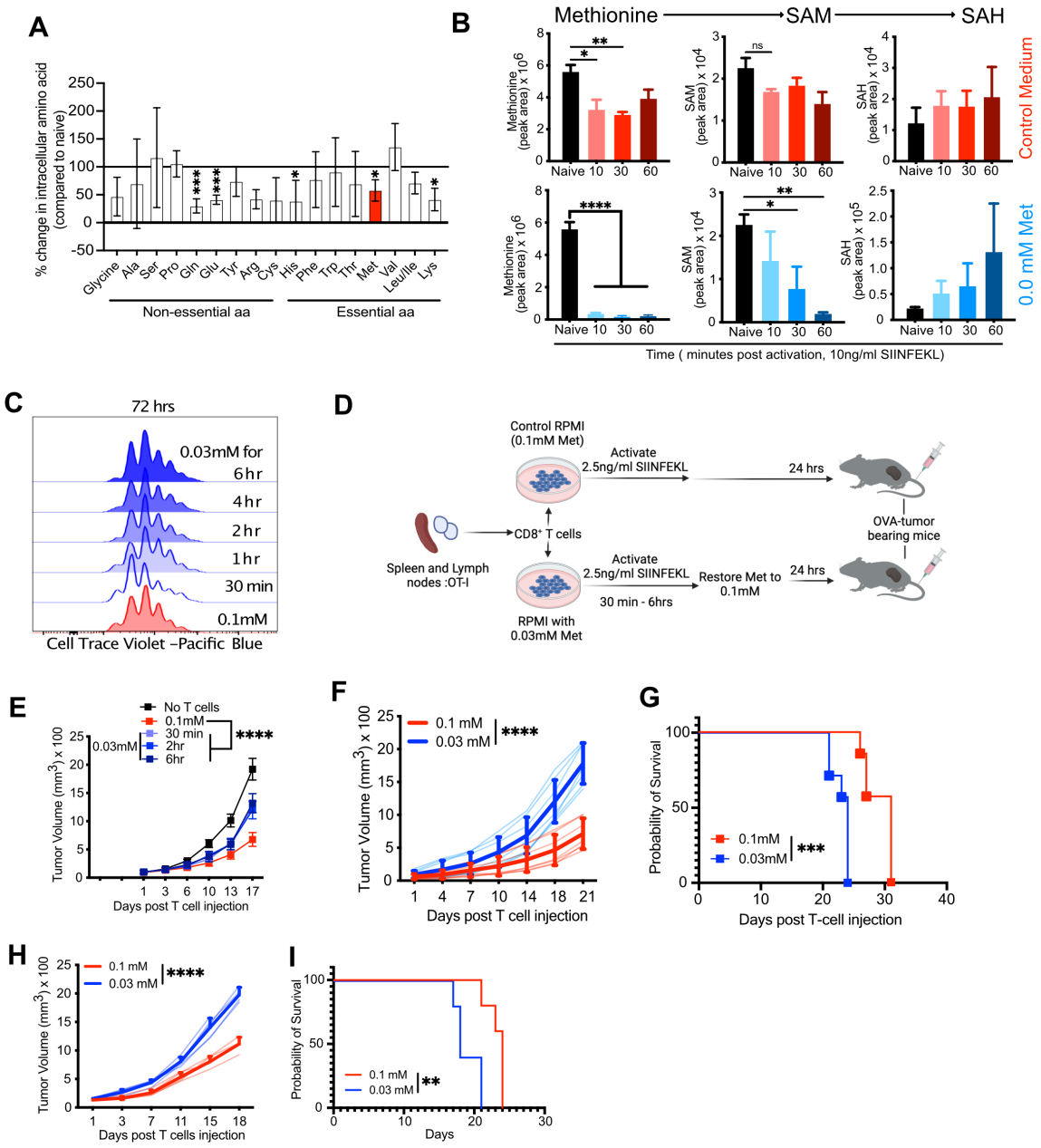

610

611 **Figure 1: TCR-mediated, rapid methionine consumption governs T cell effector function. a-**
612 **b,** Quantification of intracellular amino acids at 10 min (a) and SAM and SAH up to 60 min (b) in
613 OT-I T cells activated with 10 ng/ml SIINFEKL (n=3). **c,** T cell proliferation via cell-trace violet
614 staining of OT-I CD8^{+} T cells activated in either 0.1 mM Met or 0.03 mM Met for the indicated
615 times before restoration to 0.1 mM Met in 0.03 mM Met conditions and then analyzed 72 hrs post

616 activation (n=3). Representative of 3 samples per group. **d,** Schematic design for OT-I T cell
617 activation initially in 0.1 or 0.03 mM Met, followed by restoration of Met to 0.1 mM for 24 hrs
618 before injection into B16-OVA tumour-bearing mice. **e,** Tumour growth of B16-OVA in *Rag1*$^{-/-}$
619 treated with OT-I CD8^{+} T cells activated as described in (d) for 30 min-6hrs (n=5). **f-g,** Tumour
620 growth (f) and survival (g) of B16-OVA tumours in *Rag1*$^{-/-}$ mice after transfer of 24 hr-activated
621 OT-I T cells with first 30 min of stimulation being in 0.1 or 0.03 mM Met with 2.5ng/ml
622 SIINFEKL before restoration to 0.1 mM Met (n=5). **h-i,** Tumour growth (h) and survival (i) of
623 B16-OVA tumours treated with activated GP33^{+}-memory T cells as described in extended data
624 fig. 1d (n=5). Data are mean±s.e.m. Unpaired two-tailed Student's t-test (a, b), two-way ANOVA
625 (e, f, h), Mantel-Cox log rank test (g, i) and paired two-tailed Student's t-test (G-L) *P < 0.05, **P
626 < 0.01, ***P < 0.001, ****P < 0.0001.
627

FIGURE 2

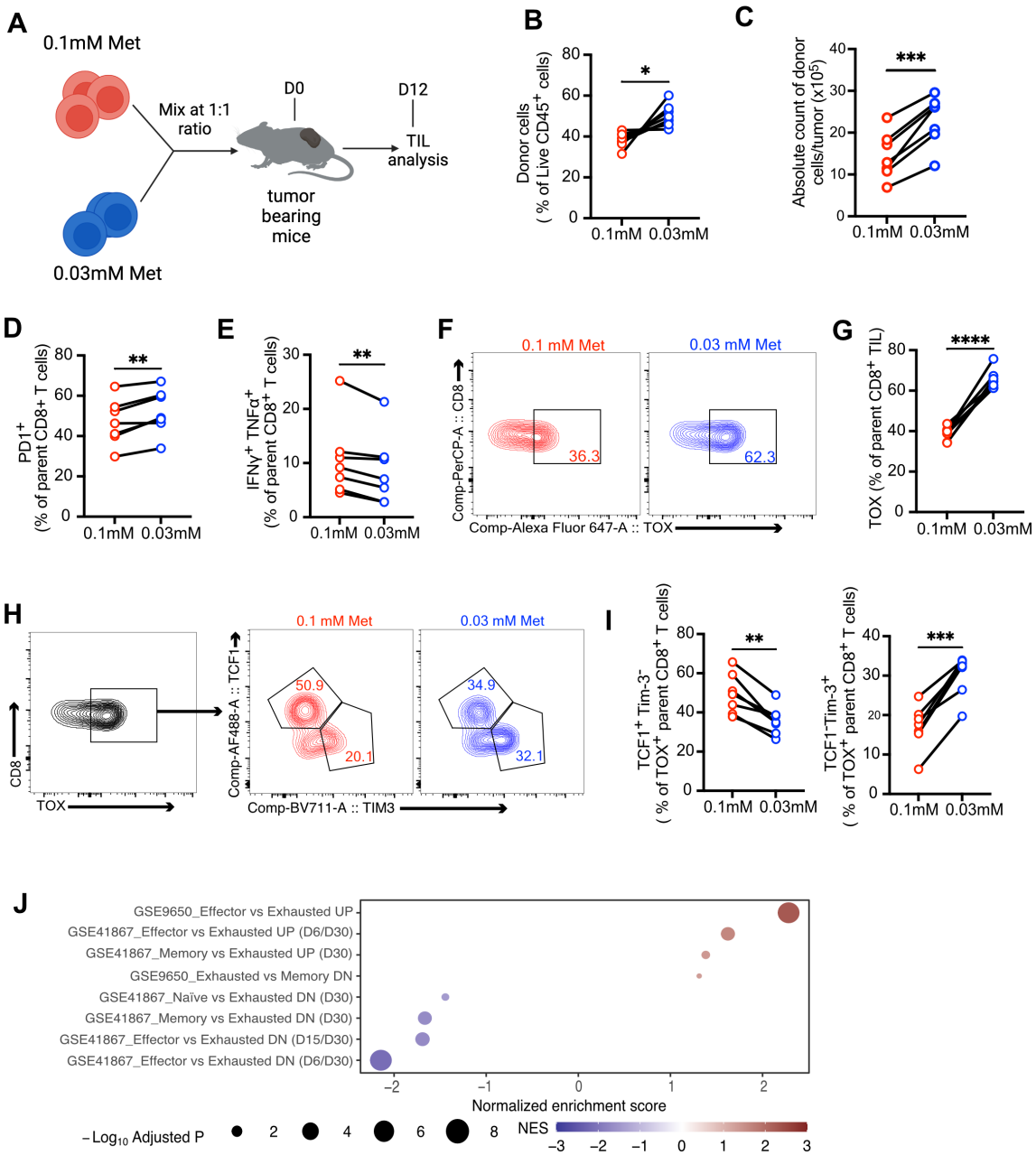

Figure 2: Reduced methionine availability during TCR signaling promotes T cell exhaustion. **a,** Schematic of experimental design. OT-I CD8^{+} T cells with different congenic markers were initially activated in 0.1 mM or 0.03 mM Met for 30 min with replenishment of Met in 0.03 mM to 0.1 mM Met for 24 hrs, transferred into B16-OVA tumour-bearing *Rag1*$^{-/-}$ mouse at a 1:1 ratio, and analyzed day 12 post T cell transfer. **b-c,** Frequencies (b) and absolute number (c) of

transferred T cells isolated from B16-OVA tumours at D12 post transfer (n=7). **d-e,** Frequency of $PD1^+$ and $IFN\gamma^+TNF\alpha^+$ OT-I $CD8^+$ TIL, initially activated in 0.1 mM and 0.03 mM Met and assessed at D12 post injection (as in a) (n=7). **f-g,** Contour plot (f) and frequency of TOX^+ cells (g) and of OT-I $CD8^+$ TIL as in d (n=7). **h-i,** Representative contour plot (h) and quantification (i) of TCF1 and Tim-3 expressing cells from TOX^+ $CD8^+$ TIL from OT-I $CD8^+$ T cells isolated at D12 post transfer as in (a) (n=7). **j,** T cell exhaustion gene sets in GSEA analysis of RNA-Seq of OT-I $CD8^+$ TIL on d9 post T cell injection as in Fig. 1f (n=4). Data are mean±s.e.m. paired two-tailed Student's t-test. *$P < 0.05$, **$P < 0.01$, ***$P < 0.001$.

FIGURE 3

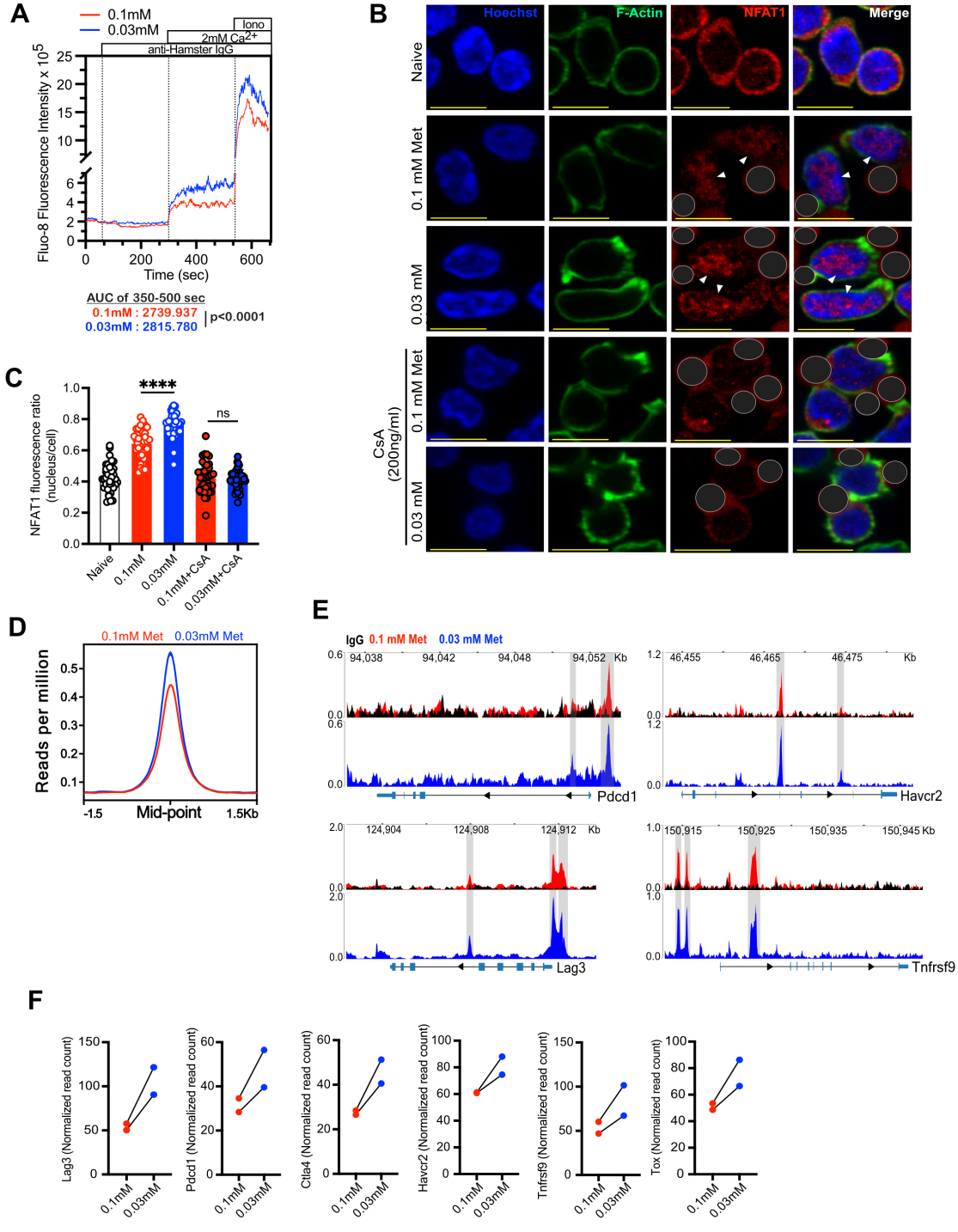

643

644

645

646 **Figure 3: Extracellular methionine availability regulates Ca^{2+}-mediated NFAT1 activity.**
647 **a,** Fluo-8 AM analysis of Ca^{2+} flux in $CD8^+$ T cells activated with anti-CD3 and anti-CD28 by
648 anti-hamster IgG crosslinking in either 0.1 mM or 0.03 mM Met containing Ca^{2+} Ringer solution
649 with addition of 2 mM Ca^{2+} to measure Ca^{2+} influx. The area under the curve is measured from
650 350-500 sec. Ionomycin then added as a positive control for maximal flux. Representative of 2
651 experiments. **b,** Representative images of T cells, cultured with or without anti-CD3/28 dynabeads
652 (dark grey masked), in 0.1 mM and 0.03 mM Met, with or without cyclosporin-A treatment for 30
653 min, stained with NFAT1 (red, marked), Hoechst (blue) and Phalloidin (green). **c,** Quantification
654 of NFAT1 intensity as nuclear to total cell ratio (c) (See Fig. S4A for unmasked figure). Scale
655 bar=10μm. (Each circle represents one cell, n=40 cells). **d,** Histogram of NFAT1 binding signals
656 (read count per million reads normalized to background) from NFAT1 CUT&RUN on T cells
657 initially activated in 0.1 or 0.03 mM Met for 30 min and assessed 24 hrs post activation. **e-f,**
658 NFAT1 CUT&RUN peaks at the known target genes (e) and quantification of known NFAT1-
659 binding regions of *Lag3, Pdcd1, Havcr2, Ctla4* and *Tnfrsf9 and Tox* (f, normalized read count (see
660 differential binding analysis)) in T cells initially activated in 0.1 or 0.03 mM Met for 30 min and
661 assessed 24 hrs post activation (n=2). Data are mean±s.e.m. Unpaired two-tailed Student's t-test
662 (C, D). *P < 0.05, **P < 0.01, ***P < 0.001, ****P < 0.0001.
663

FIGURE 4

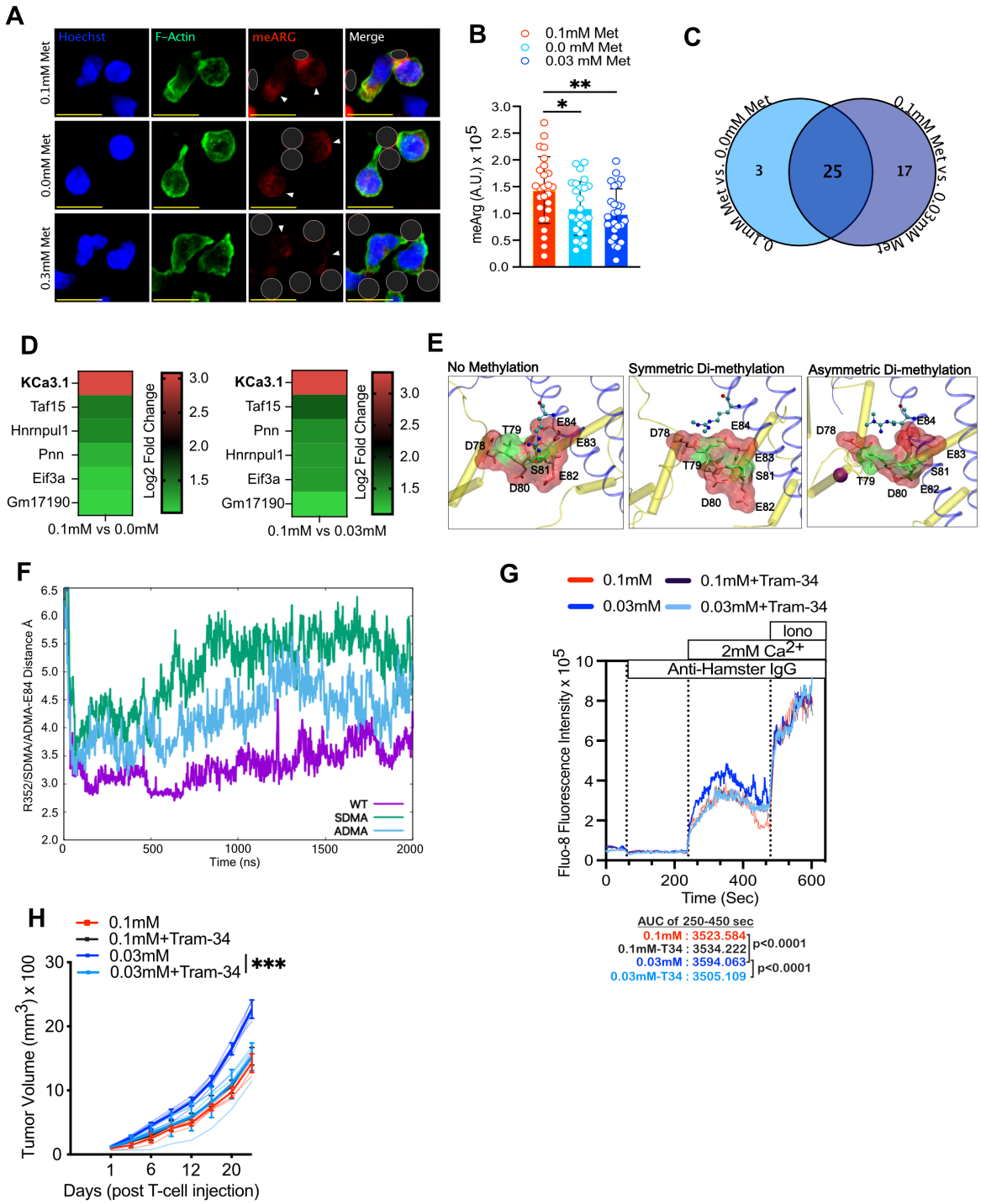

664

665

666 **Figure 4. Methionine mediated KCa3.1 methylation upon TCR activation regulates T cell**
667 **effector function.**
668 **a-b,** Representative images (a) and quantification (b) of methyl-arginine in $CD8^+$ T cells activated
669 with anti-CD3/28 dynabeads (circled in red channel images) in 0.1, 0.0, and 0.03 mM Met for 30
670 min, stained with pan-meArg (red, with arrows), Hoechst (blue), and Phalloidin (green) (scale
671 bar=10 μm) (each circle represents one cell. n= 25 cells). **c,** Venn diagram of enriched methyl-
672 arginine proteins at 30 min post activation of T cells in 0.1 mM vs 0.0 mM or 0.1 mM vs 0.03 mM
673 Met, as identified by TMT-MS. **d,** Heat-map (Log_2 fold change) of TMT-MS identified proteins
674 ($p<0.05$) with enriched methyl-arginine in T cells activated in 0.1 mM vs 0.0mM or 0.03 mM Met
675 by IgG crosslinking with anti-CD3 for 30 min (n=3). **e,** Predicted interaction of KCa3.1 monomer
676 (blue cartoon) with calmodulin (yellow cartoon) as un-methylated (left), SDMA (center) and
677 ADMA (right). The Calmodulin-binding pocket is represented as surface rendering with
678 interacting amino acids as sticks (negative charges in red, polar residues in green) and R352 as
679 ball and sticks; introduction of a hydrophobic methyl group (middle and bottom) weakens the
680 interactions between calmodulin and the KCa3.1 monomer. **f,** MD simulation analysis: Analysis
681 of variations of distance of salt bridge between calmodulin E84 and demethylated R352 WT
682 (purple), SDMA R352 (green) and ADMA R352 (blue) over the course of simulation time
683 (averaged across all four monomers, three MD trials). **g,** Fluo-8 AM analysis of Ca^{2+} flux in $CD8^+$
684 T cells activated with anti-CD3 and anti-CD28 by anti-hamster IgG crosslinking in Ca^{2+}-free
685 Ringer solution supplemented with either 0.1 mM or 0.03 mM Met and treated with either with
686 DMSO or 1μM TRAM-34. Area under the curve measured from 250-450 sec (representative of 2
687 experiments). **h,** Tumour growth of B16-OVA tumours in *Rag1*$^{-/-}$ mouse after transfer of OT-I
688 $CD8^+$ T cells activated in 0.1 mM or 0.03 mM Met with either DMSO or 1 μM TRAM-34 for 30
689 min and cultured for 24 hrs (n=5). Data are mean±s.e.m. Unpaired two-tailed Student's t-test (b),
690 2-way ANOVA (h), two-sample T-test (g) as described in the methods. *$P < 0.05$, **$P < 0.01$,
691 ***$P < 0.001$.
692

FIGURE 5

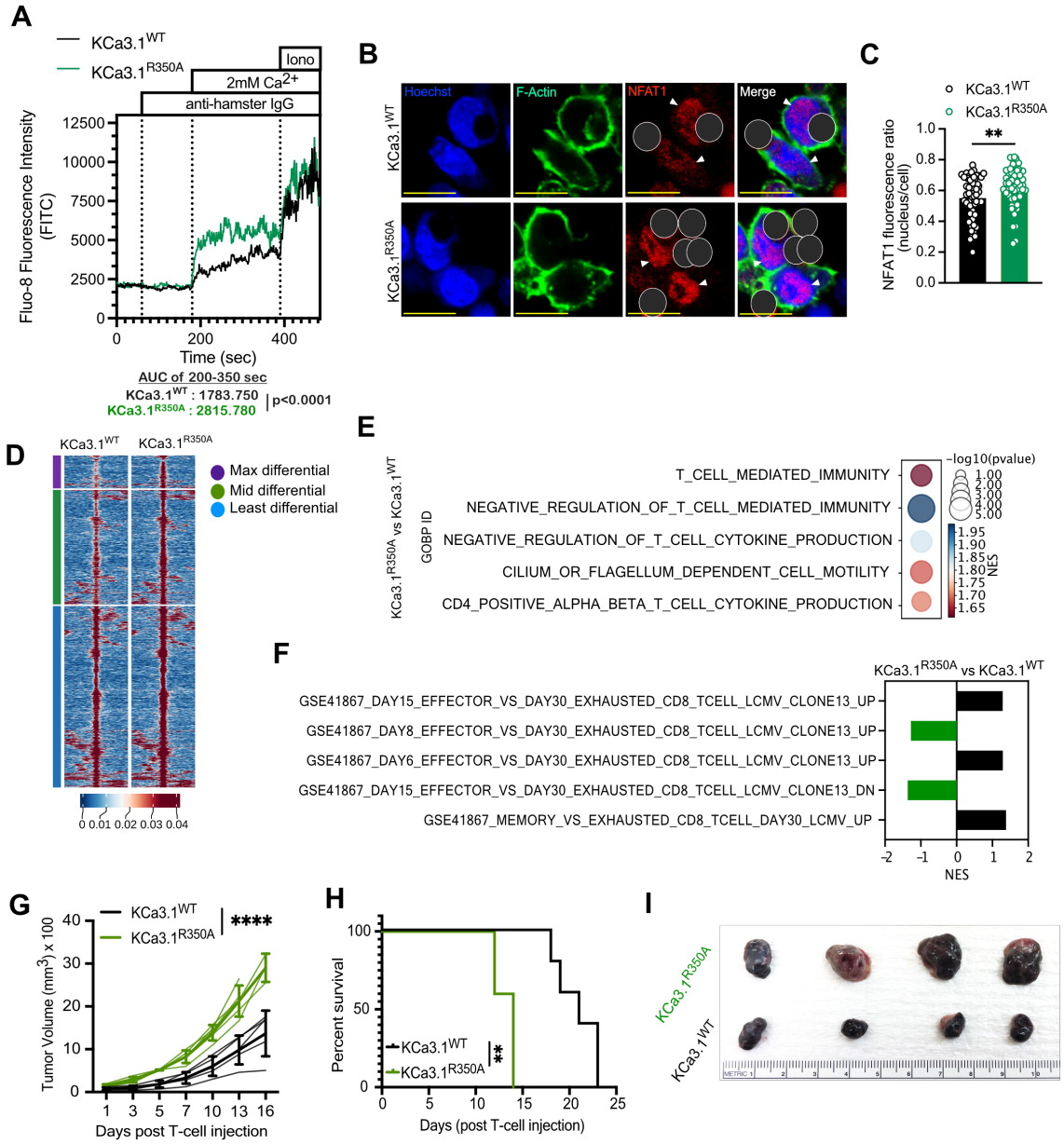

Figure 5. Ablation of KCa3.1 R350 methylation increased Ca^{2+}-mediated NFAT1 activity, promoting T cell dysfunction.

a, Fluo-8 analysis of Ca^{2+} flux in $KCa3.1^{WT}$ and $KCa3.1^{R350A}$ T cells activated with anti-CD3 and anti-CD28 by anti-hamster IgG crosslinking in Ca^{2+}-free Ringer solution. Area under the curve calculated from 200-350 sec. **b-c,** Representative image (c) and quantification of NFAT1intensity as nuclear to total cell ratio (c) in $KCa3.1^{WT}$ and $KCa3.1^{R350A}$ OT-I T cells activated for 30 min

700 with anti-CD3/28 dynabeads (dark grey masked) (See Extended Data Fig. 6F for unmasked figure),
701 scale bar=10 μm (each circle represents one cell, n=40 cells). **d,** Chromatin accessibility heatmap
702 of T cells expressing activated KCa3.1^{WT} or KCa3.1^{R350A} with each row representing peaks
703 ($p<0.05$ and log2 fold-change >1.5) displayed over the span of 2kb window with peak as center
704 (grouped from least to max differential region), analyzed 24 hrs post activation with 2.5ng/ml
705 SIINFEKL (n=3). **e,** GOBP terms associated with negative regulation of T cells enriched in OT-I
706 T cells expressing KCa3.1^{R350A} vs KCa3.1^{WT} activated as in (b) (n=3). **f,** T cell exhaustion gene
707 sets in GSEA analysis of differential accessible promoter reads from ATAC-Seq of OT-I T cells
708 expressing KCa3.1^{WT} or KCa3.1^{R350A}, activated with 2.5 ng/ml SIINFEKL for 24 hrs (n=3). **g-h,**
709 Tumour growth (g) and survival (h) of B16-OVA tumour-bearing RAG$^{-/-}$ mice after transfer of
710 KCa3.1^{WT} and KCa3.1^{R350A} OT-I T cells (n=5). **i,** B16-OVA tumours harvested at D12 post
711 transfer of KCa3.1^{WT} and KCa3.1^{R350A} OT-I T cells (n=4). Data are mean±s.e.m. Two-sample T-
712 test (a) as described in the methods, unpaired two-tailed Student's t-test (c), 2-way ANOVA (g),
713 and Mantel-Cox log rank test (h). **$P < 0.01$, ****$P < 0.0001$.
714

FIGURE 6

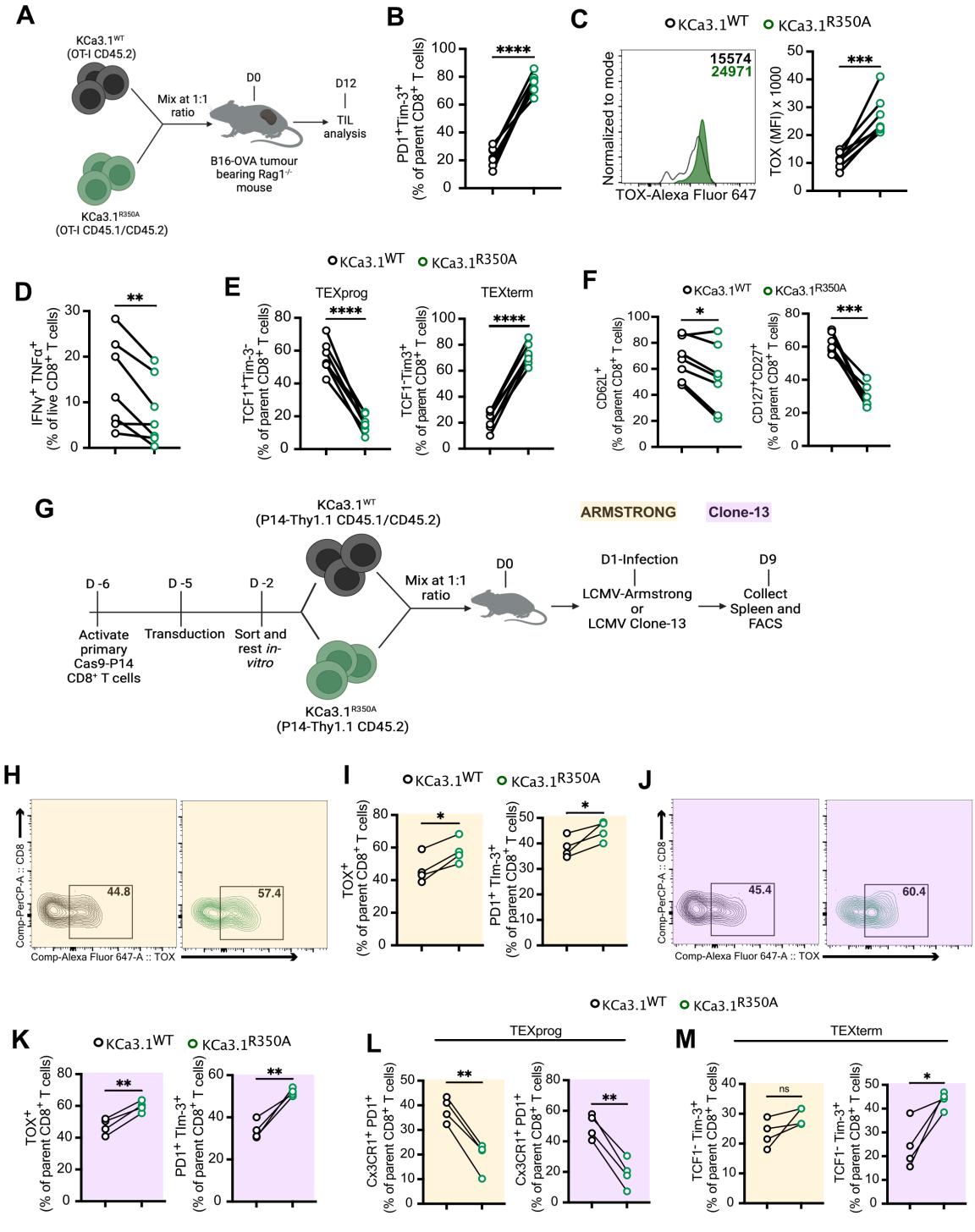

715

716

717 **Figure 6. Ablation of KCa3.1 R350 methylation promotes T cell exhaustion in tumours and**
718 **infection models.**
719 **a,** Schematic of experimental design to assess congenically distinct KCa3.1^{WT} and KCa3.1^{R350A}
720 OT-I T cells that were mixed at a 1:1 ratio and transferred into B16-OVA tumour-bearing *Rag1*$^{-/-}$
721 mice and analyzed day 12 post T cell transfer. **b-d** Frequency of Tim-3^{+}PD1^{+} (b), histogram and
722 quantification of TOX MFI (c), and frequency of IFNγ^{+}TNFα^{+} (d) among KCa3.1^{WT} and
723 KCa3.1^{R350A} OT-I TIL at D12 post T-cell transfer as in (a) (n=7). **e,** Frequency of TCF1^{+}Tim-3^{-}
724 TEXprog and TCF1^{-}Tim-3^{+} TEXterm in KCa3.1^{WT} and KCa3.1^{R350A} OT-I TIL at D12 post T-cell
725 transfer as in (a) (n=7). **f,** Expression of memory markers CD62L and CD127^{+}CD27^{+} on OT-I T
726 cells expressing KCa3.1^{WT} or KCa3.1^{R350A} isolated at D12 post transfer into B16-OVA tumour-
727 bearing mice as in (a) (n=7). **g,** Schematic of experimental design to assess congenically distinct
728 KCa3.1^{WT} and KCa3.1^{R350A} Thy1.1 P14 T cells that were mixed at a 1:1 ratio and transferred into
729 WT mice infected with either LCMV-Armstrong or LCMV-Clone-13. Spleens were analyzed at
730 D9 post infection. **h-i,** Expression of TOX (h) and frequency of TOX^{+} and PD1^{+}Tim-3^{+} (i) in
731 KCa3.1^{WT} and KCa3.1^{R350A} P14 CD8^{+} T cells from spleens at D9 post infection with LCMV-
732 Armstrong (n=4). **j-k,** Expression of TOX (j) and frequency of TOX^{+} and PD1^{+}Tim-3^{+} (k) in
733 KCa3.1^{WT} and KCa3.1^{R350A} P14 CD8^{+} T cells from spleens at D9 post infection with LCMV-
734 Clone-13 (p) (n=4). **l-m,** Frequency of CX3CR1^{+}PD1^{+} TEXprog (l) and TCF1^{-}Tim-3^{+} TEXterm
735 (m) in KCa3.1^{WT} and KCa3.1^{R350A} P14 CD8^{+} T cells from spleens at D9 post infection as in (g)
736 (n=4). Data are mean±s.e.m. Paired two-tailed Student's t-test. *P < 0.05, **P < 0.01, ***P <
737 0.001, ****P < 0.0001.

FIGURE 7

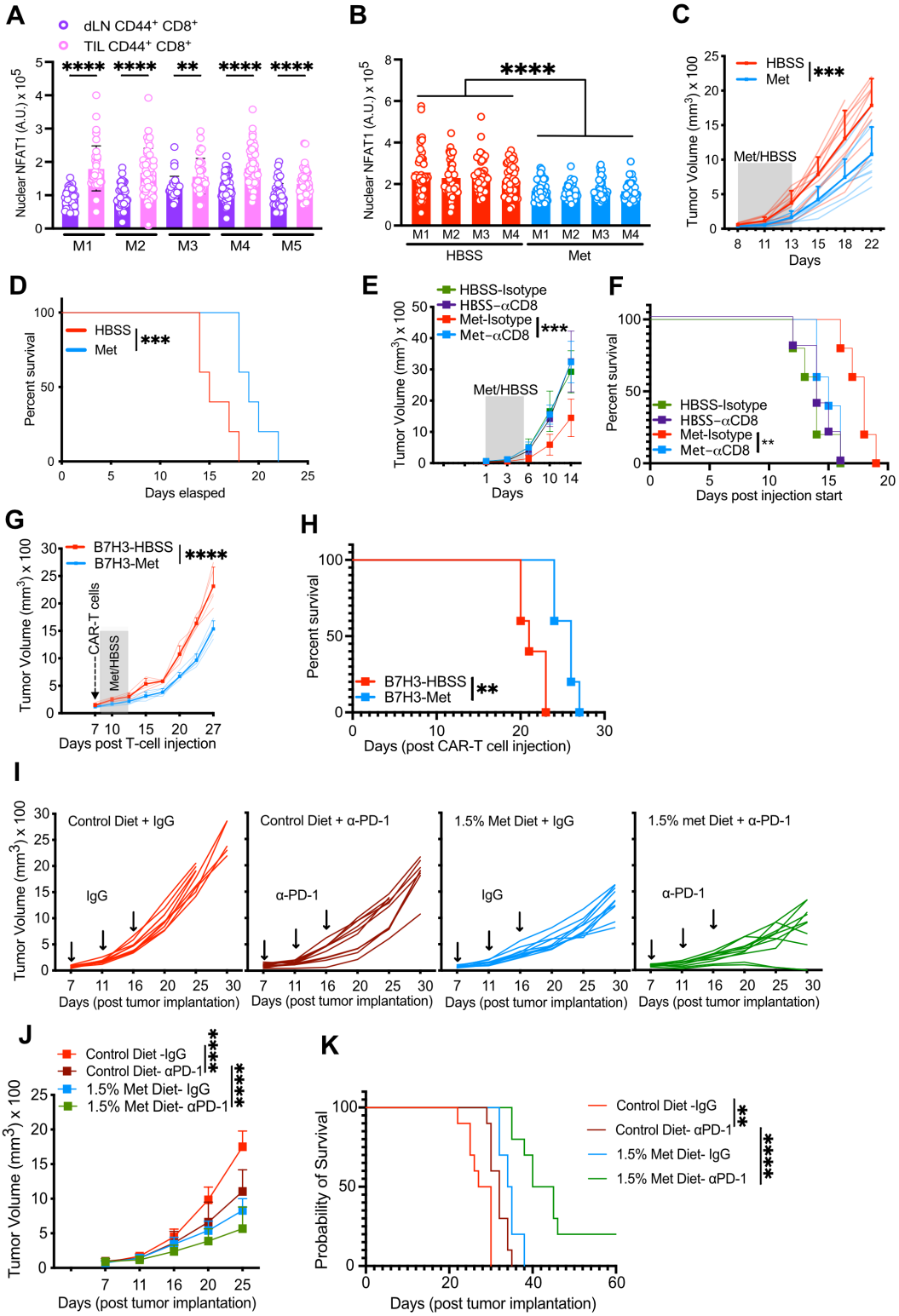
A
dLN CD44+ CD8+
TIL CD44+ CD8+
Nuclear NFAT1 (A.U.) x 10^5
M1 M2 M3 M4 M5
B
Nuclear NFAT1 (A.U.) x 10^5
HBSS
Met
C
HBSS
Met
Met/HBSS
Tumor Volume (mm3) x 100
Days
D
HBSS
Met
Percent survival
Days elasped
E
HBSS-Isotype
HBSS-αCD8
Met-Isotype
Met-αCD8
Met/HBSS
Tumor Volume (mm3) x 100
Days
F
HBSS-Isotype
HBSS-αCD8
Met-Isotype
Met-αCD8
Percent survival
Days post injection start
G
B7H3-HBSS
B7H3-Met
CAR-T cells
Met/HBSS
Tumor Volume (mm3) x 100
Days post T-cell injection
H
B7H3-HBSS
B7H3-Met
Percent survival
Days (post CAR-T cell injection)
I
Control Diet + IgG
IgG
Control Diet + α-PD-1
α-PD-1
1.5% Met Diet + IgG
IgG
1.5% met Diet + α-PD-1
α-PD-1
Tumor Volume (mm3) x 100
Days (post tumor implantation)
J
Control Diet -IgG
Control Diet- αPD-1
1.5% Met Diet- IgG
1.5% Met Diet- αPD-1
Tumor Volume (mm3) x 100
Days (post tumor implantation)
K
Control Diet -IgG
Control Diet- αPD-1
1.5% Met Diet- IgG
1.5% Met Diet- αPD-1
Probability of Survival
Days (post tumor implantation)

739 **Figure 7. Acute methionine supplementation promotes CD8$^+$ T cell-mediated tumour control**
740 **and enhances ICB treatment.**
741 **a,** Nuclear NFAT1 quantification in CD44$^+$CD8$^+$ T cells isolated from B16 tumours and respective
742 dLNs at D9 post implantation (each circle represents one cell, n=40 cells, n=5). **b,** Quantification
743 of nuclear NFAT1 in CD44$^+$ CD8$^+$ T cells isolated from B16 tumours after 5 days of peri-tumoural
744 supplementation of 50 μl HBSS or 61 μM Met per day (each circle represents one cell, n=40 cells,
745 n=4). **c-d,** Tumour growth (c) and survival (d) of B16 tumour-bearing WT mice, supplemented
746 either with HBSS or 61 μM Met peri-tumourally for five days as in (b) (n=10). **e-f,** B16 tumour
747 growth (e) and survival (f) of WT mice, treated intraperitoneally with IgG isotype or anti-CD8
748 antibody at D1 and D3 and treated peri-tumourally with HBSS or Met from D7-D12 as in (b) (n=5,
749 representative of two experiments). **g-h,** Tumour growth (g) and survival (h) of F420 tumour-
750 bearing *Rag1*$^{-/-}$ mice injected with B7-H3 CAR T-cells at D0 and peri-tumourally treated with
751 HBSS or Met from D1-D6 as in (b) (n=5). **i-k,** Tumour growth (i, j) and survival (k) of MC38
752 tumour-bearing WT mice, treated either with anti-PD1 or IgG-isotype (shown by arrows in i) and
753 fed with either control (1% Met) or Met-rich (1.5% Met) diet as shown in Extended Data Fig. 10H
754 (n=10). Data are mean±s.e.m. Unpaired two-tailed Student's t-test (a), 2-way ANOVA (c, e, g and
755 j), and Mantel-Cox log rank test (d, f, h and k). Statistical analysis of (b) is described in methods.
756 *P < 0.05, **P < 0.01, ***P < 0.001, ****P < 0.0001.
757

Extended Data Fig. 1

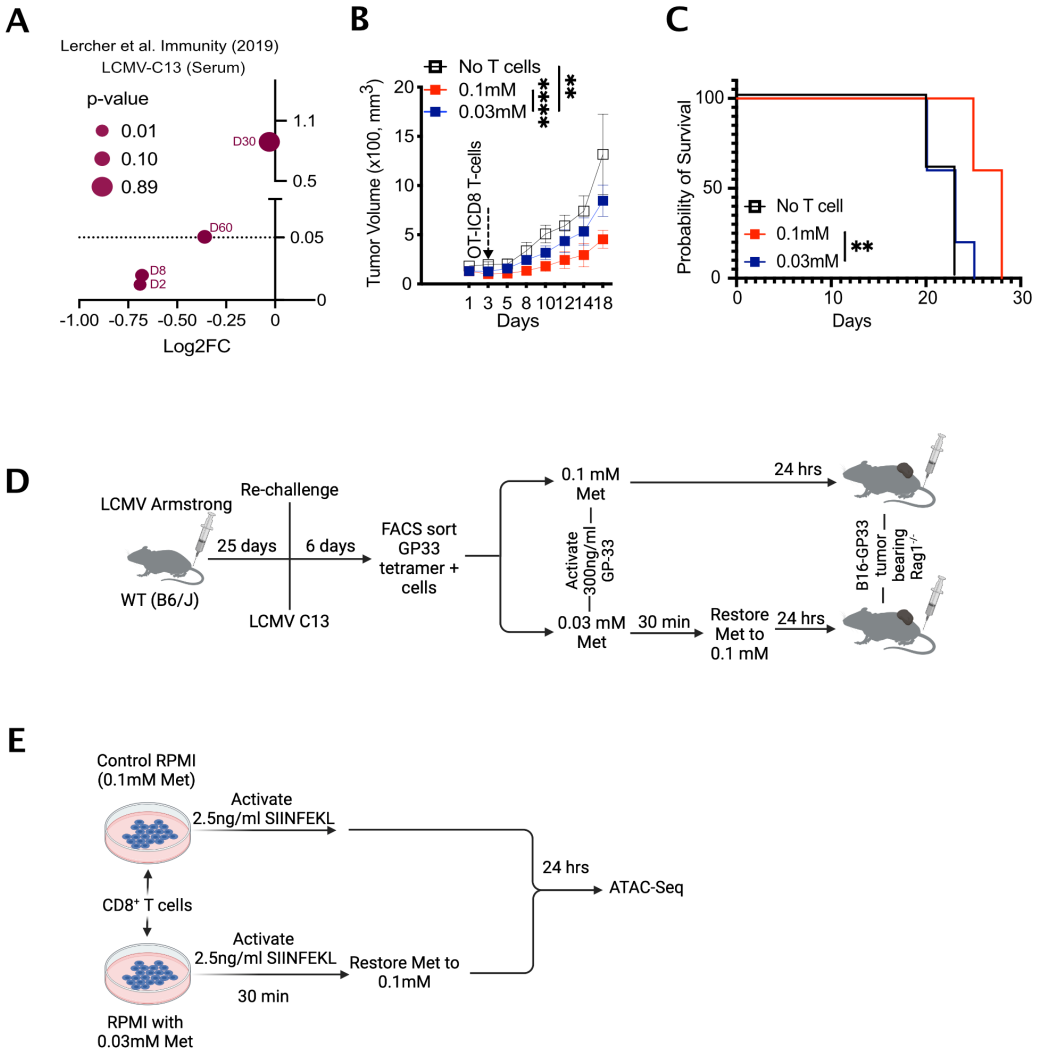

Extended Data Figure 1. Methionine availability during TCR activation determines T cell fate.

a, Log2FC in serum Met levels post LCMV-C13 chronic infection analyzed by Lercher et. al, *Immunity,* 2019 (ref. 7). **b-c,** Tumour growth (b) and survival (c) of B16-OVA tumour-bearing WT mice treated with or without OT-I $CD8^+$ T cells activated in 0.1 or 0.03 mM Met for 30 min before restoring Met to 0.1 mM in 0.03 mM Met for 24 hrs, as described in Fig. 1d (n=5). **d,** Schematic of experimental design for generation of LCMV-GP33 specific memory T cells, which were then activated as described in (Fig. 1d) before injection into B16-OVA tumour-bearing *Rag1*$^{-/-}$ mice. **e,** Schematic design for ATAC-Seq on OT-I T cell activation initially in 0.1 or 0.03 mM

768 Met followed by restoration of Met to 0.1 mM for 24 hrs. Data are mean±s.e.m. 2-way ANOVA
769 (b), and Mantel-Cox log rank test (c). **$P < 0.01$, ***$P < 0.001$.
770

Extended Data Fig. 2

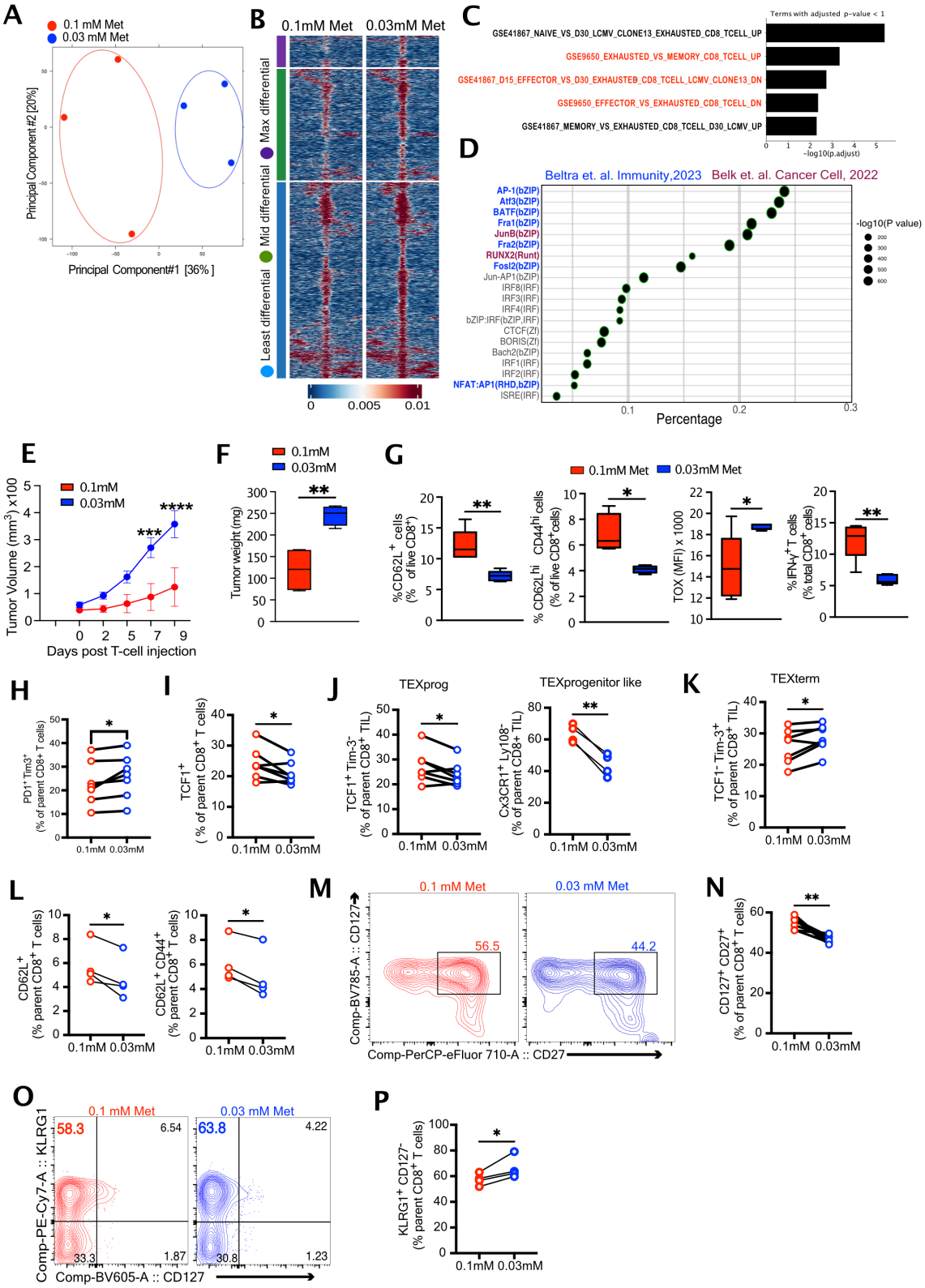

772 **Extended Data Figure 2. Reduced methionine during TCR activation promotes T cell**
773 **exhaustion.**
774 **a,** PCA analysis of ATAC-Seq of OT-I T cells activated with 2.5ng/ml SIINFEKL in 0.1 mM and
775 0.03 mM Met and cultured in 0.1 mM Met for 24 hrs. n=3. **b,** Chromatin accessibility heatmap of
776 T cells initially activated in 0.1 or 0.03 mM Met with each row representing peaks ($p<0.05$ and
777 log2 fold-change >1.5) displayed over the span of 2kb window with peak as center (grouped from
778 least to max differential region), analyzed from ATAC-Seq from (a). (n=3). **c,** Over-representation
779 analysis of the DAR from (b) showing the top 5 genesets associated with exhaustion. **d,** Homer
780 analysis of (a) showing top 20 motifs and their percent coverage. Colour corresponds to the
781 common exhaustion-associated motifs also described in the indicated studies (blue and purple). **e-**
782 **f,** Tumour growth (e) and weight (f) of B16-OVA tumour-bearing *Rag1*$^{-/-}$ mice injected with OT-
783 I T cells as in (Fig. 1d) (n=5). **g,** Frequency of CD62L^{+}, Tcm (CD62L^{hi} CD44^{hi}), TOX expression
784 (MFI) and IFN-γ^{+} in OT-I CD8^{+} TIL isolated from B16-OVA tumour-bearing *Rag1*$^{-/-}$ mice at D9
785 post-injection with OT-I T cells activated as in Fig. 1d (n=5). **h,** Frequency of PD1^{+} Tim-3^{+} on
786 OT-I CD8^{+} T cells at D12 post transfer of OT-I T cells as in Fig. 2a (n=7). **i,** Frequency of TCF1^{+}
787 on OT-I CD8^{+} T cells at D12 post transfer of OT-I T cells as in Fig. 2a (n=7). **j-l,** Frequency of
788 TCF1^{+}Tim-3^{-} TEXprog, CX3CR1^{+}Ly108^{+} TEXprogenitor-like (j) and, TCF1^{-}Tim-3^{+} TEXterm (k)
789 CD62L^{+} T memory and CD62L^{+}CD44^{+} T central memory cells (l) in OT-I CD8^{+} T cells as in Fig.
790 2a (n=7, n=4). **m-p,** Representative contour plot and quantification of CD127^{+}CD27^{+} memory
791 cells (m, n) and KLRG1^{+}CD127^{-} terminal effector cells (o, p) in OT-I CD8^{+} TIL isolated at D12
792 post of cells activated as in Fig. 1d into B16-OVA tumour-bearing *Rag1*$^{-/-}$ mice, as in Fig. 2a (n=4).
793 Data are mean±s.e.m. Statistical analyses performed using 2-way ANOVA (e), unpaired two-tailed
794 Student's t-test (f, g) paired two-tailed Student's t-test (h-p). *$P < 0.05$, **$P < 0.01$, ***$P < 0.001$.
795

Extended Data Fig. 3

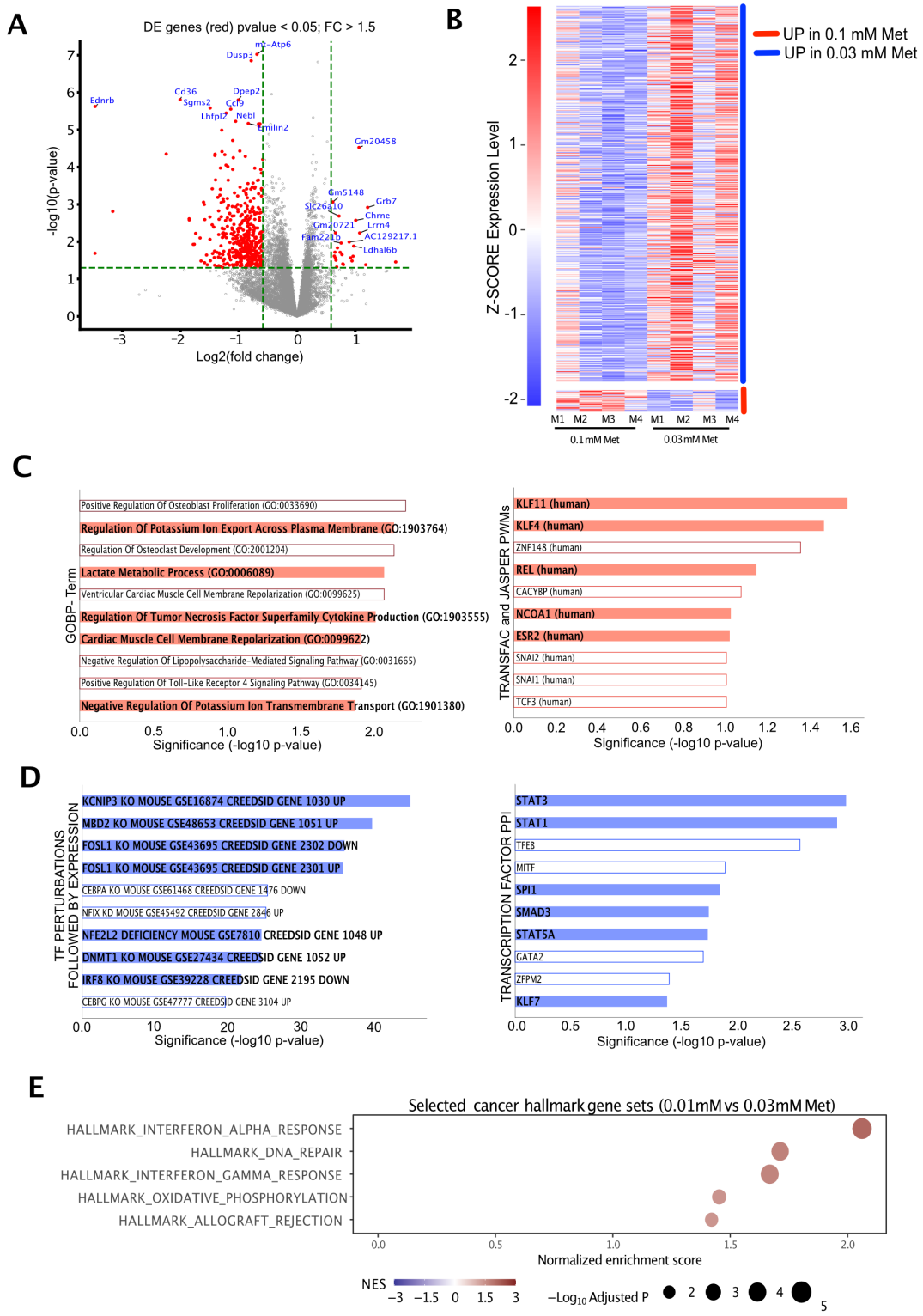

796

797 **Extended Data Figure 3. RNA-Seq analysis shows enrichment of exhaustion signature in low**
798 **Met.**
799 **a,** Volcano plot and top ten differentially expressed genes (red) (0.1 mM vs 0.03 mM, $p<0.05$,
800 FC>1.5) from OT-I $CD8^+$ TIL isolated from mice injected with OT-I T cells, initially activated in
801 0.1 mM Met or 0.03 mM Met (as in Fig. 1d), at day 9 post injection into B16-OVA tumour-bearing
802 mice (n=4). **b,** Heatmap of DE genes, which shows increased expression in cells initially activated
803 in either 0.03 mM Met or 0.1 mM Met from the RNAseq in (a) (n=4). **c,** Over-representation
804 analysis of DE genes with higher expression in TIL initially activated in 0.1 mM Met, showing
805 enrichment of biological processes and transcription factors associated with T cell effector
806 function and regulation. **d,** Over-representation analysis of DE genes with higher expression in
807 TIL initially activated in 0.03 mM Met, showing enrichment of gene sets and transcription factors
808 associated with promotion and maintenance of the exhausted T cell state. **e,** GSEA analysis of
809 hallmark genesets as analyzed from RNA-Seq of OT-I TIL initially activated in 0.1 or 0.03 mM
810 Met, isolated from B16-OVA tumours at D9 post transfer (n=4). RNA-Seq statistics were applied
811 as described in methods.
812

Extended Data Fig. 4

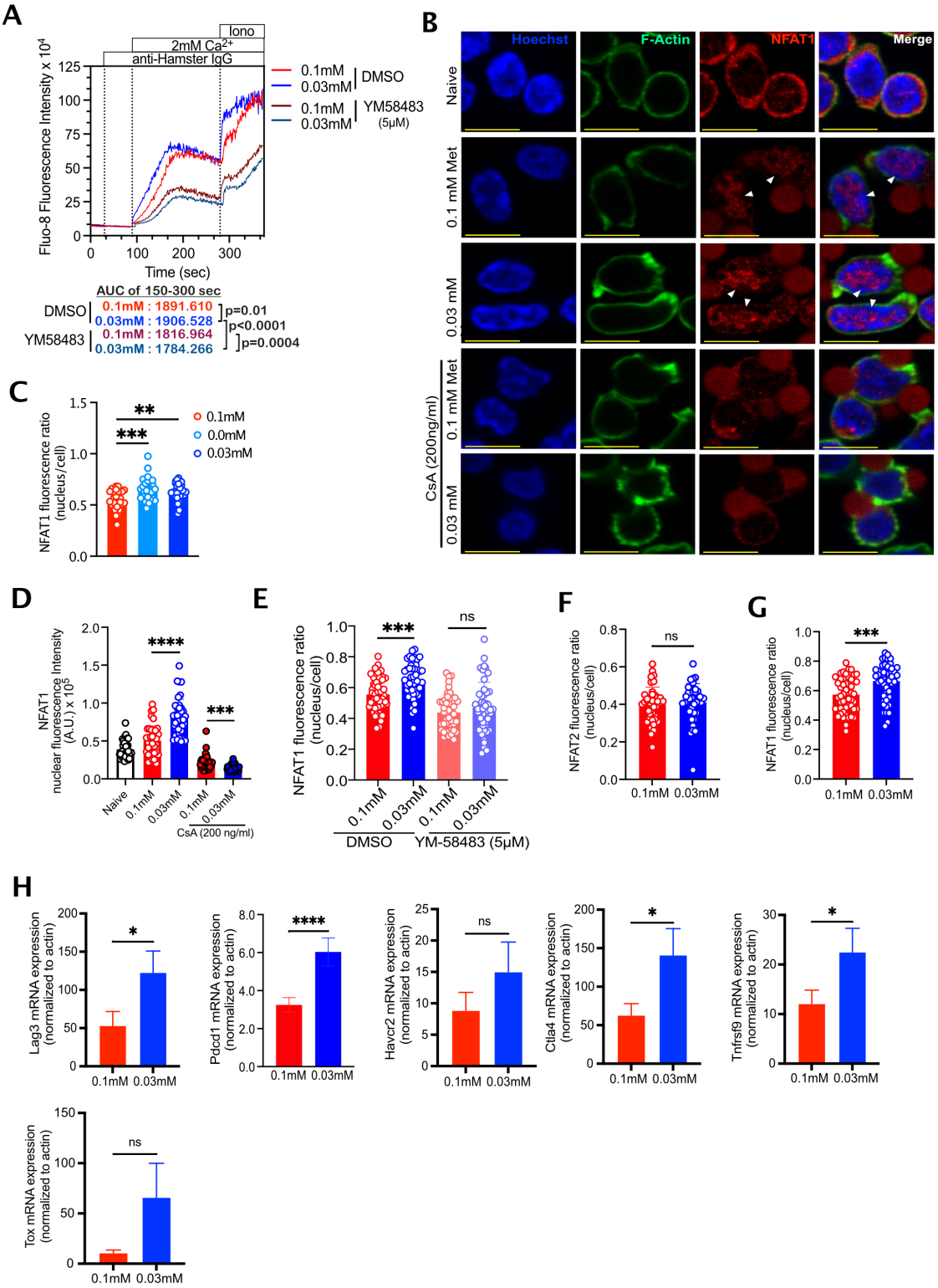

814 **Extended Data Figure 4. Met limitation results in increased TCR-mediated NFAT1**
815 **activation.**
816 **a,** Fluo-8 AM analysis of Ca^{2+} flux in $CD8^+$ T cells activated with anti-CD3 and anti-CD28 and
817 anti-hamster IgG crosslinking in Ca^{2+}-free Ringer solution containing either 0.1 mM or 0.03 mM
818 Met and treated for one hour with DMSO or 5μM YM58483. Area under the curve calculated from
819 150-300 sec (n=2). **b,** Un-edited image of Figure. 3b showing the unmasked, red anti-CD3/38
820 dynabeads which are masked grey in the main figure to highlight NFAT1 staining. **c,** NFAT1
821 intensity quantification (nuclear to total cell ratio) of $CD8^+$ T cells activated in either 0.1 mM, 0.00
822 mM or 0.03 mM Met for 30 min with anti CD3/28 dynabeads and stained for NFAT1 (each circle
823 represents one cell, n=40 cells). **d,** Quantification of nuclear NFAT1 from the experiment shown
824 in Figure 3b. **e,** NFAT1 intensity quantification (nuclear to total cell ratio) of $CD8^+$ T cells
825 activated for 30 min by CD3/28 dynabeads in either 0.1 mM or 0.03 mM Met in the presence of
826 DMSO or 5μM YM58483 (each circle represents one cell, n=40 cells). **f,** NFAT2 quantification
827 (nuclear to total cell ratio) of $CD8^+$ T cells, activated in 0.1 mM or 0.03 mM Met for 30 min with
828 anti-CD3/28 dynabeads (each circle represents one cell, n=40 cells). **g,** NFAT1 quantification
829 (nuclear to total cell ratio) of previously activated OT-I T cells, treated with anti-CD3/28
830 dynabeads for 30 min. T cells were initially activated with 2.5ng/ml SIINFEKL for 24 hrs in
831 control medium and rested with 10 ng/ml mIL-7 for 48 hrs (each circle represents one cell, n=40).
832 **h,** Normalized RNA expression quantified by quantitative-PCR performed 24 hrs post activation
833 of OT-I $CD8^+$ T cells activated with 2.5 ng/ml SIINFEKL in 0.1 mM or 0.03 mM Met for 30 min
834 followed by 0.1 mM Met (n=6). Data are mean±s.e.m. Two-sample T-test (a) as described in the
835 methods, unpaired two-tailed Student's t-test (c-g) and one-tailed Student's t-test (h). *$P < 0.05$,
836 **$P < 0.01$, ***$P < 0.001$, ****$P < 0.0001$.
837
838

Extended Data Fig. 5

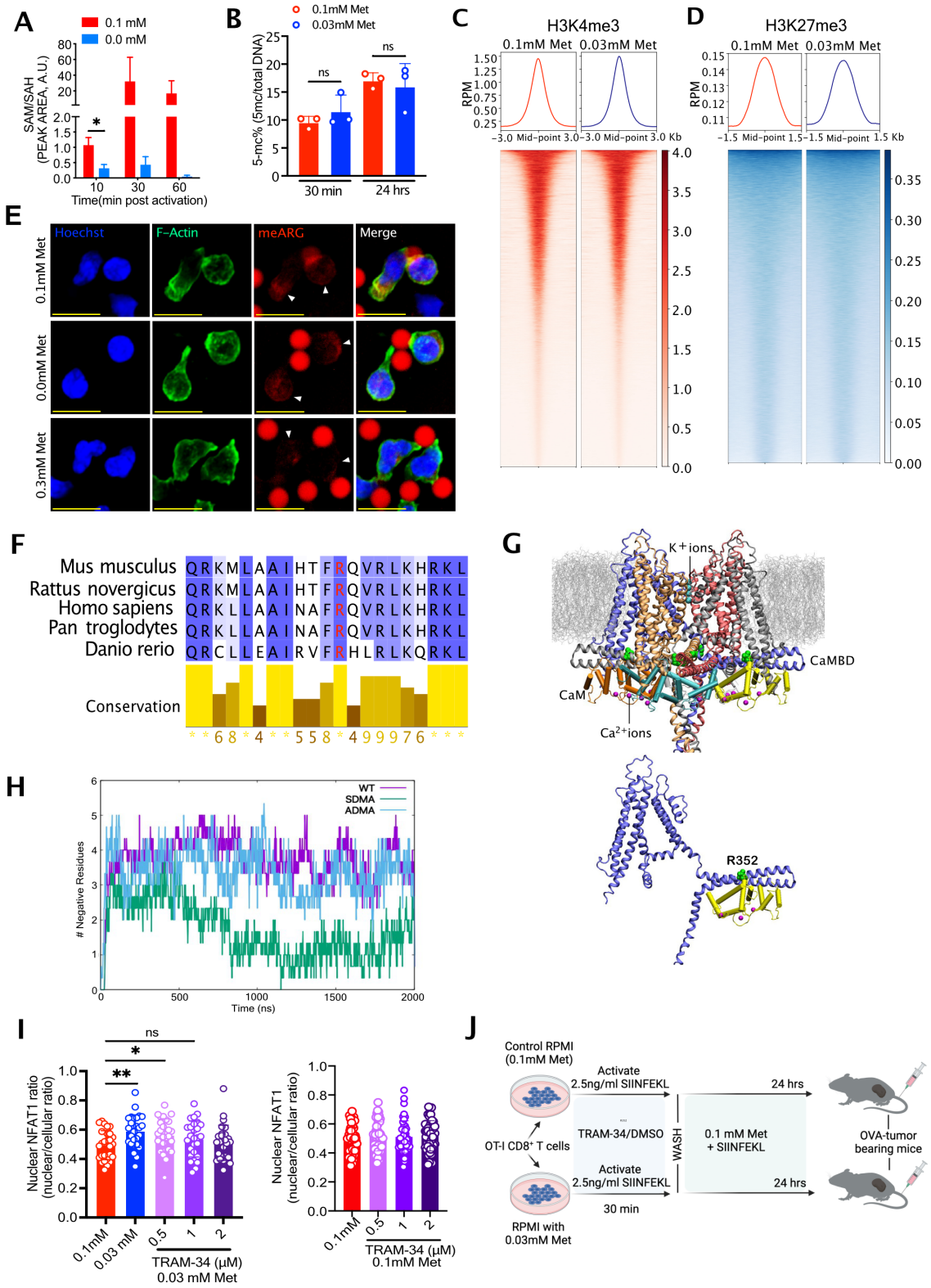

840 **Extended Data Figure 5. Initial Met limitation doesn't affect DNA or histone methylation**
841 **but alters KCa3.1 arginine methylation.**
842 **a,** Methylation potential (SAM/SAH) of 10 ng/ml SIINFEKL activated OT-I T cells in 0.1 mM or
843 0.0 mM Met at 10, 30 and 60 min (n=3). **b,** % 5-methylcytosine (%5-mc) of OT-I $CD8^+$ T cells
844 activated with 2.5 ng/ml SIINFEKL in 0.1 mM or 0.03 mM Met for 30 min, then 0.1 mM Met for
845 24 hr (n=3). **c-d,** Histograms (top) and heat-map (bottom) of H3K4me3 (c) and H3K27me3 (d)
846 CUT&RUN reads (read count per million, normalized to background) in OT-I $CD8^+$ T cells
847 activated initially in 0.1 mM or 0.03 mM Met with restoration to 0.1 mM after 30 min and
848 processed at 24 hrs post activation (n=3). **e,** Un-edited image of Figure. 4a showing the unmasked,
849 red CD3/38 dynabeads which are masked grey in the main figure to highlight me-Arg staining. **f,**
850 Conserved arginine (highlighted red) in KCa3.1 as analyzed by protein-BLAST in multiple species
851 and visualized using Jalview. **g,** Tetrameric assembly of human KCa3.1-Calmodulin complex
852 within the membrane (top). KCa3.1 is represented as ribbons and calmodulin quartet as cartoon
853 with interacting Ca^{2+} ions as purple spheres. K^+ ions are represented as cyan spheres. KCa3.1
854 monomer (blue) is shown in complex with calmodulin (yellow) along with demethylated arginine-
855 352 (green) (bottom). **h,** MD simulations analysis: Illustration of total count of negatively charged
856 residues within a 4Å radius of all four R352/SDMA/ADMA of huKCa3.1 the course of simulation
857 time (averaged across all four monomers, three MD trials). **i,** NFAT1 quantification (nuclear to
858 total cell ratio) in OT-I $CD8^+$ T cells activated for 30 min with anti CD3/28 dynabeads in 0.03 mM
859 Met (left) or 0.1 mM Met (right) in the presence of 0.5, 1 or 2 μM TRAM-34 (each circle represents
860 one cell, n=45). **j,** Schematic design for OT-I T cell activation initially in 0.1 or 0.03 mM Met,
861 treated with DMSO or TRAM-34 for 30 min, followed by washing and culturing in 0.1 mM
862 Met+SIINFEKL (2.5ng/ml) for 24 hrs before injection into B16-OVA tumour-bearing *Rag1*$^{-/-}$
863 mice. Data are mean±s.e.m. Unpaired one-tailed Student's t-test (a) or unpaired two-tailed
864 Student's t-test (b, i). *$P < 0.05$, **$P < 0.01$.
865

Extended Data Fig. 6

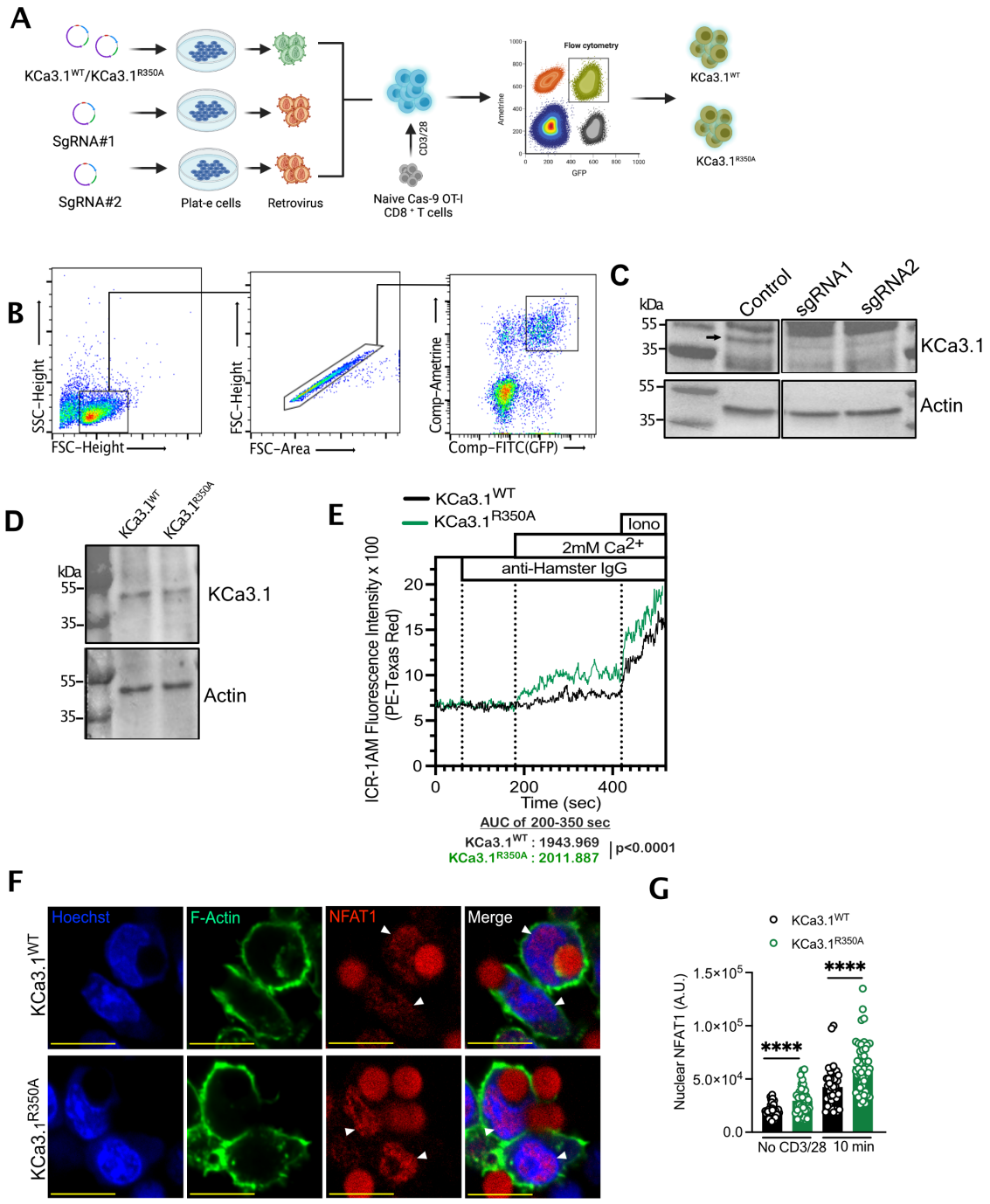

869 **Extended Data Figure 6. KCa3.1 R350 methylation regulates Ca^{2+}- mediated NFAT1**
870 **activation.**
871 **a,** Schematic of experimental design of endogenous KCa3.1 knockdown with expression of
872 $KCa3.1^{WT}$ and $KCa3.1^{R350A}$ in Cas9-OT-I or $P14^{+}$ $CD8^{+}$ T cells. **b,** Sorting strategy for *in vitro*-
873 generated $KCa3.1^{WT}$ and $KCa3.1^{R350A}$ T cells; gate shows the cells that express WT or R350A
874 KCa3.1 with endogenous KCa3.1 knockdown. **c,** Immunoblot showing knockdown of KCa3.1
875 with sgRNA1 and sgRNA2, compared to control. **d,** Immunoblot of KCa3.1 expression in
876 $KCa3.1^{WT}$- and $KCa3.1^{R350A}$-expressing $CD8^{+}$ T cells. **e,** ICR-1 AM analysis of Ca^{2+} flux in
877 $KCa3.1^{WT}$ and $KCa3.1^{R350A}$ T cells activated with anti-CD3 and anti-CD28 by anti-hamster IgG
878 crosslinking in Ca^{2+}-free Ringer solution. Area under the curve is calculated from 200-350 sec. **f,**
879 Un-edited image of Figure. 5b showing the unmasked CD3/38 dynabeads which are masked grey
880 in the main figure to highlight NFAT1 staining. **g,** Nuclear NFAT1quantification of $KCa3.1^{WT}$ and
881 $KCa3.1^{R350A}$, either control (no Dynabeads) or activated with anti-CD3/28 Dynabeads for 10 min
882 (each circle represents one cell, n=45 cells). Data are mean±s.e.m. Two-sample T-test (a) as
883 described in the methods and unpaired two-tailed Student's t-test. ****$P < 0.0001$.
884

Extended Data Fig. 7

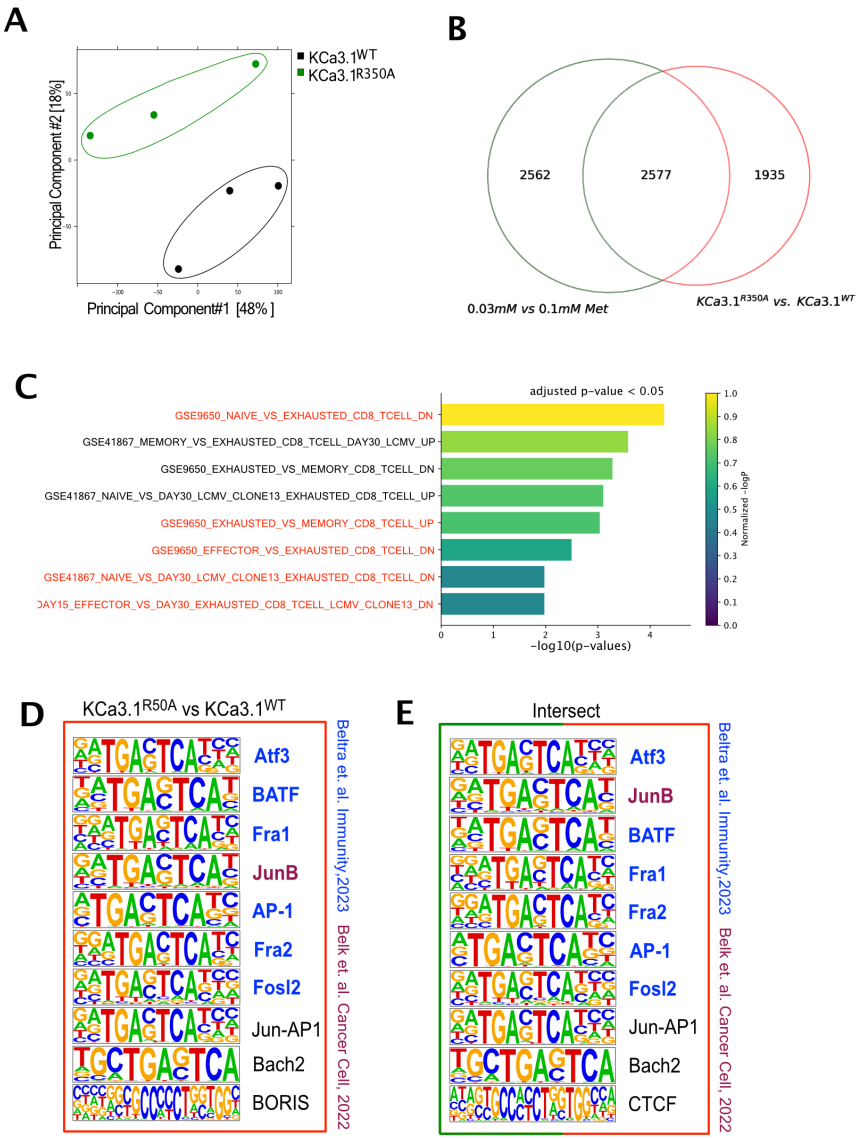

Extended Data Figure 7. Ablation of KCa3.1 R350 methylation shows similar ATAC-Seq signature as of T cells activated in reduced Met.

a, PCA analysis of ATAC-Seq of KCa3.1^{WT}- and KCa3.1^{R350A}- activated with 2.5 ng/ml SIINFEKL for 24 hrs. n=3. **b,** Common differentially accessible regions (DAR) ($p<0.05$, fold change>1.5) between ATAC-Seq of OT-I cells expressing KCa3.1^{WT} or KCa3.1^{R350A}, or OT-I cells initially activated in 0.1 mM or 0.03 mM Met as in (a) and Extended Data Fig. 2b. **c,** Over-representation analysis of the common DAR from (b) showing the top 8 gene sets associated with exhaustion and activation. **d-e,** Top 10 motifs analyzed by HOMER in ATAC-Seq DAR's from

894 24hrs activated OT-I CD8+ T cells expressing KCa3.1^{R350A} vs KCa3.1^{WT} (d), and from the
895 common DAR's from (b) (e). Colour corresponds to the common exhaustion-associated motifs
896 also described in the indicated studies (blue and purple).
897

Extended Data Fig. 8

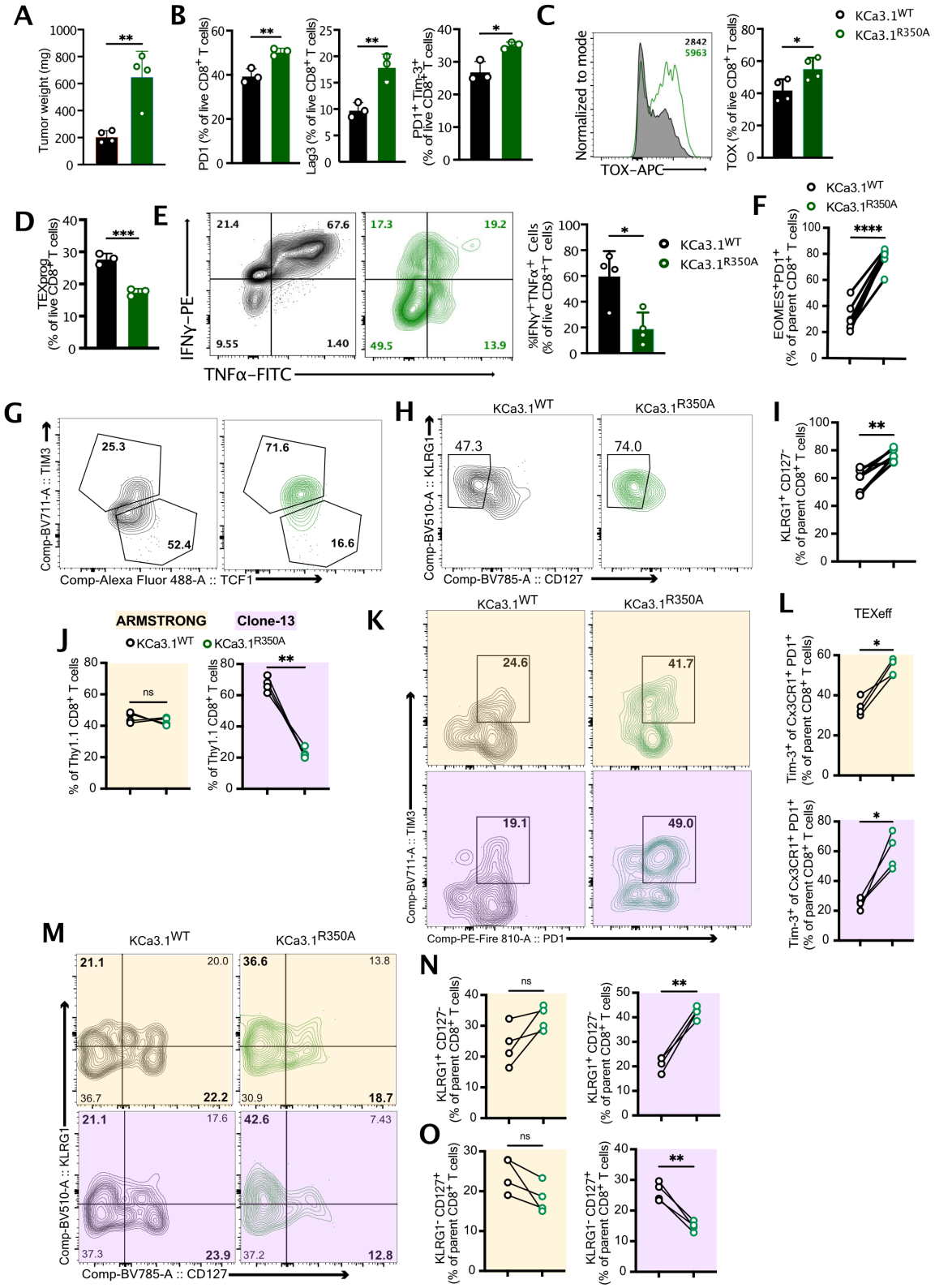

Extended Data Figure 8. Ablation of KCa3.1 R350 methylation promotes T cell exhaustion *in-vivo*.

a, Tumour weight of B16-OVA tumours isolated at D12 post transfer of OT-I T cells expressing KCa3.1^{WT} or KCa3.1^{R350A} (n=4). **b,** Surface expression of PD1^{+}, Lag3^{+} and PD1^{+}Tim-3^{+} in CD8^{+} TIL isolated at D12 post transfer into B16-OVA tumour-bearing mice of OT-I T cells expressing KCa3.1^{WT} or KCa3.1^{R350A} (n=4). **c,** Representative histogram of TOX expression and quantification in CD8^{+} TIL isolated at D12 post transfer of OT-I T cell expressing KCa3.1^{WT} or KCa3.1^{R350A} as (b) (n=4). **d,** Frequency of CD69^{lo}Ly108^{hi} TEXprog in KCa3.1^{WT} and KCa3.1^{R350A} OT-I T cells at D12 post transfer (n=4). **e,** Representative contour plot (left) and quantification of IFNγ^{+}TNFα^{+} (right) in OT-I T cells expressing KCa3.1^{WT} or KCa3.1^{R350A} at D12 post transfer as (b) (n=4). **f-g,** Expression of EOMES^{+}PD1^{+} (f) and representative contour plot of expression of TCF1 and Tim-3 (g) on congenically marked OT-I T cells expressing KCa3.1^{WT} or KCa3.1^{R350A}, mixed and transferred at a ratio of 1:1. TIL were isolated from B16-OVA tumours at D12 post T cell transfer (n=7). **h-i,** Representative contour plot (h) and quantification of KLRG1^{+}CD127^{-} terminal effector cells (i) on congenically marked OT-I T cells expressing KCa3.1^{WT} or KCa3.1^{R350A} as in (f), isolated at D12 post transfer into B16-OVA tumour-bearing mice (n=7). **j,** Frequency of KCa3.1^{WT}- and KCa3.1^{R350A} -expressing P14 T cells in spleens, D9 post infection with either LCMV-Armstrong or LCMV-Clone-13 (n=4). **k,** Representative contour plot of PD1^{+}Tim3^{+} KCa3.1^{WT}- and KCa3.1^{R350A} -expressing P14 T cells in spleens, D9 post infection with either LCMV-Armstrong or LCMV-Clone-13 (n=4). **j,** Frequency of Tim-3^{+}Cx3CR1^{+}PD1^{+} TEXeff KCa3.1^{WT}- and KCa3.1^{R350A} -expressing P14 T cells in spleens, D9 post infection with either LCMV-Armstrong or LCMV-Clone-13 (n=4). **m-o,** Representative contour plot (m) and quantification of KLRG1^{+}CD127^{-} terminal effector cells (n) and KLRG1^{-}CD127^{+} memory precursor cells (o) in spleens of animals injected with congenically marked P14 T cells expressing KCa3.1^{WT} or KCa3.1^{R350A}, mixed 1:1, and infected with either LCMV-Armstrong or LCMV-Clone-13. Analysis on d9 post infection (n=4). Data are mean±s.e.m. Unpaired two-tailed Student's t-test (a-e) and paired two-tailed Student's t-test (f-n). *P < 0.05, **P < 0.01, ***P < 0.001, ****P < 0.0001.

Extended Data Fig. 9

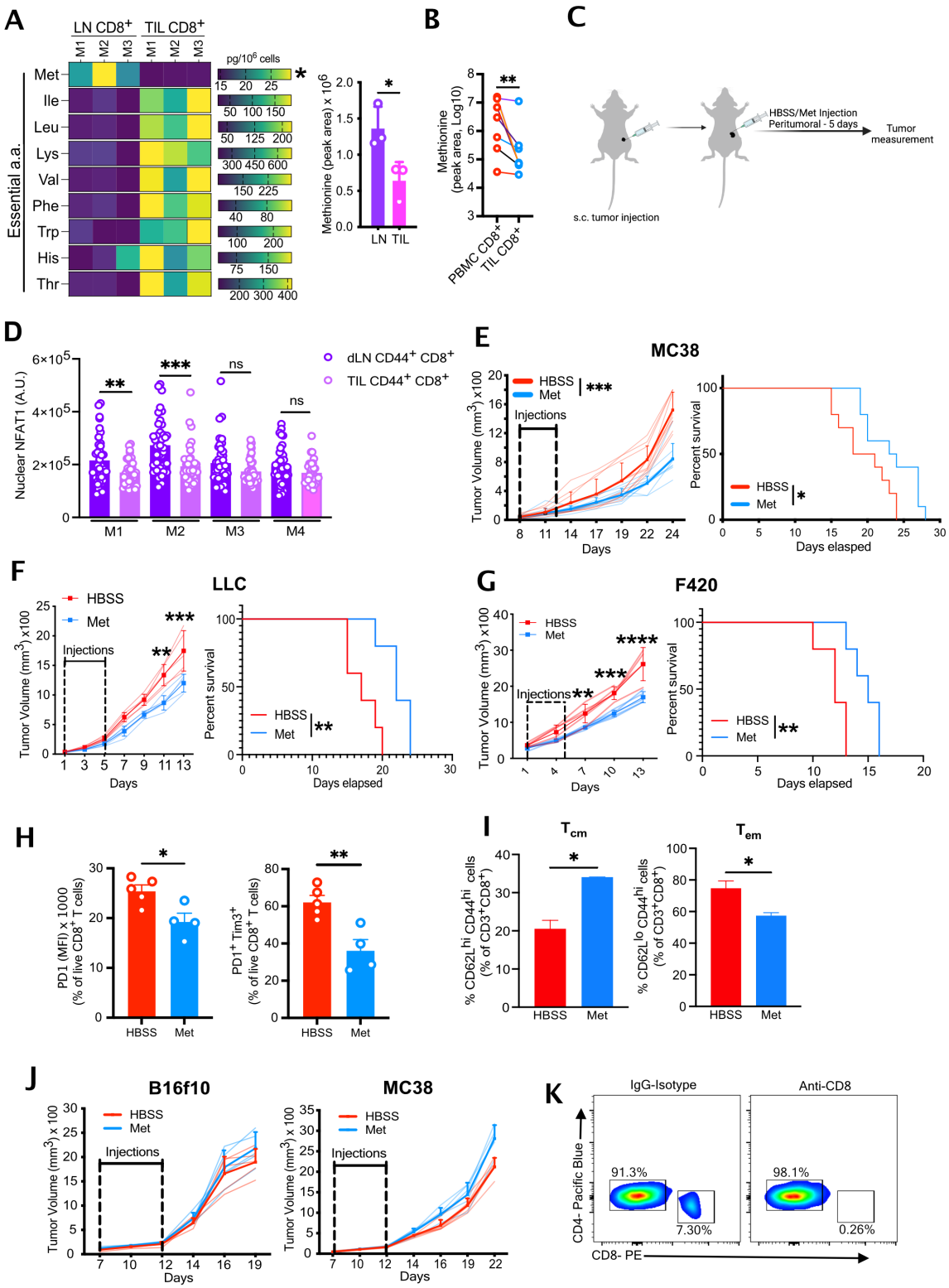

929

930 **Extended Data Figure 9. Acute Met supplementation promotes anti-tumour T cell**
931 **differentiation and tumour control.**
932 **a,** Quantification of essential amino acids (left) and peak area of Met (right) in LN $CD8^+$ T cells
933 and $CD8^+$ TIL, isolated at day 12 post tumour implantation (n=3). **b,** Quantification of intracellular
934 Met in $CD8^+$ PBMC and $CD8^+$ TIL isolated from patient primary colorectal tumours (n= 8). **c,**
935 Schematic of experimental design of acute HBSS/Met peritumoural treatment in sub-cutaneous
936 tumours. **d,** Nuclear NFAT1 quantification of $CD44^+$ $CD8^+$ T cells isolated from B16
937 subcutaneous tumours and dLN, 5 days post daily peri-tumoural supplementation of 50 ml 61μM
938 Met (M=1 mouse, each circle represents one cell, n=40 cells). **e-g,** Tumour growth (left) and
939 survival (right) of WT mice with sub-cutaneous MC38 colorectal tumours (e) (n=10), Lewis-lung
940 carcinoma (LLC) tumours (f) (representative of two experiments of n=5), and F420 osteosarcoma
941 tumours (g) (n=5), treated with either HBSS or 50 ml 61μM Met peri-tumourally daily for 5 days.
942 **h-i,** Expression of PD1, $PD1^+Tim\text{-}3^+$ (h), Tcm ($CD62L^{hi}Cd44^{hi}$) and Tem ($CD62L^{lo}CD44^{hi}$) (i) on
943 $CD8^+$ TIL isolated from B16 tumour-bearing mice 2 days after 5 daily peri-tumoural injection with
944 HBSS or Met (n=5-4). **j,** Tumour growth of B16f10 and MC38 tumours in NSG mice treated peri-
945 tumourally with 50 μl HBSS or 50 μl 61μM Met daily for 5 days (n=5). **k,** Representative flow
946 cytometry plot of blood showing $CD8^+$ T cell depletion in anti-CD8 antibody treated mice
947 compared to IgG-Isotype-treated mice (n=4). Data are mean±s.e.m. Unpaired (a, d, h and i) and
948 paired (b) two-tailed Student's t-test, two-way ANOVA (e-g (left) and j), Mantel-Cox log rank test
949 (e-f (right)). *P < 0.05, **P < 0.01, ***P < 0.001, ****P < 0.0001.
950
951

Extended Data Fig. 10

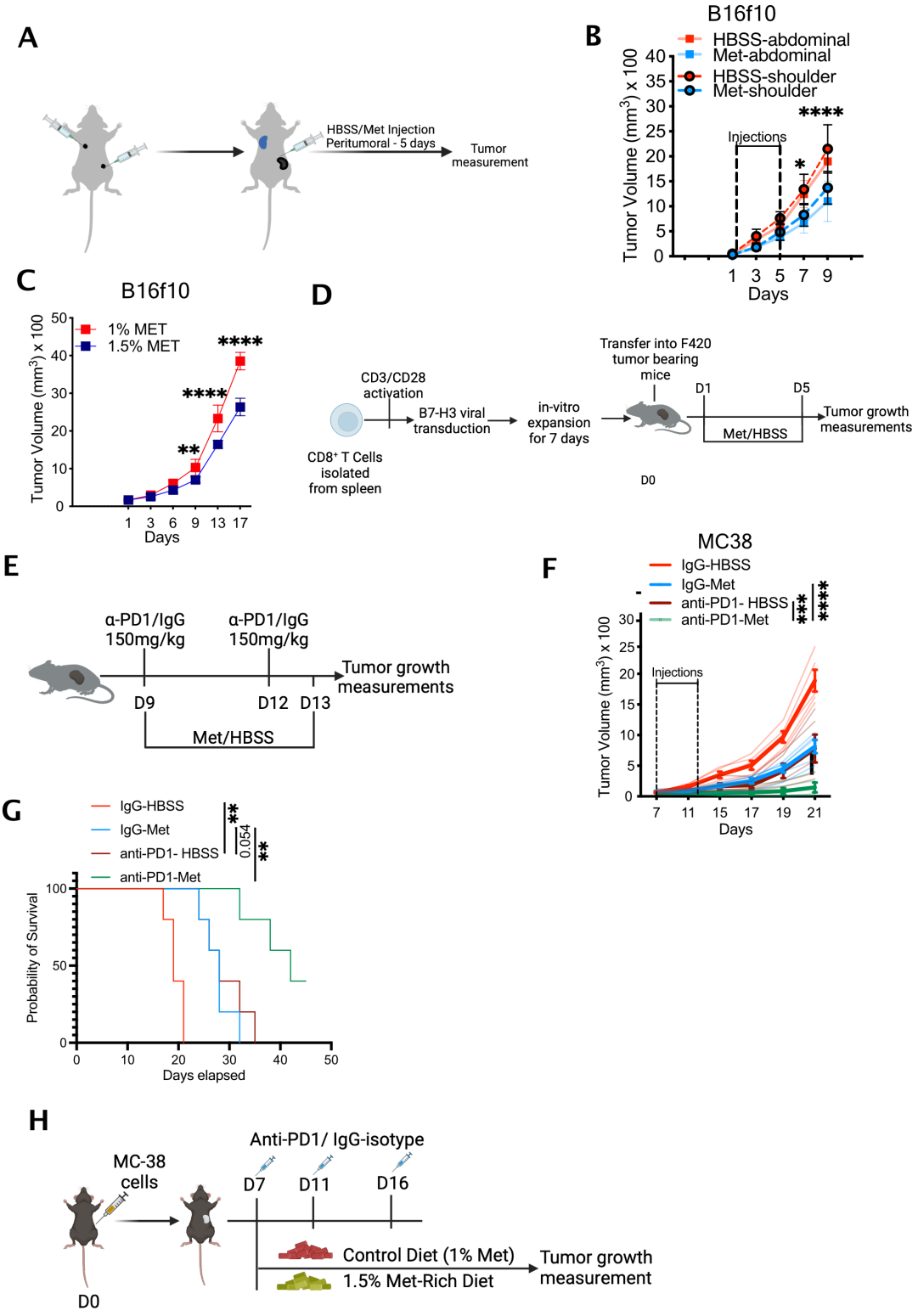

953 **Extended Data Figure 10. Acute Met supplementation promote T cell mediated tumour**
954 **control and enhances tumour immunotherapies.**
955 **a,** Schematic of experimental design of contralateral tumour experiment. **b,** Growth of B16f10
956 tumours implanted on left shoulder (dashed lines) and right flank (solid lines) following peri-
957 tumoural injection of flank tumour with 50 µl HBSS or 61µM Met daily for 5 days (n=5,
958 representative of two experiments). **c,** B16 tumour growth in WT mice fed with either 1 % Met
959 chow or 1.5 % Met chow for 7 days post tumour implantation (n=5). **d,** Schematic of experimental
960 design to assess the effect of HBSS or Met supplementation on CAR-T cell therapy in murine solid
961 tumour model. **e,** Schematic of design to assess tumour growth with anti-PD1 treatment and with
962 either peri-tumoural HBSS or Met supplementation. **f-g,** Tumour growth (f) and survival (g) of
963 MC38 tumour-bearing WT mice, treated either with anti-PD1 or IgG-isotype and supplemented
964 with HBSS or Met peri-tumourally for five days as in (e) (n=5, representative of two experiments).
965 **h,** Schematic of experimental design to assess tumour growth with anti-PD1 treatment on sub-
966 cutaneous tumour-bearing mouse, supplemented with either control diet or Met-rich diet. Data are
967 mean±s.e.m. 2-way ANOVA (b, c, and f), and Mantel-Cox log rank test (g). *P < 0.05, **P < 0.01,
968 ***P < 0.001, ****P < 0.0001.
969

Extended Fig. 11

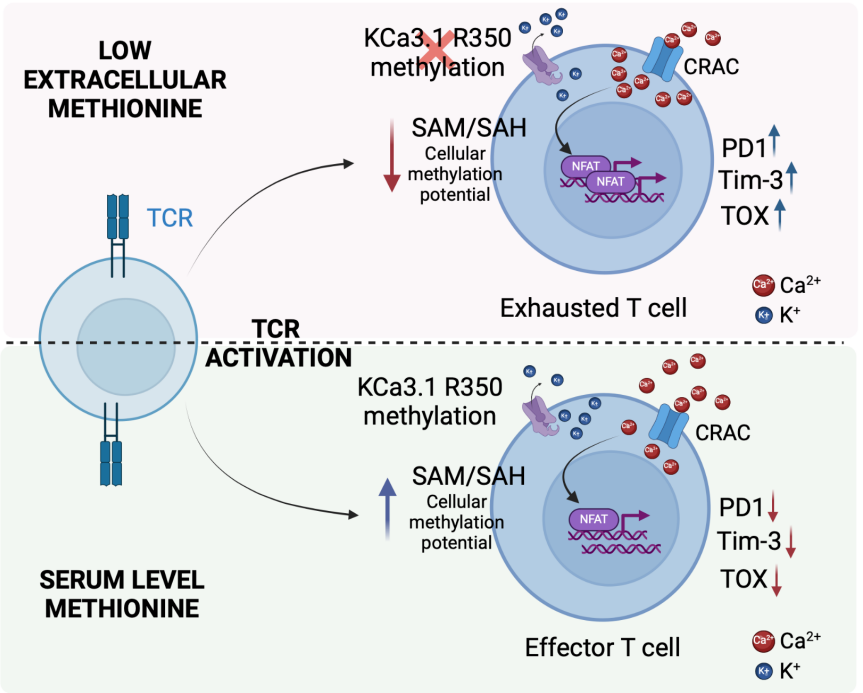

Extended Data Fig. 11: Methionine metabolism regulates TCR-mediated Ca^{2+} flux and T cell fate. Diagram illustrating the impact of methionine metabolism on TCR-dependent methylation of KCa3.1, leading to regulation of Ca^{2+} flux and subsequent activation of NFAT1. Low extracellular Met levels lead to decreased methylation potential, reducing KCa3.1 R350 methylation. This results in increased Ca^{2+} flux and downstream NFAT1 activation and consequent T cell hyperactivation and exhaustion.

986 **Materials and Methods**:

987

988 **Reagents**

989 RPMI 1640 (cat. 11875093, Gibco) and methionine-free RPMI 1640 (cat. A1451701; Gibco)
990 supplemented with 10% dialyzed FCS (Atlanta Biologicals), sodium pyruvate (cat. 11360070,
991 Gibco), NEAA (11140050, Gibco), glutamine (cat. 25030081, Thermo-Fisher), and penicillin-
992 streptomycin cocktail (cat. 15070063, Thermo-Fisher) and stored at 4°C. Methionine (cat. M5308,
993 Sigma-Aldrich) was reconstituted in PBS (0.1 M) and stored at 4°C. SIINFEKL peptide (cat.
994 60193, AnaSpec) peptide was reconstituted in PBS at 0.5 mg/ml and stored at -20°C. TRAM-34
995 (cat. HY-13519, MedChem Express) was reconstituted at 1 M with DMSO. Cyclosporin A (CsA)
996 (cat. 30024, Sigma-Aldrich) was reconstituted to a concentration of 50 mg/ml in DMSO. YM-
997 58483 (cat. 3939, Tocris) was reconstituted at 20 mM stock in DMSO. All reconstituted reagents
998 were stored at -20°C and aliquoted to avoid repeated thawing.

999 **Mice**

1000 All mouse studies were conducted in accordance with protocols approved by the St. Jude
1001 Children's Research Hospital Committee on Care and Use of Animals, and in compliance with all
1002 relevant ethical guidelines. All mice were kept under a 12h-12h light-dark cycle in a specific-
1003 pathogen-free (SPF) facility at the institute's Animal Resource Center. Age-and sex-matched
1004 mice were randomly assigned to the experimental and control groups. Cas9-OT/P14^{+}-I (Cas9
1005 Knock-in with OVA-specific transgenic TCR (OT-I) or LCMV-GP33 specific TCR(p14)),
1006 C57BL/6J (WT), OT-I, and *Rag1*$^{-/-}$ mice were bred in-house. The investigators were not blinded
1007 to the experiments and outcome assessments.

1008 **Cell lines**

1009 B16F10, B16F10-Ova (B16-Ova) melanoma cells were provided by Dr. Hongbo Chi. MC38 and
1010 MC38-Ova colon carcinoma cell lines were provided by Dr. Dario Vignali. The F420 sarcoma cell
1011 line was provided by Dr. Jason T Yustein. HEK293T and Lewis lung carcinoma (LLC) cells were
1012 purchased from the ATCC. Plat-e cells used for retroviral packaging were purchased from Cell
1013 Biolabs (cat. RV-101). All the cell lines used were tested and confirmed to be mycoplasma-
1014 negative but not independently authenticated.

1015 **Murine and Human CD8$^+$ T cell isolation and stimulation**

1016 Murine CD8$^+$ T cells were isolated from the spleen and lymph nodes (LN) by physical disruption
1017 through a 70μ strainer before treatment with erythrocyte-lysis buffer. Cells were subjected to CD8$^+$
1018 T cell enrichment using the EasySep mouse CD8$^+$ T cell isolation kit (cat. 19853, StemCell),
1019 according to the manufacturer's protocol. Isolated T cells were then either activated with
1020 SIINFEKL peptide or mouse CD3/28 Dynabeads (cat. 11456D, Thermo-Fisher) in RPMI medium,
1021 as described above. Human CD8$^+$ T cells were isolated from apheresis rings from the St Jude
1022 Blood Donor Center. Blood obtained from an apheresis ring was mixed at a 1:1 ratio with PBS
1023 containing 2% FBS and carefully layered onto Lymphoprep (cat. 07801, StemCell) solution. The
1024 samples were then centrifuged at 800g for 30 min at room temperature without braking. The
1025 peripheral blood mononuclear cell (PBMC) layer was aspirated and washed twice in PBS with 2%
1026 FBS before enrichment of CD8$^+$ T cells using the Human CD8$^+$ T Cell Isolation Kit (cat. 17953,
1027 StemCell), according to the manufacturer's protocol. CD8$^+$ T cells were activated using human
1028 CD3/28 Dynabeads (cat. 11131D, Thermo Fisher Scientific) in RPMI medium. Apheresis rings
1029 were collected with written consent from the donors for research upon review and approval by the
1030 Institutional Review Board at St Jude Children's Research Hospital.

1031 **Ca^{2+} Flux measurement and analysis**

1032 Isolated T cells were labelled with 3 μM Fluo-8 AM (AAT Bioquest, cat. 21080) or 5 μM ICR-
1033 1AM (Ion Biosciences) with 0.04% pluronic F-127 (Thermo-Fisher, cat. P6867) for 2 hrs in HHBS
1034 at 37 °C and washed twice with Ca^{2+}-free Krebs-Ringer's solution (Thermo Fisher Scientific, cat.
1035 no. J67839-AP). The cells were then resuspended in Ca^{2+}-free Krebs-Ringer's solution and
1036 incubated with anti-CD3ε (4 μg/ml; 2C11, cat. BE0001, Bio-X-Cell) and anti-CD28 (4 μg/ml;
1037 37.51, cat. BE0015, Bio-X-Cell) on ice for 10 min. 0.1 mM Met or 0.03 mM Met was added to the
1038 samples and the baseline was recorded before the addition of hamster-IgG for crosslinking. Ca^{2+}
1039 influx was measured after the addition of 2mM Ca^{2+}, 1uM ionomycin was added as a positive
1040 control for Ca^{2+} flux. All measurements were recorded on either Cytek Aurora (SpectroFlo) or BD-
1041 Fortessa flow cytometer.

1042 To analyze temporal changes in fluorescence intensity, we binned the time variable into 10-second
1043 intervals to calculate the mean log2-transformed fluorescence intensity within each 10-second bin
1044 for each sample. We calculated the AUC across the entire time series, as well as within a focused
1045 time window (x–y seconds) using the trapezoidal rule, which sums the area under each segment
1046 formed by the binned time points. This approach captures cumulative fluorescence intensity over
1047 time, providing a metric for comparing samples. To evaluate statistical significance between
1048 groups, we performed two-sample t-tests on the log2-transformed fluorescence values within the
1049 specified time window (x–y seconds).

1050 **Quantitative PCR**

1051 Isolated T cells were activated with 2.5ng/ml SIINFEKL in 0.1 mM Met or 0.03 mM Met for 30
1052 min after which Met in 0.03 mM was restored to 0.1 mM. T cells were then further cultured for 24
1053 hrs. Cells were washed twice with PBS and RNA was isolated using Direct-zol RNA miniprep Kit
1054 (Zymo research, cat. no. R2050). RNA was quantified and processed for cDNA synthesis using
1055 Reverse Transcriptase (Thermo Fisher Scientific, cat. no. 28025-013). cDNA was then used to
1056 perform quantitative PCR with the specific primers (Table S2) using SYBR green PCR master mix
1057 (Thermo Fisher Scientific, cat. no. 4309155). PCR reaction was run and quantified by QuantStudio
1058 7 flex.

1059 **LCMV infection**

1060 LCMV Armstrong and Clone-13 was obtained from Dr. Shaabani, Scripps Research Institute. The
1061 virus was propagated in BHK21(baby hamster kidney) cells as described[1] and stored at -80 degree
1062 Celsius. For experiments, $2x10^6$ pfu of both Armstrong and Clone-13 was used at $2x10^6$
1063 pfu/animal. The virus was injected intravenously, and the infected animals were maintained under
1064 a 12h-12h light-dark cycle in a SPF, Biosafety Level-2 facility in the institute's Animal Resource
1065 Center.

1066 **Cloning and virus production**

1067 *Kcnn4* gRNA's were designed using the Broad Institute platform
1068 (https://portals.broadinstitute.org/gpp/public/analysis-tools/sgrna-design) and cloned into the

1069 ametrine-expressing retroviral vector LMPd-gRNA-mPGK-Ametrine
1070 (sgRNA1:CACCGGGCAGGCTGTCAATGCCACG,
1071 AAACCGTGGCATTGACAGCCTGCCC; sgRNA2:CACCGTGTGGGGCAAGATTGTCTGC,
1072 AAACGCAGACAATCTTGCCCCACAC). KCa3.1^{WT} and KCa3.1^{R350A} cDNA were synthesized
1073 by Genscript; the latter contained an alanine substitution at R350. Both KCa3.1^{WT} and KCa3.1^{R350A}
1074 had substitutions at the PAM recognition sites of the gRNAs (Table S3). Each cDNA was
1075 subcloned into the pMIGII. Plat-e cells were co-transfected with the cloned vectors and pCL-eco
1076 (cat. 12371, Addgene) in Opti-MEM (cat. 31985070, Thermo-Fisher) with Trans-IT-293
1077 transfection reagent (cat. MIR 2705, Mirus Bio) and cultured at 37°C for 12-15 hrs prior to
1078 changing the medium and culturing for an additional 24 hrs at 37°C, followed by 24 hrs at 32°C,
1079 5% CO_2. The viral supernatant was harvested and spun at 1800rpm at RT to remove the cell debris.
1080 Viral supernatant was either used immediately or stored at -80°C till further use.

1081

1082 **Viral transduction**

1083 Naive Cas9-OT-I CD8$^+$ cells were isolated from the spleen and peripheral LNs of Cas9-OT-I mice
1084 using a Magnisort naïve CD8$^+$ T cell isolation kit according to the manufacturer's instructions (cat.
1085 8804-6825-74, Thermo-Fisher). Purified CD8$^+$ T cells were activated *in vitro* for 20 h with plate-
1086 bound anti-CD3ε (5 μg/ml; 2C11, cat. BE0001, Bio-X-Cell) and anti-CD28 (5 μg/ml; 37.51, cat.
1087 BE0015, Bio-X-Cell) antibodies. Viral transduction was performed by spinfection at 900 *g* at
1088 25 °C for 3 h with 10 μg/ml polybrene (Sigma-Aldrich), followed by resting for 3 h at 37 °C in
1089 5% CO_2. Cells were washed and cultured in medium supplemented with mouse rIL-2 (20 U/ml;
1090 cat. 212-12, Peprotech) for 4 days. GFP-Ametrine double-positive cells were sorted using the
1091 Reflection cell sorter (iCyt) or the MoFlo XDP cell sorter and rested for 24 hrs in medium
1092 containing rIL-2 (10U/ml, cat. 212-12 Peprotech) before activation or adoptive transfer into the
1093 animals.

1094 **Flow cytometry**

1095 Antibodies from BioLegend included Pacific Blue anti-mouse Ly108 (330-AJ, 134608), BV510
1096 anti-mouse KLRG1 (2F1, 138421), BV570 anti-mouse CD62L (MEL-14, 104433), BV711 anti-
1097 mouse Tim-3 (RMT3-23, 119727), BV785 anti-mouse CD127 (A7R34, 135037), PE-Cy5 anti-

1098 mouse Granzyme-B (QA16A02, 372226), PE-Fire 700, anti-mouse CD4 (GK1.5, 100484),
1099 APC/Cy7 anti-mouse TNFα (MP6-XT22, 506344), PE-Cy7 anti-mouse KLRG1 (2F1/KLRG1,
1100 138416), PerCP-Cy 5.5 anti-mouse CD62L (MEL-14, 104432), BV605 anti-mouse CD127
1101 (A7R34, 135025), Pacific blue anti-mouse CD69 (H1.2F3, 104524), Pacific blue anti-mouse
1102 CD45.1 (110722), APC anti-mouse PD1 (RL388, 109111), BV711 anti-mouse PD1 (29F.1A12,
1103 135231), PE anti-mouse IFNγ (XMG1.2, 505808), FITC anti-mouse TNFα (MP6-XT22, 506304),
1104 Pacific Blue anti-human CD45 (HI30, 982306), APC/Cy7 anti-human CD8 (RPA-T8, 344713).
1105 BUV563 anti-mouse LAG3 (C9B7W, 741350), BUV615 anti-mouse CD69 (H1.2F3, 751593),
1106 BUV805 anti-mouse CXCR3 (173, 748700), BV421 anti-mouse EOMES (X4-83, 567166),
1107 BV480 anti-mouse CD45.1 (A20, 746666), Alexa-Fluor 488 anti-mouse TCF1 (S33-966, 567018),
1108 Alexa-Fluor 647 TOX (NAN448B, 568356), BUV 496 anti-mouse Ly-108 (13G3, 750046),
1109 APC/Cy7 anti-mouse CD44 (IM7, 560568) and BUV805 anti-mouse CD8α (53-6.7, 612898) were
1110 acquired from BD Biosciences. BUV395 anti-mouse CD44 (IM7, 363-0441-82), PerCP-Cy 5.5
1111 anti-mouse IL-2 (JES6-5H4, 45-7021-82), PerCP-eF710 anti-mouse CD27 (O323, 46-0279-42),
1112 and PE-Cy7 anti-mouse Tim-3 (RMT3-23, 12-5870-82, eBioscience) were obtained from Thermo
1113 Fisher. APC anti-human/mouse Tox (REA473, 130-118-335) was obtained from Miltenyi Biotech.
1114 For surface markers, the cells were stained for 30 min on ice in PBS containing 2% FCS and 0.1%
1115 sodium azide (cat. S2002, Sigma-Aldrich). To examine intracellular cytokine production, the
1116 isolated cells were stimulated with a cell activation cocktail (cat. 5476, TOCRIS) in the presence
1117 of monensin (cat. 554724, BD Biosciences) for 4 hr, and stained for intracellular cytokines and
1118 transcription factors using a fixation/permeabilization kit (cat. 00-5523-00, Ebiosciences). Fixable
1119 viability dye (Thermo Fisher) was used to exclude dead cells. Samples were acquired on a Cytek
1120 Aurora (SpectroFlo) or BD LSRII (FACSDiva) flow cytometer and analysed using FlowJo
1121 software.

1122 ***In vivo* tumor analysis**

1123 For all tumor experiments, $0.5x10^6$ tumor cells were injected subcutaneously into the right flank
1124 of naive mice (aged 6–10 weeks). Met was diluted in HBSS to a concentration of 61 μM per 50μl.
1125 Mice were injected peri-tumorally for 5 days with either 50 μl Met or HBSS. Tumours were
1126 measured with calipers every 2 days and tumor volumes were calculated using the formula:
1127 $(\text{width}^2 \times \text{length})/2$. For adoptive transfer experiments, T cells (1×10^6) were transferred i.v. 7 -9

1128 days after tumor injection. For contralateral tumor model, 0.5×10^6 B16 tumor cells were injected
1129 subcutaneously into the right flank and left shoulder of the same mouse. Met or HBSS was injected
1130 peri-tumorally to the right flank tumor (abdominal). For check-point blockade experiment,
1131 0.5×10^6 MC38 tumor cells were injected subcutaneously into the right flank of WT mice. The
1132 mice were given either anti-PD1 antibody (RMP1-14, Bio X Cell) or rat IgG2a (2A3, Bio X Cell),
1133 intraperitoneally twice at a dose of 150 mg/kg in 100 µl PBS at day 9 and 12. Met or HBSS was
1134 given peri-tumorally for 5 days from day 9 to 13. For the CAR-T tumor model, 0.5×10^6 F420
1135 tumor cells (derived from singly floxed *p53+/F-Col2.3* transgenic mice[2]); were injected
1136 subcutaneously into the right flank of *Rag1*$^{-/-}$ mice. 5×10^6 B7-H3 CAR-T cells (see below) were
1137 transferred i.v. 8-10 days post implantation. Tumour size was measured every 2-4 days.

1138 **Generation of mouse CAR-T cells**

1139 Generation of mouse B7-H3-CAR constructs and CAR-T generation have been previously
1140 described[3]. Briefly, HEK293T cells were transiently transfected with the CAR-encoding plasmid,
1141 the Peg-Pam plasmid encoding MoMLV gag-pol, and a plasmid encoding the VSVG envelope.
1142 Viral supernatants were collected at 48 h and filtered with a 0.45m filter. The virus was then used
1143 to transduce the GPE86 producer cell line. B7-H3-CAR-expressing GPE86 cells were stained with
1144 Alexa Fluor-647 anti-human IgG, F(ab′)2 fragment antibody (cat. 109-606-006, Jackson
1145 ImmunoResearch) and sorted using the BD FACSAria III system.

1146 Naive CD8$^+$T cells from 6–8 weeks old CD45.1$^+$ mice were activated with plate-bound anti-CD3ε
1147 (1 µg/ml, 145-2C11, cat. BE0001, BioXcell), anti-CD28 (2 µg/ml, 37.51, cat. BE0015, BioXcell)
1148 and 50 U ml^{-1} rhIL-2 (cat. 200-02, Peprotech). On day 2 post activation, activated CD8$^+$ T cells
1149 were transduced with retrovirus expressing B7-H3-CAR on retronectin-coated (cat. T100B,
1150 Takara) non-tissue-culture-treated plate in complete RPMI medium supplemented with
1151 50 U/ml rhIL-2. At 48 h after transduction, CAR-T cells were collected and expanded in the
1152 presence of 50 U/ml rhIL-2 for another 3 days before adoptive transfer into tumor-bearing mice.

1153 **Tumour-infiltrating lymphocyte isolation**

1154 B16 tumors were harvested at the indicated time points and digested using a digestion cocktail
1155 (0.1% Collagenase IV and 0.01% DNaseI) for 5 min at 37 °C. Digested tumors were passed

1156 through a 70m strainer and resuspended in PBS plus 2% dialyzed FCS and processed for analysis
1157 and/or sorting by flow cytometry, as described above.

1158 Patient samples were collected following surgery and were immediately processed. Tumour
1159 samples were dissected into small pieces and digested at 37°C with digestion cocktail for 40 min.
1160 Digested tumor samples were physically disrupted and passed through 70μ filter. Samples were
1161 washed with PBS-2% dialyzed FCS twice and stained for CD45, CD3ε and CD8 and sorted for
1162 $CD8^+$ T cells by flow cytometry. Purified T cells were washed once with 1% saline and flash
1163 frozen in liquid nitrogen. Samples were collected upon informed consent and procedures approved
1164 by the IRB of St. Jude Children's Research Hospital.

1165 **Immunofluorescence staining and imaging.**

1166 $CD8^+$ T cells were immobilized in 8-well poly L-lysine-coated IBIDI chambers and stimulated by
1167 the addition of CD3/28 Dynabeads (cat. 11452D, Thermo Fisher) for 30 min, followed by 10 min
1168 of fixation with 4% paraformaldehyde (PFA) (cat. 15710, Electron Microscopy Science) at 37°C.
1169 The cells were washed once with TBS (50 mM Tris, 100 mM NaCl, pH 8.0) and permeabilized
1170 with permeabilization buffer (50mM Tris, 100 mM NaCl, pH 8.0, 0.3% (v/v) Triton X-100) for
1171 20 min at room temperature. Cells were washed again with TBS before blocking with
1172 TBS containing 2% BSA (Cat. 001-000-182, Jackson ImmunoResearch) for 60 min at room
1173 temperature. The cells were stained overnight at 4 °C with the following primary antibodies: anti-
1174 NFAT1 (1:200, cat. 4389, Cell Signaling Technology), anti-NFAT2 (1:200, cat. D15F1, Cell
1175 Signaling Technology) and anti-mono and dimethyl arginine (1:500, cat. ab412, Abcam). The
1176 samples were washed twice with TBS and incubated for 1 h at room temperature with the following
1177 antibodies: anti-rabbit Alexa Fluor plus 595 (1:1,000, cat. A-11012, Thermo Fisher), anti-mouse
1178 CD8-APC (1:500; cat. 100712, BioLegend), Alexa Fluor 488 Phalloidin (1:1000, cat. A12379,
1179 Thermo Fisher) and Hoechst 33258 (1:1000, cat. H3569, Thermo-Fisher). Samples were then
1180 imaged by Marianas spinning-disc confocal microscopy (Intelligent Imaging Innovations), using
1181 the Prime95B sCMOS camera, and the 405, 488, 561 and 640 nm laser lines. Sum fluorescence
1182 intensities were analyzed using Slide Book 6 (Intelligent Imaging Innovations).

1183 **Immunoblotting**

1184 T cells were washed once with ice-cold PBS and immediately lysed with 4x laemmli buffer (Bio-
1185 Rad, cat. 1610747). Cell lysates were separated by SDS-PAGE and blotted with anti-Kcnn4
1186 antibody (cat. PA5-33875, Thermo Fisher) and HRP-conjugated anti-Actin (cat. sc4777-HRP,
1187 Santa Cruz Biotechnology). Images were developed using Clarity Western ECL substrate (cat.
1188 1705061, Bio-Rad) and acquired on Bio-Rad Chemi-Doc.
1189
1190 **Amino acid measurement**
1191 Subcutaneous tumors were isolated and processed as described above. Sorted T cells were washed
1192 once with ice-cold saline, flash-frozen with liquid nitrogen, and stored at –80ºC before analysis.
1193 Cell pellets were extracted using 750 µl of methanol/acetonitrile/water (5:3:2, v/v/v) and the
1194 supernatant was dried by lyophilization. Aliquots of 20-50 µl from plasma and TIF were extracted
1195 with at least a 15-fold excess volume of the methanol/acetonitrile/water solution, and the
1196 supernatant was then collected and dried by lyophilization. Dried extracts containing the
1197 hydrophilic metabolites were dissolved in 30 µl of water/acetonitrile (8:2, v/v), and 10 µl was used
1198 to derivatize amino acids as described [4] with some modifications. The samples were placed in glass
1199 autosampler vials, and 35 µl of sodium borate buffer (100 mM, pH 9.0) was added and mixed by
1200 pipetting. 10 µl of the 6-aminoquinolyl-N-hydroxysuccinimidyl carbamate (AQC, 10 mM in
1201 acetonitrile)-derivatizing reagent (Cayman Chemical) was added, the vial was sealed, mixed by
1202 vortexing, and then incubated at 55°C for 15 min. The vial was cooled to room temperature and
1203 then 1 µL was analyzed by liquid chromatography with tandem mass spectrometry (LC-MS/MS).
1204 An ACQUITY Premier UPLC System (Waters Corp) was used for the LC separations, using a
1205 non-linear gradient condition as follows: 0-0.4 min 3% B; 0.4-8 min 3 to 96% B (using Curve #8
1206 of the inlet condition in MassLynx™); 8-12 min 96% B; 12-12.5 min 96 to 3% B; 12.5-14 min 3%
1207 B. Mobile phase A was water supplemented with 0.15% acetic acid, and mobile phase B was
1208 acetonitrile with 0.15% acetic acid. The column used was an Accucore C30 (50 × 2.1 mm, 2.6 µm)
1209 (Thermo Fisher Scientific) operated at 50°C. The flow rate was 300 µl/min and the injection
1210 volume used was 1 µl. All LC/MS solvents and reagents were the highest purity available (water,
1211 acetonitrile, acetic acid, boric acid, sodium hydroxide) and were purchased from Thermo Fisher
1212 Scientific. A Xevo TQ-XS Triple Quadrupole Mass Spectrometry (TQ-XS) (Waters Corp)
1213 equipped with a multi-mode ESI/APCI/ESCi ion source was employed as detector. The TQ-XS
1214 was operated in positive ion mode using a multiple reaction monitoring mass spec method (MRM).

1215 The MRM conditions were set to a minimum of 15 points per peak with an automatic dwell time.
1216 The operating conditions of the source were: Capillary Voltage 3.8 kV, Cone Voltage 40 V,
1217 Desolvation Temp 550°C, Desolvation Gas Flow 1000 L/h, Cone Gas Flow 150 L/h, Nebuliser
1218 7.0 Bar, Source Temp 150°C. Authentic amino acid standards were purchased from Sigma-Aldrich
1219 and used to establish MRM conditions and calibration curves. The monitored parent/daughter ions,
1220 fragmentation collision energy (CE), and retention time window for each amino acid are listed in
1221 Supplementary Table 4. The acquired MRM data was processed using the software application
1222 Skyline 21.2 (MacCoss Lab Software).
1223
1224 ***In-silico* model building of KCa3.1(SK4)-Calmodulin complex and simulation.**
1225 To study the impact of SK4s arginine dimethylation on the binding of calmodulin, we simulated
1226 the SK4 channel:Calmodulin complex in a membrane layer via all-atom molecular dynamics
1227 (MD), which is considered a computational microscope[5]. The Cryo-EM structure of the human
1228 SK4 channel:Calmodulin complex state (PDB:6CNN[6]) was used as the starting structure. Thisa
1229 tetramer compleconsistsng of four SK4 monomers, four calmodulins (CAMs), three calcium ions
1230 bound to each calmodulin (CAM) (total 1,2) and four K^+ ions bound to the channel selectivity
1231 filter.
1232 Initially, protein was prepared was using the molecular operating environment (MOE) software.
1233 The missing residues in the cryo-EM structure were modeled based on the human AlphaFold
1234 structure (AF-015554-F1). Protonate3D module in MOE was used to assign appropriate
1235 protonation states at pH 7.4 and then energy minimized. Further, simulation system was prepared
1236 using CHARMM-GUI web server[7-9]. Protein was placed in the POPE membrane bilayer and
1237 protein orientation was obtained using the PPM web server[10]. The protein-membrane bilayer
1238 complex was immersed in the TIP3P[11] water box of size ≈150 X 150 X 230 $Å^3$ with an edge
1239 distance of 40 Å on all sides. KCl salt was added to balance the charges and maintain a
1240 physiological salt concentration of 0.15M. Overall, each wildtype simulation system contains four
1241 SK4 monomers, four CAMs, 12 Ca^{2+} ions, ≈355 K^+ ions, ≈367 Cl^- ions, ≈618 POPE lipids, and
1242 ≈128,144 TIP3P waters. The total numbers of atoms in this system are ≈498,944. Two more
1243 systems were generated via a protocol similar to that explained above, except that in one system,
1244 R352 of the SK4 monomer was symmetrically dimethylated and in the second system, R352 was
1245 asymmetrically dimethylated. Dimethylation was introduced using the CHARMM-GUI web

server. Note that arginine's at position 352 in all four SK4 monomers were dimethylated in both systems.

Further, all three systems were simulated using AMBER20/22 MD software[12]. The MD simulation was performed in three steps. In step-1, energy minimization was carried out to remove potential steric clashes in two stages. In stage 1, each system was energy-minimized for 5000 steps, while positional restraints were applied to the protein and membrane: the first 2500 steps with the steepest-descent algorithm and the remaining 2500 steps using the conjugate gradient algorithm[13]. In stage 2, the second round of minimization was carried out with all restraints removed in 50,000 steps. The steepest-descent algorithm[14] was used for the first 25,000 steps, while the conjugate gradient algorithm was used for the remaining 25,000 steps. In step-2, equilibration was carried in six stages: (1) equilibrated for 125 ps with a time step of 1fs while applying positional restraints on protein (K=10 kcal/mol.Å^2) and membrane (K=2.5 kcal/mol.Å^2), (2) equilibrated for 125 ps with a time step of 1fs w while applying positional restraints on the protein (K=5.0 kcal/mol.Å^2) and membrane (K=2.5 kcal/mol.Å^2), (3) equilibrated for 125 ps with a time step of 1fs while applying positional restraints on the protein (K=2.5 kcal/mol.Å^2) and membrane (K=1.0 kcal/mol.Å^2), (4) equilibrated for 500 ps with a time step of 2 fs while applying positional restraints on the protein (K=1.0 kcal/mol.Å^2) and membrane (K=0.5 kcal/mol.Å^2), (5) equilibrated for 500 ps with a time step of 2 fs while applying positional restraints on the protein (K=0.5 kcal/mol.Å^2) and membrane (K=0.1 kcal/mol.Å^2) and (6) equilibrated for 500 ps with a time step of 2 fs while applying weak positional restraints on the protein (K=0.5 kcal/mol.Å^2) and restraints on the rest of the system were completely removed. The first two equilibration simulations were performed under NVT conditions, whereas the last four equilibration simulations were performed under NPT conditions. In step-3, production simulations were carried out under periodic boundary conditions using the NPT ensemble, during which the temperature (310 K) and pressure (1 atm) were kept constant. Three replicates of each system were simulated, and each replicate was simulated for ≈1 µs. Langevin integrator and Monte Carlo barostat were used[15,16] to conduct NPT simulations, whereas the SHAKE algorithm was used to restrain bonds with hydrogens[17]. Particle-mesh Ewald (PME) method was used to treat long-ranged electrostatic interactions[18] and the nonbonded cutoff was 12Å (force switching = 10Å). CHARM36 all-atom additive force field[19,20] was used to treat the entire system. Overall, nine MD simulations were conducted across three systems, with each system comprising three replicates that each ran for approximately 1µs. Consequently, the total

1277 MD simulation data accumulated for analysis amounts to approx. 9 µs, derived from the sum of
1278 simulation times for all systems and replicates (3 systems X 3 replicates X ≈1µs/per replicate =
1279 ≈9µs). Two frames per nanosecond were used for the data analysis. Visual molecular dynamics
1280 (VMD)[21] was used for visualization and graphic generation, whereas Tcl was used for data
1281 analysis. Gnuplot was used to generate the time series plots.
1282

1283 **ATAC-seq**

1284 OT-I $CD8^+$ T cells were activated with 2.5ng/ml SIINFEKL in either 0.1 mM Met or 0.03 mM
1285 Met with restoration of Met to 0.1 mM in 0.03 mM condition post 30 min of activation and
1286 incubated for 24 hrs. $KCa3.1^{WT}$ and $KCa3.1^{R350A}$ cells were activated by 2.5ng/ml SIINFEKL for
1287 24 hrs. Cells were processed for ATAC-Seq after 24 hrs of activation. Briefly, 50,000 cells were
1288 washed with 1 ml cold PBS by centrifugation at 500 g for 5 min at 4°C. Cells were then
1289 resuspended in 50 ml cold cell lysis buffer (10 mM Tris pH 7.4, 10 mM NaCl, 3 mM $MgCl_2$, and
1290 0.1% NP-40). Isolated nuclei were pelleted at 1,000 × g for 10 min at 4°C, resuspended in 50 µl
1291 transposition reaction mixture (25 µl TD buffer, 2.5 µl TDE1, 22.5 µl ddH_2O) (20034197,
1292 Illumina), and incubated at 42°C for 45 min. DNA was purified using a MiniElute PCR purification
1293 kit (cat. 28004, Qiagen). Samples were then processed for library barcoding and amplification with
1294 Q5 High-Fidelity 2× Master Mix (cat. M0492S, NEB). Prepared libraries were sent for sequencing
1295 after quantification using Qubit and size distribution as determined using an Agilent 4200
1296 TapeStation.

1297 **Analysis of ATAC-seq data**

1298 Paired-end sequencing reads were trimmed using Trim Galore (version 0.5.0)
1299 (https://github.com/FelixKrueger/TrimGalore) with default parameters. Reads were aligned to the
1300 reference mouse mm10 assembly using Bowtie 2 (version 2.3.5.1)[22] with settings --end-to-end --
1301 very-sensitive -X 2000. The resulting alignments, recorded in a BAM file, were sorted, indexed, and
1302 marked for duplicates with Picard MarkDuplicates function (version 2.19.0). Afterward, the BAM
1303 file was filtered with SAMtools (version 1.9)[23], BamTools (version 2.5.1)[24] and scripts of nf-
1304 core/chipseq[25] to discard reads, mates that were unmapped, PCR/optical duplicates, not primary
1305 alignments, mapped to multiple locations, or mapped to ENCODE blacklisted regions[26]; only reads

1306 mapped in proper pair were kept (-F 1804 -f 2 -q 30). The alignments were shifted by deepTools
1307 alignmentSieve[27] with --ATACshift and default parameters. Nucleosome-free reads (fragment
1308 length < 109 bp) were separated from the BAM files with SAMtools (version 1.9). MACS (version
1309 2.1.2)[28] was used to call peaks from the BAM files with narrowPeak setting, --extsize 200, and
1310 recommended mappable genome size (default value for other parameters). Chromatin accessibility
1311 signal was normalized by scaling to 1 million mapped reads using BEDTools (version 2.27.1)[29]
1312 and bedGraphToBigWig (version 377)[30] and visualized as heatmaps using deepTools plotHeatmap
1313 (version 3.2.1)[27].

1314 Differentially accessibility analysis was performed using DiffBind[31] (v.3.4.7) (summit = 50,
1315 normalized by trimmed mean of M values[32] (TMM) approach, library size estimated by reads
1316 mapped to "background" regions, the genomic regions (binned into 15000 bp) overlapped with
1317 peaks). Peaks were annotated to the nearest genes with annotatePeak function in R package
1318 ChIPseeker[33] (v.1.30.3) at the gene level using the default parameters. Genes were ranked by fold
1319 change (log2 transformed) of associated peaks located within +/- 1.5 kb of transcription start sites
1320 (if a gene was associated with multiple peaks, the mean was used). Gene Set Enrichment Analysis[34]
1321 (GSEA) was then performed against MSigDB collections with R package clusterProfiler[35]
1322 (v.4.2.2). The common differentially accessible regions (DAR) between ATAC-Seq of KCa3.1WT
1323 and KCa3.1R350A and T cells activated in 0.1 mM or 0.03 mM Met were obtained by the
1324 overlapping of the DARs (at least 1 bp). Enrichment analysis was performed using the over-
1325 representation approach against MSigDB using the R package clusterProfiler.

1326

1327 **CUT&RUN**

1328 CUT&RUN experiments were performed as previously described[36] with slight modifications.
1329 Purified OT-I $CD8^+$ T cells were activated with 2.5ng/ml SIINFEKL in 0.1 mM and 0.03 mM Met
1330 for 30 min. Met was restored to 0.1 mM post 30 min and cultured for 24 hrs. Cells were washed
1331 with cold PBS and dead cells were removed using Easysep dead cell removal kit (cat. 17899,
1332 StemCell). Cells (2×10^5) were washed twice with wash buffer (20 mM HEPES (H3375, Sigma-
1333 Aldrich], 150 mM NaCl (cat. AM9760G, Invitrogen), 0.5 mM spermidine (cat. S0266, Sigma-
1334 Aldrich), and protease inhibitor cocktail (cat. 5056489001, Sigma-Aldrich)), resuspended and
1335 bound to concanavalin-A coated magnetic beads (cat. BP531, Bang Laboratories). The

1336 resuspension buffer was removed using a magnetic stand and beads were resuspended in 100 µl
1337 antibody buffer (20 mM HEPES, 150 mM NaCl, 0.5 mM spermidine, 0.01% digitonin (cat.
1338 300410, Millipore), 2 mM EDTA (cat. AM9260G, Invitrogen), and protease inhibitor cocktail).
1339 Primary antibodies (1:100) were added to the samples and incubated overnight at 4 °C. Next,
1340 samples were washed twice with cold Dig-wash buffer (20 mM HEPES, 150 mM NaCl, 0.5 mM
1341 spermidine, 0.01% digitonin, and protease inhibitor) and pAG-MNase (cat. 123461, Addgene) was
1342 added and rotated at 4 °C for 1 h. Samples were washed twice and resuspended in 50 µl Dig-wash
1343 buffer and $CaCl_2$ (2 µl of 100 mM, cat. 2115, Sigma-Aldrich) was added followed by brief
1344 vortexing and incubation on ice for 30 min. Next, 50 µl of 2× STOP buffer (340 mM NaCl, 20 mM
1345 EDTA, 4 mM EGTA (cat. E3889, Sigma-Aldrich) and 100 µg/ml RNase A (cat. EN0531, Thermo
1346 Fisher), and 50 µg/ml GlycoBlue (cat. AM9515, Invitrogen)) was added and mixed by gentle
1347 vortexing and incubated for 30 min at 37 °C to release CUT&RUN fragments. Fragmented DNA
1348 was purified using the NEB Monarch PCR&DNA Cleanup Kit (cat. T1030S, New England
1349 Biolabs). DNA libraries were prepared using the NEBNext Ultra II DNA Library Prep Kit (cat.
1350 E7645S, New England Biolabs) and purified with AMPure SPRI beads (cat. B23318, Beckman-
1351 Coulter). Prepared libraries were quantified using Qubit and size distribution was determined with
1352 a Agilent 4200 TapeStation analysis before paired-end sequencing.

1353 **CUT&RUN data processing**

1354 Paired-end sequencing reads were trimmed using Trim Galore (v.0.5.0)
1355 (https://github.com/FelixKrueger/TrimGalore) with default parameters. The reads were then
1356 aligned to the reference mouse mm10 assembly using Bowtie 2 (v.2.3.5.1)[22] with settings --end-
1357 to-end --very-sensitive --no-mixed --no-discordant -q --phred33 -I 10 -X 700. The resulting
1358 alignments, recorded in the BAM file, were sorted, indexed, and marked for duplicates using the
1359 Picard MarkDuplicates function (v.2.19.0) (Picard toolkit. *Broad Institute GitHub Repository,*
1360 2019). Next, the BAM file was filtered with SAMtools (v.1.9)[23], BamTools (v.2.5.1)[24] and scripts
1361 of nf-core/chipseq[25] to discard reads, including mates that were unmapped, PCR/optical duplicates,
1362 non-primary alignments, reads that mapped to multiple locations or to ENCODE-blacklisted
1363 regions[26], or with more than 4 mismatches (-F 0x004 -F 0x008 -F 0x0100 -F 0x0400 -f 0x001 -q
1364 1). MACS (v.2.1.2)[28] was used to call peaks from the BAM file with IgG control and recommended
1365 mappable genome size (the default values were used for the other parameters). NarrowPeak mode

1366 was used for NFAT1, H3K27me3, and H3K4me3. Binding signal was normalized by scaling to 1
1367 million mapped reads using BEDTools (version 2.27.1)[29] and bedGraphToBigWig (version 377)[30]
1368 and visualized as heatmaps using deepTools plotHeatmap (version 3.2.1)[27]

1369 In the CUT&RUN experiment with spike-in E. coli, two modifications were made: i) a hybrid
1370 reference of mouse mm10 and E. coli ASM584v2, and ii) signals were normalized by scaling to
1371 per million reads mapped to E. coli.

1372 Differential binding analysis was performed using DiffBind (v.3.4.7) (summit = 75 (for NFAT1)
1373 and 100 (for H3K27me3 and K3K4me3 modifications), normalized by the trimmed mean of M
1374 values (TMM) approach library size estimated by reads mapped to "background" regions. Peaks
1375 were annotated to the nearest genes with the annotatePeak function in R package ChIPseeker
1376 (v.1.30.3) at the gene level using default parameters. Genes were ranked by fold-change (log2
1377 transformed; if a gene was associated with multiple peaks, the mean was used). GSEA was then
1378 performed against MSigDB collections with R package clusterProfiler (v.4.2.2).

1379

1380 **RNA-seq**

1381 The isolated $CD8^+$ TIL were washed once with cold PBS and pelleted at 1500 rpm at 4°C. Total
1382 RNA was isolated using the Direct-zol RNA Microprep Kit (cat. R2061, Zymo Research)
1383 according to the manufacturer's instructions and quantified using an Agilent 4200 TapeStation.
1384 Libraries were prepared using the KAPA RNA HyperPrep Kit with RiboErase (HMR) (cat.
1385 08098131702, Roche) and purified by AMPure SPRI beads (cat. B23318, Beckman-Coulter).
1386 Libraries were quantified and size distribution was determined using a Agilent 4200 TapeStation
1387 before paired-end sequencing was performed.

1388 **RNA-seq data processing**

1389 Paired-end sequencing reads were mapped by the pipeline of St. Jude Center for Applied
1390 Bioinformatics. The reads were trimmed using Trim Galore (version 0.5.0)
1391 (https://github.com/FelixKrueger/TrimGalore) with default parameters. Reads were aligned to the
1392 reference mouse mm10 assembly plus ERCC spike-in sequences using STAR (version 2.7.5a)[37].
1393 The resulting alignments, recorded in BAM file, were sorted, indexed, and marked for duplicates

1394 with Picard MarkDuplicates function (version 2.19.0). Transcript quantification was calculated
1395 using RSEM[38]. Differential gene expression analysis was carried out with DESeq2 with Wald test
1396 (default parameters)[39]. To examine if global changes in gene expression were present, the RUVg
1397 function in the RUVSeq package was used for normalization with ERCC spike-in followed by
1398 DESeq2 according to the RUVSeq manual[40]. Gene set enrichment analysis (GSEA) was performed
1399 against the MSigDB database[41] with R package clusterProfiler (version 4.2.2)[35] with the genes
1400 ranked by the Wald statistic from DESeq2 analysis.

1401

1402 **Quantitative Proteomics by tandem mass tag mass spectrometry (TMT-MS)**

1403 $CD8^+$ T cells were isolated from WT mice and activated with anti-CD3 antibody by crosslinking
1404 with IgG for 30 min. Activated and untreated cells were washed once with ice-cold PBS and flash-
1405 frozen in liquid nitrogen. Proteomic profiling of the whole proteome and methylome was carried
1406 out using a previously optimized protocol[42] with modifications. Briefly, the cells were lysed in 8M
1407 Urea lysis buffer using pulse sonication, and approximately 100 µg of protein per sample was
1408 digested with Lys-C (Wako, 1:100 w/w) at 21 °C for 2 h, followed by dilution to reduce urea to
1409 2M, and further digestion with trypsin (Promega, 1:50 w/w) at 21 °C overnight. The protein digests
1410 were acidified (trifluoroacetic acid to 1%), centrifuged at 21,000 x g for 10 min at 4°C to remove
1411 any insoluble material, desalted with Sep-Pak C18 cartridge (Waters), and dried by Speedvac.
1412 Each sample was resuspended in 50 mM HEPES (pH 8.5), TMT labeled, mixed equally, desalted,
1413 and fractionated by offline HPLC (Agilent 1220) using basic-pH reverse phase LC (Waters
1414 XBridge C18 column, 3.5 µm particle size, 4.6 mm x 25 cm, 180 min gradient, 80 fractions).
1415 Fractions were aliquoted (5% v/v) for whole proteome and methylome (95% v/v) profiling. The
1416 methylome fractions were further concatenated into 10 fractions for antibody-based sequential
1417 mono-methyl-arginine and di-methyl-arginine peptide enrichment.

1418

1419 **Antibody-based Sequential Methylome Enrichment**

1420 Each concatenated fraction (approximately 1 mg) was resuspended in 400 µL ice-cold IAP buffer
1421 (50mM MOPS, pH 7.2, 10 mM sodium phosphate, and 50 mM NaCl) and centrifuged at 21,000 ×
1422 g for 10 min at 4°C to remove any insoluble material. The peptides were then incubated with
1423 mono-methyl-Arginine antibody beads (mono-me-R, 12235S Cell Signaling Technology) at an

antibody-to-peptide ratio of 1:20 (w/w, optimized through a pilot experiment) for 2 hr at 4°C with gentle end-over-end rotation. The antibody beads were then collected by a brief centrifugation, washed 3 times with 1 mL ice-cold IAP buffer and twice with 1 mL ice-cold PBS, while the supernatants were carefully removed and used for the sequential di-methyl-Arginine peptide enrichment (di-me-R symmetric, cat.13563S Cell Signaling Technology). Peptides were eluted from the beads twice at room temperature with 50 µL of 0.15% TFA, dried, and analyzed by LC-MS/MS.

LC-MS/MS Analysis

Each sample was dried, reconstituted, and analyzed by LC-MS/MS (a CoAnn 75 µm x 30 cm column, packed with 1.9 µm C18 resin from Dr. Maisch GmbH) interfaced with the Orbitrap Fusion MS (Thermo Fisher). LC settings included an 80 min gradient of 15%-40% buffer B (70% ACN, 2.5% DMSO, and 0.1% FA) with buffer A (2.5% DMSO, and 0.1% FA) at a flow rate of ~0.25 µL /min flow rate. MS settings included data-dependent (3 s cycle) mode with a survey scan in the Orbitrap (60,000 resolution, scan range 410–1600 m/z, 1 × 106 AGC target, and 50 ms maximal ion time), followed by sequential isolation of abundant ions in a 3 s duty cycle, with fragmentation by higher-energy collisional dissociation (HCD, 38 normalized collision energy), and high-resolution detection of MS/MS ions in the Orbitrap (60,000 resolution, 1 × 105 AGC target, 105 ms maximal ion time,1.0 m/z isolation window, and 20 s dynamic exclusion).

Database Search and TMT Quantification

The MS/MS spectra were searched against the UniProt Mouse protein database (version 2020.04.22) using the COMET algorithm (v2018.013[43] **)** with the JUMP software suite[44]**.** Search parameters included MS1 mass tolerance of 20 ppm and MS/MS of 0.02 Da, fully tryptic, static mass shift for the TMT16 tags (+304.2071453) and carbamidomethyl modification of 57.02146 on cysteine, dynamic mass shift for Met oxidation (+15.99491), for mono-methyl-Arginine (+14.01565), and for di-methyl-Arginine (+28.0313), maximal missed cleavage (n = 3), and maximal dynamic modifications per peptide (n=5). All matched MS/MS spectra were filtered by mass accuracy and matching scores to reduce false discovery rate (FDR) below 1% for either proteins (whole proteome analysis) or peptides (methylome analysis), based on the target-decoy strategy[45,46].

1455

1456 TMT quantification analysis was performed as previously reported[47] with the following
1457 modifications: (i) extracting reporter ion intensities from each PSM; (ii) correcting the intensities
1458 according to the isotopic distribution of each TMT reagent; (iii) removing PSMs of very low
1459 intensities (e.g., minimum value of 1,000 and median value of 5,000); (iv) normalizing sample
1460 loading bias with the trimmed median intensity of all PSMs; (v) calculating the mean-centered
1461 intensities across samples (e.g., relative intensities between each sample and the mean), (vi)
1462 summarizing protein relative intensities by averaging related PSMs; (vii) finally deriving protein
1463 absolute intensities by multiplying the relative intensities by the grand-mean of the three most
1464 highly abundant PSMs. (vii) Protein fold change and p-values of different comparisons were
1465 calculated based on the protein intensities, using a log transformation and moderated t-test with
1466 the limma R package[48,49].

1467

1468 **Quantification and statistical analysis**

1469 Data were plotted and analysed using GraphPad Prism (GraphPad Software, v.9.2.0). Statistical
1470 significance was calculated using unpaired one- or two-tailed Student's *t*-tests. Two-way ANOVA
1471 was performed to compare tumor growth curves. The log-rank (Mantel–Cox) test was performed
1472 to compare the mouse survival curves. For Fig. 7b, a linear mixed effects model with log10(y) as
1473 the response variable, group as a fixed-effect predictor variable, and mouse as a random-effect
1474 predictor variable was fit to the data. This model represents data with cells as random samples
1475 from each mouse. The results showed that the mean log10(y) values of the two mouse groups
1476 differed by -0.131 units (95% CI: -0.163, -0.0999; $p = 6.98\ 10^{-15}$). Statistical significance was set
1477 at $P < 0.05$. Data are presented as mean ± SEM. No statistical methods were used to determine
1478 sample size.

1479 **References**

1480

1481 1 Welsh, R. M. & Seedhom, M. O. Lymphocytic choriomeningitis virus (LCMV):
1482 propagation, quantitation, and storage. *Curr Protoc Microbiol* **Chapter 15**, Unit 15A
1483 11 (2008). https://doi.org:10.1002/9780471729259.mc15a01s8

2 Zhao, S. *et al.* NKD2, a negative regulator of Wnt signaling, suppresses tumor growth and metastasis in osteosarcoma. *Oncogene* **34**, 5069-5079 (2015). https://doi.org:10.1038/onc.2014.429

3 Haydar, D. *et al.* Cell-surface antigen profiling of pediatric brain tumors: B7-H3 is consistently expressed and can be targeted via local or systemic CAR T-cell delivery. *Neuro Oncol* **23**, 999-1011 (2021). https://doi.org:10.1093/neuonc/noaa278

4 Sharma, G. *et al.* Analysis of 26 amino acids in human plasma by HPLC using AQC as derivatizing agent and its application in metabolic laboratory. *Amino Acids* **46**, 1253-1263 (2014). https://doi.org:10.1007/s00726-014-1682-6

5 Meszaros, B. *et al.* Recent breakthroughs in computational structural biology harnessing the power of sequences and structures. *Curr Opin Struct Biol* **80**, 102608 (2023). https://doi.org:10.1016/j.sbi.2023.102608

6 Lee, C. H. & MacKinnon, R. Activation mechanism of a human SK-calmodulin channel complex elucidated by cryo-EM structures. *Science* **360**, 508-513 (2018). https://doi.org:10.1126/science.aas9466

7 Jo, S., Kim, T., Iyer, V. G. & Im, W. CHARMM-GUI: a web-based graphical user interface for CHARMM. *J Comput Chem* **29**, 1859-1865 (2008). https://doi.org:10.1002/jcc.20945

8 Lee, J. *et al.* CHARMM-GUI Input Generator for NAMD, GROMACS, AMBER, OpenMM, and CHARMM/OpenMM Simulations Using the CHARMM36 Additive Force Field. *J Chem Theory Comput* **12**, 405-413 (2016). https://doi.org:10.1021/acs.jctc.5b00935

9 Wu, E. L. *et al.* CHARMM-GUI Membrane Builder toward realistic biological membrane simulations. *J Comput Chem* **35**, 1997-2004 (2014). https://doi.org:10.1002/jcc.23702

10 Lomize, M. A., Pogozheva, I. D., Joo, H., Mosberg, H. I. & Lomize, A. L. OPM database and PPM web server: resources for positioning of proteins in membranes. *Nucleic Acids Res* **40**, D370-376 (2012). https://doi.org:10.1093/nar/gkr703

11 Jorgensen, W. L., Chandrasekhar, J., Madura, J. D., Impey, R. W. & Klein, M. L. Comparison of simple potential functions for simulating liquid water. *The Journal of Chemical Physics* **79**, 926-935 (1983). https://doi.org:10.1063/1.445869

12 Case, D. A. *et al.* AmberTools. *J Chem Inf Model* **63**, 6183-6191 (2023). https://doi.org:10.1021/acs.jcim.3c01153

13 B. N, P. *Mathematics of Computation* **28**, 669-671 (1974). https://doi.org:10.2307/2005951

14 in *Oeuvres complètes: Series 1* Vol. 10 *Cambridge Library Collection - Mathematics* (ed Augustin-Louis Cauchy) 399-402 (Cambridge University Press, 2009).

15 Feller, S. E., Zhang, Y., Pastor, R. W. & Brooks, B. R. Constant pressure molecular dynamics simulation: The Langevin piston method. *The Journal of Chemical Physics* **103**, 4613-4621 (1995). https://doi.org:10.1063/1.470648

16 Åqvist, J., Wennerström, P., Nervall, M., Bjelic, S. & Brandsdal, B. O. Molecular dynamics simulations of water and biomolecules with a Monte Carlo constant

pressure algorithm. *Chemical Physics Letters* **384**, 288-294 (2004). https://doi.org:https://doi.org/10.1016/j.cplett.2003.12.039

17 Ryckaert, J.-P., Ciccotti, G. & Berendsen, H. J. C. Numerical integration of the cartesian equations of motion of a system with constraints: molecular dynamics of n-alkanes. *Journal of Computational Physics* **23**, 327-341 (1977). https://doi.org:https://doi.org/10.1016/0021-9991(77)90098-5

18 Darden, T., York, D. & Pedersen, L. Particle mesh Ewald: An N·log(N) method for Ewald sums in large systems. *The Journal of Chemical Physics* **98**, 10089-10092 (1993). https://doi.org:10.1063/1.464397

19 Huang, J. *et al.* CHARMM36m: an improved force field for folded and intrinsically disordered proteins. *Nat Methods* **14**, 71-73 (2017). https://doi.org:10.1038/nmeth.4067

20 Best, R. B. *et al.* Optimization of the additive CHARMM all-atom protein force field targeting improved sampling of the backbone phi, psi and side-chain chi(1) and chi(2) dihedral angles. *J Chem Theory Comput* **8**, 3257-3273 (2012). https://doi.org:10.1021/ct300400x

21 Humphrey, W., Dalke, A. & Schulten, K. VMD: visual molecular dynamics. *J Mol Graph* **14**, 33-38, 27-38 (1996). https://doi.org:10.1016/0263-7855(96)00018-5

22 Langmead, B. & Salzberg, S. L. Fast gapped-read alignment with Bowtie 2. *Nat Methods* **9**, 357-359 (2012). https://doi.org:10.1038/nmeth.1923

23 Li, H. *et al.* The Sequence Alignment/Map format and SAMtools. *Bioinformatics* **25**, 2078-2079 (2009). https://doi.org:10.1093/bioinformatics/btp352

24 Barnett, D. W., Garrison, E. K., Quinlan, A. R., Stromberg, M. P. & Marth, G. T. BamTools: a C++ API and toolkit for analyzing and managing BAM files. *Bioinformatics* **27**, 1691-1692 (2011). https://doi.org:10.1093/bioinformatics/btr174

25 Ewels, P. A. *et al.* The nf-core framework for community-curated bioinformatics pipelines. *Nat Biotechnol* **38**, 276-278 (2020). https://doi.org:10.1038/s41587-020-0439-x

26 Amemiya, H. M., Kundaje, A. & Boyle, A. P. The ENCODE Blacklist: Identification of Problematic Regions of the Genome. *Sci Rep* **9**, 9354 (2019). https://doi.org:10.1038/s41598-019-45839-z

27 Ramirez, F. *et al.* deepTools2: a next generation web server for deep-sequencing data analysis. *Nucleic Acids Res* **44**, W160-165 (2016). https://doi.org:10.1093/nar/gkw257

28 Zhang, Y. *et al.* Model-based analysis of ChIP-Seq (MACS). *Genome Biol* **9**, R137 (2008). https://doi.org:10.1186/gb-2008-9-9-r137

29 Quinlan, A. R. & Hall, I. M. BEDTools: a flexible suite of utilities for comparing genomic features. *Bioinformatics* **26**, 841-842 (2010). https://doi.org:10.1093/bioinformatics/btq033

30 Kent, W. J., Zweig, A. S., Barber, G., Hinrichs, A. S. & Karolchik, D. BigWig and BigBed: enabling browsing of large distributed datasets. *Bioinformatics* **26**, 2204-2207 (2010). https://doi.org:10.1093/bioinformatics/btq351

31 Ross-Innes, C. S. *et al.* Differential oestrogen receptor binding is associated with clinical outcome in breast cancer. *Nature* **481**, 389-393 (2012). https://doi.org:10.1038/nature10730

32 Chen, Y., Lun, A. T. & Smyth, G. K. From reads to genes to pathways: differential expression analysis of RNA-Seq experiments using Rsubread and the edgeR quasi-likelihood pipeline. *F1000Res* **5**, 1438 (2016). https://doi.org:10.12688/f1000research.8987.2

33 Yu, G., Wang, L. G. & He, Q. Y. ChIPseeker: an R/Bioconductor package for ChIP peak annotation, comparison and visualization. *Bioinformatics* **31**, 2382-2383 (2015). https://doi.org:10.1093/bioinformatics/btv145

34 Subramanian, A. *et al.* Gene set enrichment analysis: a knowledge-based approach for interpreting genome-wide expression profiles. *Proc Natl Acad Sci U S A* **102**, 15545-15550 (2005). https://doi.org:10.1073/pnas.0506580102

35 Yu, G., Wang, L. G., Han, Y. & He, Q. Y. clusterProfiler: an R package for comparing biological themes among gene clusters. *OMICS* **16**, 284-287 (2012). https://doi.org:10.1089/omi.2011.0118

36 Meers, M. P., Bryson, T. D., Henikoff, J. G. & Henikoff, S. Improved CUT&RUN chromatin profiling tools. *Elife* **8** (2019). https://doi.org:10.7554/eLife.46314

37 Dobin, A. & Gingeras, T. R. Mapping RNA-seq Reads with STAR. *Curr Protoc Bioinformatics* **51**, 11 14 11-11 14 19 (2015). https://doi.org:10.1002/0471250953.bi1114s51

38 Li, B. & Dewey, C. N. RSEM: accurate transcript quantification from RNA-Seq data with or without a reference genome. *BMC Bioinformatics* **12**, 323 (2011). https://doi.org:10.1186/1471-2105-12-323

39 Love, M. I., Huber, W. & Anders, S. Moderated estimation of fold change and dispersion for RNA-seq data with DESeq2. *Genome Biol* **15**, 550 (2014). https://doi.org:10.1186/s13059-014-0550-8

40 Risso, D., Ngai, J., Speed, T. P. & Dudoit, S. Normalization of RNA-seq data using factor analysis of control genes or samples. *Nat Biotechnol* **32**, 896-902 (2014). https://doi.org:10.1038/nbt.2931

41 Liberzon, A. *et al.* The Molecular Signatures Database (MSigDB) hallmark gene set collection. *Cell Syst* **1**, 417-425 (2015). https://doi.org:10.1016/j.cels.2015.12.004

42 Yu, K. *et al.* High-Throughput Profiling of Proteome and Posttranslational Modifications by 16-Plex TMT Labeling and Mass Spectrometry. *Methods Mol Biol* **2228**, 205-224 (2021). https://doi.org:10.1007/978-1-0716-1024-4_15

43 Eng, J. K. *et al.* A deeper look into Comet--implementation and features. *J Am Soc Mass Spectrom* **26**, 1865-1874 (2015). https://doi.org:10.1007/s13361-015-1179-x

44 Wang, X. *et al.* JUMP: a tag-based database search tool for peptide identification with high sensitivity and accuracy. *Mol Cell Proteomics* **13**, 3663-3673 (2014). https://doi.org:10.1074/mcp.O114.039586

45 Peng, J., Elias, J. E., Thoreen, C. C., Licklider, L. J. & Gygi, S. P. Evaluation of multidimensional chromatography coupled with tandem mass spectrometry (LC/LC-MS/MS) for large-scale protein analysis: the yeast proteome. *J Proteome Res* **2**, 43-50 (2003). https://doi.org:10.1021/pr025556v

46 Elias, J. E. & Gygi, S. P. Target-decoy search strategy for increased confidence in large-scale protein identifications by mass spectrometry. *Nat Methods* **4**, 207-214 (2007). https://doi.org:10.1038/nmeth1019

47 Niu, M. *et al.* Extensive Peptide Fractionation and y(1) Ion-Based Interference Detection Method for Enabling Accurate Quantification by Isobaric Labeling and Mass Spectrometry. *Anal Chem* **89**, 2956-2963 (2017). https://doi.org:10.1021/acs.analchem.6b04415

48 Bai, B. *et al.* Deep Multilayer Brain Proteomics Identifies Molecular Networks in Alzheimer's Disease Progression. *Neuron* **105**, 975-991 e977 (2020). https://doi.org:10.1016/j.neuron.2019.12.015

49 Smyth, G. K. Linear models and empirical bayes methods for assessing differential expression in microarray experiments. *Stat Appl Genet Mol Biol* **3**, Article3 (2004). https://doi.org:10.2202/1544-6115.1027